E-21-T23

Final Report

for

LDF Project 01H5

Advanced Remote Sensing Applications to Strategic Surveillance Systems

Rome Air Development Center : Electro-optics Applications Branch / OCSP

Principal Investigator: N. Chonacky - Project Scientist

LDF Funds/Yr: $30,000 / FY-85 Contractor: In-house

19 February 1990

LDF Project 01H5

ADVANCED REMOTE SENSING APPLICATIONS TO STRATEGIC SURVEILLANCE SYSTEMS

Rome Air Development Center : Electro-optics Applications Branch / OCSP

Principal Investigator: N. Chonacky - Project Scientist

ABSTRACT

This report describes the assembly and preliminary testing of a LIDAR system consisting of: two high-power, flashlamp-pumped dye lasers as sources; a 1-meter Cassegrain telescope together with a 1-meter, clear-aperture coelostat as both transmitter and receiver in a monostatic configuration; associated optics for beam expansion, handling, and diagnostics; a silicon diode and associated microcomputer-driven electronics as detector. The context of this research is a program to investigate LIDAR concepts for their scientific and technological feasibility and their applicability to satellite surveillance operations which require the measurement of gases remotely from the ground. This project was prompted by the conjunction of particular Air Force needs for real-time measurements of atmospheric water vapor concentrations and recent successes by a number of different researchers at measuring gaseous substituents in the atmosphere using LIDAR systems. The particular goal of the Laboratory Director's Fund part of this project is to make an initial effort to setup and operate a LIDAR system suitable for such concept testing at the RADC Advanced Optical Testing Labortory (AOTF) at our Verona NY Test Site, using equipment already on-hand and using the AOTF, which is ideally suited for such work, in an attempt to bring such a system quickly on line at relatively low cost.

1. Introduction

Recent successful measurements of gaseous substituents in the atmosphere using LIDAR systems[1,2,3,4] have increased the prospects for successfully measuring gases, such as water vapor, in strategic surveillance applications. An overall goal of our remote sensing program is to evaluate LIDAR concepts for their scientific and technological feasibility and their applicability to satellite surveillance requirements. In this particular project we are interested in LIDAR concepts that yield real-time measurements of atmospheric water vapor concentrations from the ground along paths that slew. The particular goal of this Laboratory Director's Fund project[5] is to make an initial effort to setup and operate a LIDAR system suitable for such concept testing at the RADC Advanced Optical Testing Laboratory (AOTF) at our Verona NY Test Site.

In this report we describe how we designed, assembled, and tested a LIDAR system from various components, in consort with major Air Force resources already on hand at the AOTF. This monostatic LIDAR uses two high-power, flashlamp-pumped dye LASERs, with associated power supplies, as the light sources. A 1-meter Cassegrain telescope at the AOTF is one of two, principal optical elements of the transmitter/receiver. The other is a 1-meter, clear-aperture coelostat, which directs the LIDAR's line-of-sight along ground or sky paths, as testing requires, while fixing the focal plane of the telescope relative to the laboratory. This arrangement permits us to operate with the same system configuration either along ground or sky paths, and to construct the configuration of source LASERs, beam controls, exit and entrance optics, and detectors on an optical bench *fixed* in the laboratory. This fixed focal-plane feature makes our experimental setup ideally suited for developing and testing various LIDAR techniques.

We have arranged the material in this report into several sections. In the first of these, SECTION 2: APPROACH, we outline the functional organization of our LIDAR system and the chronological organization of the project's workplan. Next, in SECTION 3: MODELS AND CALCULATIONS, we provide a quantitative context for various design requirements that are background for SECTION 4: COMPONENT DEVELOPMENT AND TESTING, where we describe various subsystems that we researched and developed. We arranged this latter section in terms of the LIDAR components outlined in our functional description of the system, in SECTION 2. In SECTION 4: SYSTEM INTEGRATION AND TESTING, we report our efforts to make all of the subsystems work together to achieve the LIDAR function. Finally, in SECTION 5: RESULTS AND RECOMMENDATIONS, we summarize the lessons we draw from our results.

This report describes work done during three years. The work on this project was started at the beginning of FY85, in October 1984. We include in this report, the results of all work activity completed as of November 1987. The first, critical year of these was funded by the Laboratory Director. The follow-on effort, supported by the SDIO, permitted us to achieve most of our original construction objectives and to address some actual operations problems. We include results from these additional years of effort in this LDF final report because they provide the proper context for seeing the overall significance of the LDF-supported part of this work.

2. Approach

We first proposed building a LIDAR system which would detect gases using their fluorescence. Early in this project we became aware of the need to solve a critical problem in an IR measurements program at the **A**ir Force **M**aui **O**ptical **S**tation (**AMOS**). In particular, a theoretical study[6] suggested that a **Di**fferential **A**bsorption LIDAR (**DIAL**) system could solve this measurement problem. Since the equipment we had on hand was also suited to constructing a DIAL system, at an early date we adapted our goals to developing a DIAL in lieu of the fluorescence system. We proposed to conduct a proof-of-concept test for the particular kind of LIDAR system cited to solve the AMOS problem. Since we did not do significant work on the original fluorescence LIDAR concept before moving to the DIAL, we report here only on the latter.

2.1. Lidar principles; the DIAL.

In this section we discuss the principles of operation of LIDAR, first modelling them in simple terms and then using them to explain the real system we are designing. The basic LIDAR principle is just like that of ordinary RADAR; they both detect and range by sending out a pulse of electromagnetic energy and waiting for the backscatter to return. This return indicates the prescence of material in the beam, from which the radiation has scattered. The time between the departure of the pulse and the return of any reflection measures the range of the scattering, i.e.the source of that reflection.

One difference between RADAR and LIDAR is in the characteristics of the electromagnetic energy, which in the case of such a RADAR is a microwave and in the case of a LIDAR is light. These radiations differ in wavelength, and hence in the means to generate and guide them. Tuned electron oscillations produce microwave pulses and a LASER produces light pulses. A less obvious but very important difference in characteristics between the two is the manner in which the light interacts with matter, as compared to microwaves. Whereas the absorption and scattering of microwave energy depends chiefly upon the (net electron) density in the intervening material, the absorption and scattering of light energy can also depend upon the light's wavelength. That this wavelength dependence is often sharp and often characteristic of the *particular kind of material* involved in the interaction, is what makes LIDAR a powerful *analytical* tool. In the case at hand, we wish specifically to measure the concentration water vapor, and not other substituents, in the atmosphere. Thus we use light wavelengths that interact specifically with water molecules. We choose to use light in the very-near infrared region of the optical spectrum.

A most respected and comprehensive reference on LIDAR concepts is by Raymond Measures.[7] At the least detailed level, a LIDAR consists of a pulsed (LASER) light source, beam-forming exit optics to transmit the pulse in the desired direction, receiving optics to capture as much of the returning, scattered light as possible, a detector to notice when and how much light has returned, and a computer to record this return information and calculate the amount of water vapor at various ranges. The block diagram in [Fig.1] depicts the functional organization of a LIDAR at this level of detail. In our LIDAR we arranged the outgoing beam direction and the incoming line-of-sight to be identical. This

is called a **monostatic** beam geometry. [Fig.2] shows schematically how we configured our monostatic LIDAR system. This arrangement, which confines the output light and the input field-of-view to a common path, is particularly convenient if, as is the case with our LIDAR, this path must slew through space.

A LIDAR requires backscattered light to operate. The backscatter that our LIDAR uses is Rayleigh scattering from the transmitting medium, in this case the substituents of the atmosphere distributed along the illuminated path. This scattering process is commonly the predominant interaction with light for all atmospheric substituents; and although it is wavelength dependent, it is not sharply so. Moreover, this degree of wavelength dependence is the *same* for all molecules. On the otherhand, we can select a source radiation wavelength near which the absorption, by water molecules only, is *very* wavelength dependent. Since both the outgoing source radiation and the returning backscatter have identical wavelengths, the returning Rayleigh backscatter for a given amount of water can depend sharply on the source wavelength due to the process of absorption. For example, light precisely at an absorption "line" near 720NM is attenuated markedly by water. Additionally, the degree of this water-selective attenuation can be simply related by simple theory to the amount of water vapor that the radiation encounters. This is the essence of the **DIAL principle**.

> Measure returns from two LIDAR systems, aimed in the same direction, which are virtually identical except for the wavelength of their source radiation. Operate one source ***on*** the water absorption line and the other ***off*** of that line. If all else remains the same between the two, the ratio of their returns depends *simply* and *only* upon amount of the water vapor within their common beam paths.

A simple model illustrates this principle. We can use this model to derive the essential relationship between the number of absorbing molecules and the return energies at the two wavelengths.

[Fig.3] shows the source light pulses as irradiances E_{on} and E_{off}. We picture these each as travelling next to one another for clarity in the figure, though they actually must traverse identical paths. They each pass through N water molecules, pictured as a slab, on the way to their (common) scattering site, and then travel again through these molecules on the way back. The vertical line dividing the whole slab into two halves represents the scattering site; and though the "scattered" radiation in the picture doesn't turn around and head back, the effect of the water on it is the same if the slab halves are identical. The points are these: all the radiation going to and coming from a given scattering site passes through the same molecules twice; the total water molecules up to the range of any given scattering site act like an absorbing slab to the radiation scattering at that site.

The two emerging irradiances E'_{on} and E'_{off} are attenuated versions of their respective source irradiances E_{on} and E_{off}. The attenuation is due to more than just water; in fact there are many other molecular, light-absorbing species in the atmosphere which belong in this slab. We account for all absorption effects with the familiar relation for light passing through a slab of thickness **x**, Beer-Lambert Law:

[Eq. 1] $$E' = E\, e^{-\mu x} = E\, e^{-\alpha(2N)}$$

Most people are familiar with the first version of this relation which expresses the linear extinction coefficient μ and the penetration depth **x**. You must appreciate that the validity of this form is restricted to materials of uniform composition (e.g. density), which is not the case for the atmosphere. The second is a more generally valid version which expresses the molar extinction coefficient α and the molar population **N**. This latter form emerges because light absorption is fundamentally a molecular, not a collective, process. Note that we have added a factor of 2 here because the radiation passes *twice* through the atmosphere: once going to the site and once returning. These two extinction coefficients express the same optical information in different forms. They are related as $\mu = \alpha\, \mathbf{nA}$, where **n** is the molar density (moles/volume) and **A** is the cross-sectional area illuminated.

If we wish to apply equation [1] to the individual light components, *on* and *off*, then we must use a different extinction coefficient for each, reflecting the fact that these components share absorption for most of the atmospheric molecular substituents, but certainly not for water. The extinction coefficients for competing processes are simply additive; so we have

$$\alpha_{on} = \alpha_{water} + \alpha_{other}$$
$$\alpha_{off} = \alpha_{other}$$

and

[Eq. 2] $$E'_{on} = E_{on}\, e^{-\alpha_{on} 2N} = E_{on}\, e^{-(\alpha_{water} + \alpha_{other})2N}$$

[Eq. 3] $$E'_{off} = E_{off}\, e^{-\alpha_{off} 2N} = E_{off}\, e^{-\alpha_{other} 2N}$$

Likewise, the scattered light goes out in all directions, not just straight back to the receiver, further depleting the returning irradiance. But we arrange the two LIDARs to be identical; and consequently these depleting effects, whatever their value, are *identical* for both *on* and *off* components. We simply lump them into a general "depletion" factor γ which we use to modify Beer-Lambert Law, equation [1], using the same γ value for both components.

$$E' = \gamma E\, e^{-\alpha 2N}$$

The validity of the DIAL principle is requires that both LIDARs be identical except for their respective operating wavelengths, which still must be close together. Moreover, to optimize the sensitivity of this technique, one of these two wavelengths must be precisely *on* the absorption peak while the other is wholly *off* the peak. This arrangement serves to maximize the effect of the factor α_{water}.

Finally, to evaluate **N(x)**, the integrated water vapor out to any given range **x**, we take the depletion-modified form of equations [2,3]

$$E'_{on} = \gamma E_{on}\, e^{-(\alpha_{water} + \alpha_{other})2N}$$
$$E'_{off} = \gamma E_{off}\, e^{-\alpha_{other} 2N}$$

and divide them by one another.

$$\frac{E'_{on}}{E'_{off}} = \frac{\gamma E_{on}\, e^{-(\alpha_{water} + \alpha_{other})2N}}{\gamma E_{off}\, e^{-\alpha_{other} 2N}}$$

Cancelling common factors and taking the logarithm of both sides, we arrive at the relation for molar value of the integrated water vapor:

$$\ln\left(\frac{E'_{on}}{E'_{off}}\right) = \ln\left(\frac{E_{on}}{E_{off}}\right) - (\alpha_{water} + \alpha_{other})2N + \alpha_{other}\,2N$$

Simplifying and rearranging to solve for the integrated, molar water vapor value up to the range **x**:

[Eq. 4]
$$N(x) = \frac{\ln\left(\frac{E'_{on}}{E'_{off}}\right) - \ln\left(\frac{E_{on}}{E_{off}}\right)}{2\,\alpha_{water}}$$

Here (E'_{on}/E'_{off}) is the observed return ratio; (E_{on}/E_{off}) is the ratio of relative source irradiances, and serves to normalize the observed returns on a shot by shot basis. We understand in using this relation that the values for the returning light irradiances E'_{on} and E'_{off} are those detected at the specific time $\mathbf{t = x/c}$ correponding to return from the given range **x**.

These considerations and relations dictate how you must design a DIAL. [Fig.4] shows a block diagram of a LIDAR from the proposal for the AMOS,[8] which we use to discuss the functional organization of our DIAL. In our design, the two component LIDARs are actually, almost one. We decided to design our system to use two (identical) LASERs in tandem, but otherwise to share the optics, detector, signal processing, and controls. Thus, the diagram serves to describe our DIAL as well as each component LIDAR, where the LASER "box" contains two LASERs operating, alternately, at slightly different wavelengths; and the signal processing and controls must be properly phased.

In DIAL operation, we must tune the *on*-line LASER precisely to the water absorption line. This requires that we make an absolute measurement of that wavelength, and control it accordingly. We have somewhat more leeway in tuning the *off*-line LASER; but it must be in a spectral region where water aborption is minimal. We use two different LASER pulses as *on/off* sources; thus we also must measure their relative irradiances so that we can normalize the resulting returns. We expect the "signal" represented by the difference in pulse returns to be small, and therefore must average repeated pulse returns to enhance the signal to noise ratio if we wish to extract reliable information. We wish to know the water distribution along the path as well as total water content, so the receiving system must time-resolve the returning signals. Because of the high quality of our receiving telescope, we decided to use a small photodiode instead of PMT's for return detection.

2.2. Functional Organization of the Effort.

Since our aim is to develop and evaluate components as well as an entire DIAL system, we decided to "stage" the work, choosing first to configure a bench development system and then to work toward a field test system in series of steps.

The basic development system with which we started uses a single LASER. Our development LASER system consists of one dye LASER source and several diagnostic instruments. These instruments include a spectrometer/wavemeter, an energy meter, a space-resolving pulse profiler, and a time-resolving pulse profiler (c.f.[Fig.5]). Each of these is coupled to the LASER beam by means of folding optics. Their electronic outputs are suitably transformed by signal-processing circuits and sent to digital computers. We can use these diagnostics, together, to obtain qualitative and quantitative information about the operation of the LASER source and the character of its output pulses. We need this information in the developmental phase both to learn how to operate the LASER reliably and efficiently, and to properly interpret LIDAR test data once we install the LASER in a LIDAR system. The development LIDAR system must be capable of operating at visible as well as the near-IR (λ~720NM) wavelength regimes because visible operation greatly simplifies testing activities in the field.

The next stage is a development LIDAR system. This consists of the foregoing, developmental dye LASER system to which we add a beam expander, transfer optics to place the expanded beam into the receiving telescope's aperture (c.f. monostatic geometry), and an optical detection system at the focal plane of the telescope (c.f. [Fig.6]). We use this system to propagate pulses into the atmosphere and measure the scattering returns from hard targets as well as the atmosphere. These experiments obtain information about beam propagation phenomena, scattering by the atmosphere, and the performance of the receiving system including the receiver optics, shutters, detectors, and the data acquisition system. We need this information to evaluate the expected strength of the (return) signal in our operational LIDAR system; but also to locate and evaluate the parasitic scattering by the system's optical elements and the system's electronic noise, all of which are crucial to the evaluation of an operational LIDAR's actual performance capabilities.

During the time period covered by this report, we had not progressed to the full DIAL field operation. Therefore, we detail the field version DIAL only in the last SECTION 6: RESULTS AND RECOMMENDATIONS.

In addition to these two developmental systems, we established two subsidiary test systems to carry out this project. One of these is a photodetector test and calibration facility. This consists of light-tight enclosures, pulsed and cw light sources with fiber optic output couplers, remotely controlled translation stages, calibrated detectors, and associated low noise electronics. In principle this system is capable of measuring the absolute and relative responses of detectors in both the time and intensity domains. The other test system is for obtaining beam geometry diagnostics. This consists of instruments capable of bore-sight aligning a beam and evaluating beam collimation in the field.

We have organized the SECTION 4: COMPONENT DEVELOPMENT AND TESTING of this report according to the DIAL's components. Thus, the following components list, arranged according to system function, summarizes our DIAL design and provides an outline for much of the information in this report:

1. Sources:
   Pulsed LASERs, operating at optical and/or IR wavelengths.

2. Output beam diagnostics:
   narrow-band spectrometer;
   energy meter for pulse normalization;
   beam time and spatial profilometers.

3. Exit optics:
   beam expander;
   folding optics;
   beam director (coelostat mirrors).

4. Receiver optics:
   beam director;
   transfer optics.

5. Detector:
   low-noise optical detector;
   high dynamic-range pulse amplifiers;
   gain switched amplifiers;
   photon counting.

6. Computer:
   signal digitization;
   data acquisition;
   data archiving;
   signal processing.

2.3. Chronological Organization of the Effort.

The following list of milestones[9] describes the general workflow in this project. Rather than reconstruct a detailed chronology of the *actual* history of work over the three year period, we present the original schedule, framed in the In-house Work Unit Plan[10] at the start of the project, in **Appendix [A]**. That schedule contains a detailed, planned task list extracted from the original LDF proposal. Subject to some additions and deletions, it still describes the approximate scope and general time sequence of the work actually done; only the time scale is underestimated.

Milestones:

1. LASER Reactivation
2. Diagnostic Instrumentation
3. Etalon Retrofitting
4. Detection System
5. Indoor Testing
6. Beam Extraction Optics
7. Outdoor Testing

3. Models and Calculations

Our LIDAR must sense gases in the atmosphere where the Rayleigh scattering from atmospheric substituents, rather than reflection from a "hard" target, generates the return signal. Thus the Rayleigh scattering coefficient dictates the required intensity and operating wavelength of candidate source LASERs. In what follows we use a simplified model of our system to generate numerical values for important design parameters such as strengths expected for the return signals for given values of LASER strength, atmospheric characteristics at ranging altitudes, receiver aperture, etc. To carry out these calculations we base our work on the standard developments of this subject already available.[11,12]

First, it is helpful to estimate the strength of the Rayleigh backscatter that we can expect at the wavelengths we need for water experiments. The general *molecular* backscattering cross section is

$$\sigma_\pi^R \equiv \frac{d\sigma_R(\theta = \pi)}{d\Omega} = \frac{\pi^2 (n^2 - 1)^2}{N^2 \lambda^4}$$

where the incident/scattered radiation has wavelength λ, and the scattering material has refractive index **n** and number density **N**. Note that this quantity is essentially a molecular characteristic, i.e. it does not depend upon the macroscopic density **N**, even though **N** appears explicitly in the formula. This is practically true because the quantity $(\mathbf{n^2 - 1}) \propto \mathbf{N}$, nearly, for all gaseous material. However, the proportionality constant is not the same for all gases; and so some gas molecules backscatter more efficiently than others.[13]

This scattering cross section is the per molecule ratio of scattered intensity **I** (flux per steradian) to the incident irradiance $\mathbf{E_i}$ (flux per area). Thus the backscattered intensity per molecule is

$$I = E_i \sigma_\pi^R \qquad \text{(power per steradian)}$$

For the particular mixture of molecules in atmospheric gases below 100 km, the effective molecular backscattering cross section is[14]

$$\sigma_\pi^R = 5.45 \left[\frac{550}{\lambda(\text{nm})}\right]^4 \times 10^{-28} \text{ cm}^2 \text{ sr}^{-1}$$

This corresponds to the molecular values of

$$\sigma_\pi^R = 2 \times 10^{-28} \text{ cm}^2 \text{ sr}^{-1} \text{ @ } \lambda \sim 720\text{nm}$$

$$\sigma_\pi^R = 8 \times 10^{-28} \text{ cm}^2 \text{ sr}^{-1} \text{ @ } \lambda \sim 504\text{nm}$$

which are evaluations at the two operating wavelengths of our LASERs. This difference is a consequence of the inverse fourth power dependence of the Rayleigh scattering upon wavelength.

The scattering coefficient plays the same role for characterizing bulk scattering that the cross section plays for molecular scattering; it relates incident irradiance to scattered intensity on a *per unit volume* basis. At sea level where the molecular density under conditions of standard temperature and pressure is $N \sim 2.6 \times 10^{19}$ cm^{-3}, the atmospheric backscattering coefficient is

[Eq. 5] $$\frac{I_v}{E_i} \equiv \beta_\pi^R(\lambda) = N\,\sigma_\pi^R(\lambda) = 1.40\left[\frac{550}{\lambda(nm)}\right]^4 \times 10^{-8}\ cm^{-1}\ sr^{-1}$$

The backscattering coefficient takes on the values of

$$\beta_\pi^R = 0.5 \times 10^{-8}\ cm^{-1}\ sr^{-1} @\ \lambda\sim 720nm$$

$$\text{and } \beta_\pi^R = 2.0 \times 10^{-8}\ cm^{-1}\ sr^{-1} @\ \lambda\sim 504nm.$$

We wish to be able to evaluate how much backscatter to expect when operating at the water-detection wavelength $\lambda\sim 720nm$. This also turns out to be a "worst case" for the purposes of performance analysis since the scattering is lowest for the longest wavelengths. In the spirit of this "worst case" circumstance, we want to find expressions useful for design purposes. One of these should be the relationship of flux received Φ to energy of the source pulse $\mathcal{E}_0$, appropriate to our system, for the most stringent set of experimental conditions that we anticipate encountering. In the development of relevant expressions, we shall make use of results derived in **Appendix B**, where we lay out detailed considerations of the scattering process in space-time.

The average light flux Φ received is related to the optical energy $\mathcal{E}_r$ gathered by the receiver during the sampling interval T_{samp} used by the system's analog signal processor. This energy is the integrated, received optical power and is evaluated as

[Eq. 6a] $$\mathcal{E}_r = \int_{T_{samp}} \mathcal{P}_r(t')\,dt'$$

and the corresponding average flux is

[Eq. 6b] $$\Phi = \frac{\int_{T_{samp}} \mathcal{P}_r(t')\,dt'}{T_{samp}}$$

These two quantities are important for predicting the overall signal characteristics of the receiving system. Equations [6a,b] state explicitly how the elaspsed time t since initiation of the source pulse, and the duration T_{samp} of the sampling window, enter the evaluation of the receiver signal. The time integration is from $(t' = t)$ to $(t' = t+T_{samp})$. Both integrated results depend explicity on t (and *implicitly* on T_{samp}) and are, effectively, the LIDAR signals: viz. $\mathcal{E}_r = \mathcal{E}_r(t)$; $\Phi = \Phi(t)$.

The instantaneous, received optical power $\mathcal{P}_r$ is the rate at which optical energy arrives at the detector. It is related to the scattered intensity per unit volume I_v from equation [5]. Specifically

[Eq. 7] $$\mathcal{P}_r(t') = \int_{V_{base}} \int_{\Delta\Omega} I_v \, d\Omega \, dV$$

The integration volume $\mathbf{V_{base}}$ in equation [7] is derived in **Appendix B**. It is that volume of the propagation media that contributes to the scattered power the detector receives at a *given* instant **t'**.

[Eq. 8] $$V_{base} = \left[A \left(\frac{c\tau}{2} \right) \right]$$

Clearly $\mathbf{V_{base}}$ that is *not* the entire volume $\mathbf{V_{pulse}}$ occupied by the pulse at a given instant but, rather, half of it. This particular *portion* of $\mathbf{V_{pulse}}$ gives rise to scattering events which, even though they occur at *different* times within $\mathbf{V_{base}}$, arrive at the detector at a *single* instant of time **t'**. Thus $\mathbf{V_{base}}$ is a logically, rather than a geometrically, defined volume. Fortunately it is easy to identify $\mathbf{V_{base}}$ with a simple geometric volume, which leads to the expression of equation [8]. In **Appendix B** we show the space-time trajectories that connect particular scattering events to a common reception event at **t'**. These trajectories permits us to define $\mathbf{V_{base}}$ by tracing scattering, received at a given time point, back to the contiguous, elemental volumes **dV** along the propagation path that spawned that scattering. This means that the volume integration is a straight forward spatial integration along the propagation path, despite the logical, space-time complications. The elemental volumes **dV** are merely subdivisions of $\mathbf{V_{base}}$. The spatial integration accumulates their contributions into $\mathcal{P}_r(t')$.

The integration period T_{samp} in equations [x6] reflects the performance of the sampling circuit which effectively accumulates the instantaneous, received power $\mathcal{P}_r(t')$ over this time interval. During T_{samp}, the base volume shifts along the positive z-axis for a distance Δz_{shift}, generating a sampling distance Δz_{samp} and hence a sampling volume V_{samp}. These quantities are also derived in **Appendix B**.

[Eq. 9a] $$\Delta z_{samp} = \frac{c}{2} [T_{samp} + \tau]$$

[Eq. 9b] $$V_{samp} = A \bullet \Delta z_{samp}$$

Returning to the equation [7], since $\mathbf{I_v}$ is the per volume flux per unit solid angle scattered from each elemental volume **dV** in the space-time ensemble defining $\mathbf{V_{base}}$, and the solid angle of such scattering intercepted by the receiver aperture may depend upon the location of each such elementary scattering volume relative to that receiver, the order of the integrations here is important. We first sum the angular contributions (Ω-integration) to the scattering, carrying along the dependence, if any, upon the location of their elemental source **dV** within the base volume $\mathbf{V_{base}}$. Then we sum the spatial contributions (V-integration) from each **dV**, carrying along their dependence, if any, upon the time position (**t'**) of the reception event within the sampling window $[\mathbf{t}, \mathbf{t}+T_{samp}]$.

In the simplest case for the spatial integration: (1) the elements **dV** are all sufficiently far from the receiver to be treated as point sources; (2) the depth Δz_{samp} of the sampling

volume is sufficiently smaller than the average distance $\mathbf{z(t')}$ of that volume from the receiver so that we can treat it as a *single* point source; and (3) the cross sectional area **A** of the scattering volume is sufficiently small to neglect any angular dependence in the scattered intensity $\mathbf{I_v}$. In this case, the angular integration becomes trivial. Where $\Delta\mathbf{A_r}$ is the entrance area of the receiving optic,

[Eq. 10] $$\mathcal{P}_v(t') = \int_{\Delta\Omega} I_v \, d\Omega = I_v \, \Delta\Omega = I_v \left[\frac{\Delta A_r}{z^2(t')}\right]$$

If, in addition, the time profile of energy in the source pulse is "rectangular", i.e. constant energy between sharp leading and trailing edges, and its spatial profile is uniform, i.e. constant over its cross sectional area **A**, then the volume integration becomes trivial. But first we must express the pulse energy $\mathcal{E}_0$ as an equivalent power $\mathcal{P}_0$ and thence as an incident irradiance $\mathbf{E_i}$, so that we may employ equation [5] to compute the scattering. Where τ is the source pulse duration, we have

$$E_i = \left[\frac{\mathcal{E}_0}{\tau}\right]\frac{1}{A}$$

Incorporating this into equation [5] where we identify the distance **R** there with **z** here, we have

$$I_v = E_i \, \beta_\pi^z(\lambda) = \left[\frac{\mathcal{E}_0}{\tau}\right]\frac{1}{A}\beta_\pi^R(\lambda)$$

Substituting this expression into equation [10] above

$$\mathcal{P}_v(t') = I_v \, \Delta\Omega = E_i \, \beta_\pi^z(\lambda) = \left[\frac{\mathcal{E}_0}{\tau}\right]\frac{1}{A}\beta_\pi^z(\lambda) \, \Delta\Omega$$

Returning to equation [7], we use this result to obtain an expression for the received power which incorporates all of the simplifications assumed above.

$$\mathcal{P}_r(t') = \int_{V_{base}} \mathcal{P}_v \, dV = \left[\frac{\mathcal{E}_0}{\tau}\right]\frac{1}{A}\Delta\Omega \int_{V_{base}} \beta_\pi^z(\lambda) \, dV$$

$$= \left[\frac{\mathcal{E}_0}{\tau}\right]\frac{1}{A}\Delta\Omega \, \beta_\pi^z(\lambda) \, V_{base}$$

$$= \left[\frac{\mathcal{E}_0}{\tau}\right]\frac{1}{A}\Delta\Omega \, \beta_\pi^z(\lambda)\left[A\left(\frac{c\tau}{2}\right)\right]$$

Making all possible simplifications in this expression, we obtain

$$= \mathcal{E}_o \left[\frac{\Delta A_r}{z^2(t')}\right] \beta_\pi^z(\lambda) \left(\frac{c}{2}\right)$$

Finally, rearranging we obtain

[Eq. 11] $$\mathcal{P}_r(t') = \mathcal{E}_o \left(\frac{c}{2}\right)\left[\frac{\Delta A_r}{z^2(t')}\right] \beta_\pi^z(\lambda)$$

It is interesting to note that the source pulse duration τ does *not* appear in equation [11]. This means that, under the simplifying assumptions made in deriving this result, the pulse length of its LASER *does not* affect the LIDAR's scattered power, provided the pulse energy remains the same. What the source's pulse length *does* affect is the LIDAR's spatial resolution. We now model this aspect of LIDAR performance.

We return to equation [8], the expression drawn from **Appendix B** for the volume of origin of the scattering contributing to the instantaneous scattered power arriving at the receiver. $\mathbf{V_{base}}$ is the product of the cross sectional area **A** of the source beam and an "effective" length ($\Delta \mathbf{z_{base}} = \mathbf{c\tau/2}$) for the contributing region. Since all the points within this length contribute scatter that is being received simultaneously, this length is a limit on the spatial resolution which we can hope to obtain by using the LIDAR. In information theoretic terms, $\Delta \mathbf{z_{base}}$ is the limiting sample period. According to the Nyquist sampling theorem, any information sampled in this way cannot contain details having spatial wavelengths shorter than $\lambda_{\mathbf{Nyquist}} = \mathbf{2}\Delta \mathbf{z_{base}}$. In terms of the LIDAR parameters, profiles which we hope to obtain using the LIDAR scattering cannot have details more closely spaced than

[Eq. 12] $$\lambda_{spatial} \geq (2c\tau/2) = c\tau$$

where **c** is the speed of light and τ is the source LASER pulse duration.

Related to this limiting spatial resolution, there is an actual spatial resolution of the LIDAR. Equations [x6] are a reminder that any real measurement of the return signal necessarily involves a finite amount of time. This "time constant" of the measurement is manifest either as an integration time for weak signals (c.f. equation [6a]) or an averaging time for strong signals (c.f. equation [6b]). In the former case the receiver may, for example, count photons for a time $T_{\mathbf{samp}}$; while in the latter case the receiver may, for example, be low pass filtered with cut-off frequency $\mathbf{f_0} = \mathbf{1}/T_{\mathbf{samp}}$. In either case, during $T_{\mathbf{samp}}$ the volume of scattering origin moves, generating a "sampling volume" $\mathbf{V_{samp}}$ as it does. We already have discussed this above in stating equations [x12] which define the particular connection between $T_{\mathbf{samp}}$ and $\Delta \mathbf{z_{samp}}$ that apply to our sampling considerations here. Restating this

[Eq. 9a] $$\Delta z_{samp} = \frac{c}{2}\left[T_{samp} + \tau\right]$$

Notice from equation [x12] that Δz_{samp} has a lower limit of $\Delta z_{samp} = \Delta z_{base}$ as the sampling time $T_{samp} \rightarrow 0$. This results in the limiting spatial resolution, which is what we intuitively expect. On the other hand, Δz_{samp} becomes independent of the pulse length τ in the limit as $T_{samp} \gg \tau$. This is the zero-duration pulse limit and results in $\Delta z_{samp} = cT_{samp}/2$, directly proportional to the sampling time, again what we intutively expect. Δz_{samp} is often called the measurement bin size.

A consequence of a finite pulse duration is that the scattering from a given volume appears within *more* than one time sampling window. We call this condition "redundant" or "over"sampling. The degree to which this "duplication" of sampling from a given region occurs is determined by how long the pulse is as compared to how far the pulse moves during a sampling period, i.e.on the ratio (τ/T_{samp}). The *less* the pulse moves as compared to its length, the *greater* is the oversampling. The effects of oversampling are to boost the resolution, but to degrade the sampling statistics. There is not an unique relation between sampling times and resolution; it depends upon how the data are processed (i.e. digitally filtered) and for a given technique there will usually be an optimal value. Nonetheless, it is useful to calculate the degree of redundancy in the sampling process.

We characterize the degree of sampling redundancy by means of the sample number $\mathbf{f}$, defined as the number of (adjacent) sampling windows in which scattering from any given point appears. The value of $\mathbf{f}$ depends upon how far (Δz_{shift}) the pulse moves during a sampling gate in comparison to the length (Δz_{samp}) of the sampling volume. The latter is the combination of $\Delta z_{samp} = \Delta z_{shift} + \Delta z_{base}$. From our derivations in **Appendix B** and in accord with our notions outlined above, the sample number is given by

[Eq. 13]
$$\mathbf{f} = \frac{\Delta z_{samp}}{\Delta z_{shift}} = \frac{T_{samp} + \tau}{T_{samp}}$$

Here we have used equation [x12]. Only for $T_{samp} \gg \tau$ do we approach perfectly non-redundant spatial sampling ($\mathbf{f} = 1$), i.e. the scattering from each point in space occurs in exactly one sample. Thus, for any finite pulse duration at all, there must occur some sampling redundancy. This confirms our previous assertion that the effect is due to finite pulse duration.

Given that we have the freedom, within wide ranges, to select the sampling time T_{samp}, what are the criteria for choosing a value? Equations [x6] tells us that values of T_{samp} have to do with signal integration and averaging. Above we referred to the digital signal averaging algorithm as one consideration for choosing a value for T_{samp}; here are some other considerations. Smaller values of T_{samp} require higher sampling rates; and the associated averaging times are decreased, leading to wider receiver bandwidths with associated higher noise levels. Higher noise levels can degrade spatial resolution. Equation [13] tells us that smaller values of T_{samp} increase redundancy. What are there implications of various redundancy values. To address this question, we must first know how to interpret values for $\mathbf{f}$.

For *integer* values, the interpretation given above seems adequate: it is the number of sampling windows in which scattering from any given point appears. But what of *non-integer* values? You should understand that *non-integer* values of $\mathbf{f}$ imply *non-uniform* spatial sampling. For example, $\mathbf{f = 1.2}$ means every spatial point is sampled once; but 20% of the points are sampled twice. Thus, space is partitioned into two component regions, each having *different* degrees of sampling. In fact these regions alternate in space with the periodicity of Δz_{shift} (c.f. Appendix B). The location of these partitions happen to be set arbitrarily by the phase relation of the sampling gate to the pulse emission time. Since these partitions have no special physical significance, biasing the sampling there is inappropriate. Instead, for *integer* values of $\mathbf{f}$, every spatial point along the propagation line is *uniformly* sampled. For large values of $\mathbf{f}$, this non-uniformity is of little consequence, since the bias between $\mathbf{f = n}$ and $\mathbf{f = n+1}$ can be neglected for large $\mathbf{n}$. But for small values, the bias can be considerable.

4. Component Development and Testing

To introduce this section, we provide some values for the design parameters of our system. These provide a context in which you can consider the discussions of various subsystems in this section. In our system design we chose the compromise value of $T_{\mathbf{samp}} = 31\mu\text{sec} \cong 0.05\tau$, for which, from equation [13], $f \cong 20$. Then each point in space is sampled twenty times in successive samples. We used this value, the highest possible for our A/D convertor, in all of our experiments.

For the LASERs that we use in these experiments (c.f. SECTION 4.1: COMPONENT DEVELOPMENT AND TESTING - SOURCES), the pulse length $\tau = 700\text{ns}$. Using this value, together with the value for $T_{\mathbf{samp}}$ from above, in equation [x12] leads to a value for the length of the sampling volume of

$$\Delta z_{samp} = \frac{c}{2}[\tau + \tau] = \frac{3.0 \times 10^8 \text{ m/sec}}{2}[2\ (7 \times 10^{-7} \text{ sec})] = 210\text{m}$$

By the Nyquist criterion [eq. 12], this design limits the spatial resolution for profiling to a value

$$\lambda_{spatial} \geq (2c\tau/2) = c\tau = 210\text{m}$$

Thus, this limit is the same value as the length of the sampling volume that we just calculated.

Equation [11] is the relation for the received power $\mathbf{P_r}$ in terms of the source pulse energy $\mathbf{\mathcal{E}_0}$. We can use it to make an estimate of how much Rayleigh scattering to expect in the "worst case" for our LIDAR system. This case is when the LIDAR range is **10km**, pointed vertically, and the wavelength is that needed for water detection. We use a pulse of energy $\mathbf{\mathcal{E}_0 = 1\ joule}$ and consider the case of source radiation having $\lambda \sim 720\text{nm}$. Our aperture of diameter = 1m (i.e. $\Delta\mathbf{A_r} \cong 0.8\ \text{m}^2$) receives the scattering from a range distance of $\mathbf{z(t)} = 10\text{km}$. Using equation [5], which we have evaluated in SECTION 3, for the scattering conditions of the atmosphere at sea level, we obtain the scattering coefficient

$$\beta_\pi^R = 0.5 \times 10^{-8}\ \text{cm}^{-1}\ \text{sr}^{-1} \text{ @ } \lambda \sim 720\text{nm}$$

The received power from air at *sea level density* is then

$$\mathbf{P}_r = 1\ \text{joule}\left[1.5 \times 10^{10}\ \frac{\text{cm}}{\text{sec}}\right]\left[\frac{0.8\ \text{m}^2}{(10^4\ \text{m})^2}\ \text{sr}\right][0.5 \times 10^{-8}\ \text{cm}^{-1}\ \text{sr}^{-1}]$$

$$\mathbf{P}_r = 0.6\ \mu\text{watts}$$

We may adjust this estimate to received power from air at 10 km by noting that the scattered power is directly proportional to the target density. For the U.S. Standard Atmosphere, Table [1] gives the densities at various altitudes. Relative to sea level, the density at 11km is[15]

$$\frac{0.36\frac{kg}{m^3}}{1.22\frac{kg}{m^3}} = 0.30$$

Thus the adjusted estimate for the received scattered power is

$$\mathcal{P}_r = 0.30 \ (0.6\ \mu\text{watts}) = 0.18\ \mu\text{watts} \ @\ h = 10\text{km}$$

This translates into a number of photons/sec given by the following.

$$\mathcal{P}_r = \frac{0.18\ \mu\text{watts}}{(hc/\lambda)}$$

$$= \frac{0.18 \times 10^{-6}}{6.6 \times 10^{-34} \times 3.0 \times 10^{8}} \times (7.2 \times 10^{-7}) \text{ photons/sec} \ @\ \lambda\sim 720\text{nm}$$

$$\mathcal{P}_r \cong 7 \times 10^{11} \text{ photons/sec}$$

Finally, we must include reduction factors that account for optical energy lost in transmission and reception due to absorption by non-ideal reflective surfaces in the optical path. We somewhat arbitrarily use a figure of 20% transmission for the outgoing pulse, and the same figure for the incoming, scattered energy. This introduces a net, optical transmission factor of T= 0.04. Beyond this, there is the detector efficiency. For a silicon diode, efficiencies of order unity are achievable at this wavelength. Thus,

$$[\mathcal{P}_r]_{net} = 0.04 \times 0.18\ \mu\text{watts} = 7 \text{ nanowatts}$$

But for photomultiplier tubes, which we may need to use for photon counting of received powers at the lower edge of our estimates above, we need to reckon with PMT photocathode efficiencies which are about 20% at this wavelength. Thus, for photon counting of the highest rate

$$[\mathcal{P}_r]_{net} \cong 0.04 \times 0.20 \times 7 \times 10^{11} \text{ photons/sec} \cong 6 \times 10^{9} \text{ photons/sec}$$

This is *just* above the rates at which standard counting equipment can operate. Thus, we must do photon counting only if the "worst case" estimates above are too optimistic.

4.1. Sources

The LIDAR systems that we wish to develop must use pulsed LASERs as signal sources. At the beginning of this project we had on hand a pair of Candela CL-1200, quadraxial, water-cooled, flashlamp-pumped dye cells, each mounted on an ED-1000 driver circuit and together capable of handling up to 25 KV from a single HVD-200 power supply. This power supply is capable of delivering enough electrical energy to the pair of drivers to operate at a repetition rate of about one pulse per 5 seconds. For operation of a single driver, this maximum repetition rate could be one pulse per $2\frac{1}{2}$ seconds. There is a DCR-20L dye/water chiller which holds an approximate 4 liters of water and 2-10 liters of dye in appropriate reserviors. It cools these sufficiently and delivers them to the LASER tubes, at a pressure head of a few feet, sufficiently to permit operation as specified above. All of these items are manufactured by Candela.

Each ED-1000 Driver has a pair of 1.5μf capacitors in a Marx bank configuration in which they are charged (up to 25KV) in parallel and discharged, by self-contained spark gaps, in series (applying 50KV) through a quartz, xenon-filled flashlamp surrounding the 21mm diameter dye cell coaxially. The driver therefore stores about 1 kilojoule for discharge through the lamp on each pulse. For high efficiency dyes like Rhodamine-6G or Coumarin-504, this system produces broadband (red or blue-green) LASER radiation in about 1 joule pulses with lengths of just under 1 μsecond. The peak power of these pulses just over 1 megawatt; and their irradiance is about 800kW/cm^2 in a naturally collimated beam area of 1.8cm^2.

All of the various components of the LIDAR system, starting from the dye LASER where the source light pulses originate, act upon the beam of those pulses. Consequently, each optical surface of each of those components needs to meet the beam at the proper position and angle. To facilitate the proper positioning of these components with respect to the beam we use an *alignment* LASER. For the development systems, this LASER is a HeNe whose red light can propagate through the reflective end mirrors on the dye LASER cavity. There is sufficient reflectivity at the folding mirrors, however, to that this alignment beam continues to trace the source beam's path through space beyond the folding optics. We achieve congruence of the alignment and source LASERs' light beams by adjusting the alignment beam so that it passes through the dye cell's center. We check this by watching the alignment beam strike cross-hairs positioned at both ends of this cylindrical cell. This collocation procedure also assures collinearity between the two beams. For first-time setup, all this is accomplished with the cavity mirrors removed (but the dye cell windows in place); thereafter we may check collocation without removing the end mirrors. In setting up and maintaining the remaining optical components, we always use this alignment LASER beam as a reference with respect to which we may position and orient all optical surfaces.

4.1.1. Requirements

The requirements of the operational LIDAR system dictates the characteristics of the candidate LASER sources. We wish these systems to detect specific gases in the atmosphere, so they must operate with some form of spectroscopic discrimination. SECTION 2.1: LIDAR PRINCIPLES; THE DIAL describes how our system achieves such

discrimination using spectral absorption features of the target gas. Of the gases of interest, water vapor is an important target candidate. Our DIAL must operate at/near the IR wavelength region of the optical spectrum in order to utilize the water molecular spectrum while preserving the advantage in Rayleigh scattering afforded by shorter wavelengths. We wish to take advantage of narrow absorption lines of water for discriminating against all other molecules in the target volume. [Fig.7] shows the relevant part of the H_20 absorption spectrum.[16] Since the line widths there (FW@HM) are about $(\Delta\lambda/\lambda) = 2 \times 10^{-5}$, we must use a source LASER having a line widths of order $(\Delta\lambda/\lambda) = 2 \times 10^{-6}$. This value corresponds to the line width specification of the "baseline" LASER system used in the AMOS LIDAR report.[17] Also from that report, the baseline LASER average power is 1 watt. Using a LASER operating at this power level, this report's analyses confirm that a DIAL system can measure column water contents to accuracies in the 1-10% range.

4.1.2. Configuration

[Fig.8] shows the basic Candela CL-1200 flashlamp-pumped dye LASER tube. It has a coaxial flashlamp surrounding a cylindrical dye cell. In a coaxial arrangement, situated between the flashlamp and the dye cell, there is a water-filled cooling jacket that is actually part of the flashlamp. The purpose of this jacket is to cool the flashlamp. Within the dye cell, there is another coaxial, cylindrical tube surrounding the cylinder of dye solution, an evacuated sheath situated between the water jacket and the dye. The purpose of this sheath is to thermally insulate the dye solution from the cooling jacket. This design insures that the water will *not* cool the dye solution within the active cell; for to do so would cause thermal, hence density, gradients there that could distort the resonating optical beam. Instead, the dye is cooled outside of the active cell, by a counter-current heat exchanger in the circulator/chiller unit. This four-fold coaxial arrangement of lamp, coolant, vacuum, and dye is the reason for naming this LASER tube design "quadraxial". It is especially intended for maximum power operation. The LASER tube's dye cell has end-windows which are slightly wedged (30') and coated for anti-reflection near the intended LASER operating wavelength. For all the experiments upon which we report in this document, we operated the LASER using Coumarin 504 dye, which has a lasing peak in the blue-green near 504 nanometers.

The LASER tube is mounted between two plane mirrors which form a **plane-parallel resonator** cavity. [Fig.9] shows the arrangement of these elements for the development LASER we used a total, plane reflector at one end, and a 20% reflective, plane output coupler at the other. Both these elements have dielectric reflective coatings which peak broadly at these reflectances for $\lambda \sim 500$nm. With only these mirrors in place, the resonator LASEs in mode whose bandwidth is determined by the dye gain spectral curve. For the Coumarin 504 dye in solution, this instrument LASEd with almost no tuning effort once we reached a comfortable (HV~15kilovolt) level on the flashlamp, even though we were using only a modest (~10% optimal) concentration of Coumarin dye. This arrangement produces a multimode beam with $\lambda \sim$ 500nm. We did not measure the spectrum of this broadband output. However, for this dye the spectral gain curve[18] for coxial flashlamp pumping shows a peak at $\lambda \sim 500$nm and $\Delta\lambda \cong 45$nm (viz. $\Delta\lambda/\lambda \cong 9\%$ @FWHM) linewidth. Compared to the *required* linewidth

($\Delta\lambda/\lambda = 2 \times 10^{-6}$), this linewidth indicates a need for considerably fine tuning capability to make this LASER a candidate for a DIAL.

An *optimal* dye concentration is that which produces a (1/e) attenuation of maximally absorbed light across a transverse radius of the dye cell. Here, for the (~2cm) diameter dye cell, this optimal concentration, expressed as the molarity of the dye solution, must be

$$c_o = \frac{1}{1\text{cm}\cdot A}$$

where $A = 4.7\times10^4$ liter/mole•cm is the extinction coefficient/mole of the dye solution in $(\text{M}\cdot\text{cm})^{-1}$ evaluated at the wavelength $\lambda = 436$nm, where absorption is maximal. This molar concentration, $M_o = 2.1\times10^{-5}$ M is very nearly the threshold concentration for LASing in our system, i.e. the *minimum concentration* at the *minimum* flashlamp *pumping power* (16KV) for which the system will *just* LASE. The maximum solubility of Coumarin 504 gives a (saturated) solution at concentration of $c_{max} = 4\times10^{-2}$M, so that we were working here with fairly dilute solutions.

From the small concentrations of dye required and the robustness of the LASing action, this system is clearly almost superradiant (i.e. LASEs without any resononator). We conducted a series of cavity-tuning experiments where we optimized the output energy as a function of adjustments to the parallelism of the end mirrors. We found that we could not adequately conduct quantitative, cavity alignment, optimization experiments using the hand-operated micrometer positioners provided by Candela. For the (θ, Φ) orientational controls, we replaced these micrometers with electrical servo-driven micrometers made by NRC. In turn, an NRC Model 815 Controller drives the micrometers; and an IBM-PC drives the 815 Controller through an IEEE-488 instrument/computer interface. Since either one, but only one, of the cavity mirrors needs to be adjusted to produce parallel alignment, we chose to operate the total reflector. We use a HeNe LASER to produce a reflection from the *back* of this element to monitor its orientation and movement directly, in addition to having such information indirectly from the Model 815 Controller. This is the same LASER, called the *alignment* LASER and described above, that we use for general alignment of all the LIDAR system components.

We designed our own control programs to operate this instrumentation for pointing the total reflector and hence controlling the plane-plane cavity alignment. A separate report[19] describes this configuration more fully and the details of the cavity alignment process. With the cavity properly aligned we obtained LASER pulses of several hundred millijoules for extended periods (several hundred pulses) before the cavity could benefit from further tuning adjustments. We discovered that an intrinsic decrease of pulse energy with continued operation was a more serious problem, than resonator alignment, to sustained operation.

4.1.3. Performance

The intrinsic decrease in LASER efficiency that we uncovered in our studies of resonator alignment led us to an awareness of dye photodegradation effects. As early as January 1986, we initiated studies on this problem. This was before we implemented the servo-driven cavity alignment instrumentation. We decided that we had to install this capability only after we obtained inconsistent results in the preliminary dye degradation studies. Thus it was not until the following year that we had completed the studies and

presented a preliminary report.[20] This work subsequently received an USAF Service Award for Technical Achievement in In-house Research.[21]

The energy distribution in the pulse wavelength spectrum is a fundamental limitation to achieving spectral discrimination. For example, for DIAL (differential absorption LIDAR) technique we must operate the LASER source with a linewidth at least as narrow as the spectral absorption feature that we are using to measure the target molecule. We believe that we can operate the high power dye LASERs at the AOTF at quite narrow linewidths ($\Delta\lambda/\lambda = 2 \times 10^{-6}$) by inserting etalon tuning elements into the dye LASER cavity to control the linewidth of the LASER pulse. To achieve these linewidths using dyes which have relatively broad lasing-gain curves ($\Delta\lambda/\lambda = 0.1$), we must consider using multiple, cascaded etalon filters in the optical cavity.[22] To monitor this intra-cavity tuning, we must configure an optical spectrometer capable of resolving the spectral shape of the pulsed LASER light to this precision [c.f. SECTION 4.2: OUTPUT BEAM DIAGNOSTICS]. To design and test the etalons for insertion, we had to devise a method of measuring their tuning response. We describe this in a separate report.[23]

In addition to generating source light with the requisite linewidth, its line center must coincide with the spectral absorption feature of the target molecule. Consequently, we must have capability to establish the center line wavelength of the source radiation [c.f. SECTION 4.2: OUTPUT BEAM DIAGNOSTICS]. This part of the work, to achieve LASER spectral performance requisite for a DIAL, was especially difficult; and our original project plan specified it would be done by a post-doctoral appointee recruited specifically for this purpose. This staff addition was not forthcoming and this portion of the work lagged throughout the project.

4.2. Output Beam Diagnostics

For the development work and LIDAR operation, we need to monitor and/or measure several qualities of the LASER and system output radiation. On various occasions we are interested in the spatial and temporal distributions of optical energy in the LASER pulses; or in their relative spectral distribution, or even their absolute spectral distribution for the DIAL application; or in their output energy, sometimes relatively and other times absolutely. We also are interested in the output beam trajectory and collimation properties, which we treat in SECTION 4.3: EXIT OPTICS. In this section, we report on the design and operation of several specialized instruments which serve some of the needs that we have just described.

4.2.1. Pulse energy measurements.

For LASER development work we need to know the absolute output pulse energy in order to monitor and optimize LASER performance. For the LIDAR development work we need to know relative energy of individual source pulses to normalize the return signal data. Since each LASER pulse has, in general, a different energy, the return scattering from each source pulse must be appropriately weighted if all are to be averaged, and if they are to be used in ratios with other pulses as the DIAL technique requires. We acquired aLASER power/energy meter (Scientec Model 38-0101: Volume Absorbing Disc Calorimeter) for directly measuring the energy of the dye LASER output pulses. This instrument converts the incident light to thermal energy in order to measure the optical

pulse energy or the optical CW power. We can calibrate this instrument absolutely using a coil, imbedded in the sensor, which delivers electrical energy to heat the sensor in the same manner as does the incident LASER radiation.[24] We deployed this instrument in two ways, as shown in [Fig.10]. We used this instrument in preliminary LASER experiments, and to calibrate a secondary, photodetector sensor for use in further LASER experiments and in LIDAR operations.

We must deal with hundreds of LASER shots in any experiment or DIAL measurement. Consequently, we need to have the computer automatically record the energy meter readings from all output pulses. The Scientec instrument uses a serial interface, similar to the RS-232c standard, to accomplish this. We had to modify the cabling arrangement so that this system would operated as designed in the "hostile" environment of our laboratory where the high-energy LASER flashlamp together with its power supply and driver electronics produce considerable RF noise. We successed by installing improved shielding on all energy meter communication lines, by improving the grounding of the meter housing itself, and by judicious placement of the signal line connecting the detector head with the meter housing.

4.2.2. Spectral energy distribution measurements.

We adapted an existing design for a narrow-band spectrometer to use as a diagnostic wavemeter. This grating spectrometer is described by Morris and McIlrath.[25] It uses an echelle grating in an Ebert "over-and-under" configuration, and a photodiode array to measure the output. This spectrometer/wavemeter, with a theoretical spectral resolution of ($\Delta\lambda/\lambda = 10^{-4}$), is insufficient to evaluate the source spectral purity spectral to the degree required for some of the more critical LIDAR applications. But it is sufficient to check many aspects of LIDAR system operation, and to approximate the capabilities required for those more critical applications. In particular, it is completely sufficient for the outdoor tests in the atmosphere of the integrated LIDAR development system (LASER/scattering/detector) where we intend to use, in the most finely tuned version, only the single-etalon tuned LASER source.

In its original version, the photodiode array that is the detection element in the spectrometer is "read out" in the form of an oscilloscope display that is synchronized with the trace. We designed and developed our own computerized interface for this detector element.[26] This interface to the computer is controlled by a microprocessor, hence "intelligent". We describe it in somewhat more detail in SECTION 4.6.2: SPECTROMETER/FIRING CONTROL COMPUTER. Our design adds flexibility to the LASER development environment, for example permitting us to use this same detector array as a spatial profilometer of the source LASER output beam. Another such example is the use of this detector array in etalon tuning studies that we describe below. But the interface also greatly simplifies the application of this instrument as a monitoring wavemeter in the LIDAR development environment. It is primarily in this important respect, the interface, that our design differs from the original by Morris and McIlrath.

At this point, we have constructed our spectrometer and calibrated it.[27] The results indicate that it is operating satisfactorily, subject to special precautions necessary to avoid a systematic error from "phase jumping" in the digital readout. In this situation, the pixel

sequence becomes confused because the pixel information at some point in the readout sequence is not available to the microprocessor, and the previous value is "twice read".

We conducted a series of experiments to validate the spectral filter characteristics of our high-power LASER tuning etalons, under low power conditions.[28] Relatively low power, cw Argon (λ=544nm) and HeNe (λ=633nm) LASERs illuminate the etalons in these experiments. These experiments use our flexible, microprocessor-controlled, photodiode array as a detector of each etalon's Fabry-Perot fringe pattern, which is a spatial intensity distrubution. This use is in precisely the same manner as it would be for the beam spatial profiling diagnostic measurements mentioned above.

Preliminary LASER tuning studies just began. Our objectives were to operate with a single, coarse intra-cavity etalon to narrow the LASing bandwidth from the broadband of the natural dye gain (tuning) curve to the line profile of this etalon. As of yet, we have not been able to achieve successful lasing action with this etalon in place. Our failure to achieve narrowband LASing means that we have not been able to test, yet, the pulsed operation of the diagnostic wavemeter. This is because the free spectral range of our narrow-band spectrometer is insufficient to accomodate the spectral width of the broadband LASER output.

In order to operate many LIDAR systems, we must know the track the precise wavelength of the LASER during long operational runs; and we must also monitor its bandwidth. In order to do these things, we have need greater resolution than that provided by the kind of spectrometer we describe above. Accordingly, we have obtained a high-precision, commercial Fabry-Perot interferometer and tested it for future inclusion as a diagnostic tool for our systems. The "read-out" device for this instrument will be, as in the etalon tuning experimental setup, the microprocessor-controlled, photodiode array. Results of our preliminary experiments verify that this read-out methodology will work.

4.3. Exit Optics

This section discusses the optical components which carry the LASER output through the diagnostic sampling elements all the way out to the field. Transfer optics carry the output beam from the source LASER to diagnostic instruments; also to beam expander and thence to the telescope axis for propagation outward. This path is separated into two sections by the beam expander. The first section, before beam expansion, has high beam intensity and is called the high-power section. After expansion, the intensity drops and the remaining path to the field is called the low-power section. This common terminology, strictly speaking, is a misnomer; the power (except for interface losses) is actually constant throughout; only the power per area (irradiance) decreases between the two sections. Nontheless, this is the terminology we have adopted and continue to use here. [Fig.11] depicts, in schematic representation, the elements in the optical train of the exiting LASER pulses in our developmental LIDAR.

4.3.1. High-Power Section

First in line starting from the LASER source are beam samplers (low reflectivity splitters) which extract about 5% of the beam energy and direct it toward diagnostic instruments. One of these instruments is the spectrometer; another is the pulse energy detector. We

call these directive elements the sampling optics. In the transmitting path beyond the samplers, we needed an additional fold mirror to direct the beam into the expander. The beam at this point is about 15mm in diameter and, in full power operation, each pulse could have 1 Joule of energy in a 700ns pulse. This combination effects about 1 Megawatt/cm^2 of irradiance. Thus all folding optics in this part of the beam, including the samplers, must have high-power dielectric coatings and be kept relatively clean if they are to survive each pulse undamaged. In the reflective paths beyond the samplers, however, the irradiance levels are sufficiently decreased that special, high-power coatings are probably not necessary. All of the optical elements in the main beam are coated for anti-reflection at the appropriate wavelength. For the development versions of our LIDAR, the center wavelength for these coatings is λ=500nm. All these coatings are rated to tolerate fluences of at least 1.5 Mw/cm^2. We ordered two different sets of beam samplers and folding mirrors for our experiments: one set to operate at λ=500nm and the other at λ=700nm wavelengths. At this point the beam enters the expander, leaving the high-power section.

Depending upon the particular geography of supporting tables and space, delivery of the sampled radiation to the diagnostic instruments may require one or more fold optics beyond the samplers. These will be mirror flats which need not have high-power coatings. However, you may find it desirable to have all folding mirrors to the energy meter be broadband, "total" reflectors at all of the operating wavelengths, in lieu of dielectric reflective coatings, which tend to be wavelength selective.

4.3.2. Low-Power Section.

As the beam enters the expander, it leaves the high-power section. Exiting the expander, the beam is turned by three fold mirrors which position behind the secondary mirror of the main receiving telescope, and align it with that telescope's axis. The beam at this point is now centered on and collinear with the main telescope's line-of-view, achieving a monostatic LIDAR geometry. Finally, a coelostat on the top of the AOTF observatory dome directs the LIDAR's line-of-view anywhere in the upper hemisphere, above the viewing horizon. In fact, it actually can lower the line-of-view beneath the horizon to contact ground targets situated anywhere in the testing fields surrounding the AOTF.

4.3.2.1. Beam Expander

Next in line, a high-power beam expander enlarges and collimates the main output beam in order to reduce its power density and obviate the need for high-energy optical elements in the succeeding portions of the system. This beam expander thus forms the divide between the high and low energy density segments of the output system. The design for this expander is an off-axis paraboliod, which affords a good expansion ratio (10:1) without a central obscuration which would remove some of the beam energy. It also preserves the propagation direction of the entrance beam in the exit beam.

The Space Optics Research Laboratory (SORL) produced this unit, which is essentially their Model COAR 10X15-HQ-C. Unfortunately, this instrument's standard design has a nominal 10mm entrance aperture, and thus does not quite accomodate the periphery of our LASER beam. This vignettes the main output beam by about 50%. However, if instrument increasing efficiency becomes a priority, we feel that some properly engineered combination of "prefocus" with a convergent, high-power mirror, matched to

a corresponding accomodation with the expander collimation adjustment, should be able to increase the system throughput. Because this optimization was not among our prime goals, we did nothing to address this issue.

The optics of the (x10) beam expander/collimator are specially coated to operate at both 500nm and 700nm. wavelengths. This combination permits us to experiment with the LIDAR development system in the visible region, but enables us to switch to the near-IR for experiments in the wavelength regime of our water targets. The rationale for double-coating the expander but not the folding optics is that this special coating is quite expensive, and ought to be restricted to elements that are difficult and time-consuming to change when we want to switch operating wavelengths. Only the beam expander meets this criterion.

4.3.2.2. Folding Optics

Next, a set of three, low-power, folding mirrors directs the expanded beam around the receiving telescope's primary mirror to a point behind its secondary mirror, and thence into a line coaxial with the telescope's line of sight. [Fig.12] shows the structural details of the telescope taken from the plan for that instrument.[29] This permits you to picture the relative positions of the three folding mirrors, which positions we describe further below. [Fig.13] depicts the dimensions and distances more clearly than the structural diagram. All these mirrors are 15.2cm flats, and are nomimally oriented at 45° to the beam, in order to change its direction by 90°. This means that the "clear aperture" of these optics in this orientation is $\sqrt{2} \times 15.2\text{cm} = 10.8\text{cm}$. Because the expanded beam has a nominal diameter of 10.0cm, these apertures are sufficient to pass the beam without vignetting. However, the positioning tolerances are tight.

The first folding flat is located at the 1 meter level, just inside the sloping, lower truss support. It is less than 1m from the exit port of the beam expander. The second flat is at the "A-level" (c.f. [Fig.12]) and its mounting is fastened to the upper truss structure of the telescope there. The third flat is located just behind (i.e. above) the telescope secondary mirror assembly. Its mounting is supported by a narrow beam that runs horizontally to the floor of the AOTF which is located very near the telescope's "A-level". The first and third of these three fold mirrors have (θ, Φ) orientational adjustments in their mounts to control the direction of reflection.

From this point on, the coelostat mirrors form a beam director which controls both the output beam's line of propagation and the telescope's line of sight. If these lines are well co-aligned, this arrangement constitutes a monostatic configuration for the LIDAR development system. We calculate that the reduced (1/100) irradiance of the expanded output beam, even if we operate our LASER at maximum power, is safe for the existing coatings on our coelostat flats.

In addition to the directional attitude of the outgoing beam, we are concerned with its collimation. After emerging from the beam expander, the beam may not be perfectly collimated. The SORL Model COAR 10X15-HQ-C has an adjustment to trim the collimation of the exiting, expanded beam. In order to exploit this adjustment, we must have a means of measuring the collimation of the beam beyond the expander. We developed our own method for doing this, which also serves to bore-sight the LIDAR's line-of-view.

4.3.3. Boresight/collimation Diagnostic Prodedures

The tasks of aligning the LIDAR within its FOV (field of view) and aiming it are related to the task of collimating the output beam, because both concern determining the propagation direction of rays in the beam. The latter concerns the direction output rays relative to one another; while the former concerns the direction of all the rays, as a whole, relative to the optical axis of the system. Note that the output's propagation direction is uniquely defined only if it is a collimated beam. Our method of boresight alignment uses a retroreflector to return an alignment beam. Our method of collimation testing also uses a retroreflector to return the autocollimation test beam. The former is a simple expedient for boresighting when your system already has a collimated alignment beam defining the system axis (c.f. SECTION 4.1: SOURCES). The latter is useful when you have a large system, whose output points where you wish to test collimation do not readily allow coordination between the viewer with the autocollimator telescope and the adjuster of the return mirror at the beam's test point.

[Fig.14] depicts the optical arrangement that achieves our boresight alignment and beam collimation diagnostics. Our test system consists of: a sighting telescope, with cross-hair eyepiece, focussed at infinity; a pellicle beamsplitter with orientational and one degree of translational adjustment capability at **A**; a folding mirror or a retroreflector at **B** which can be temporarily inserted in, then withdrawn, from the beam; a retroreflector which can be positioned and subsquently moved to sample the output beam across its aperture at **C**; and, as an option, another pellicle beamsplitter with orientational and one degree of translational adjustment capability at **D**, to introduce a second alignment LASER beam having a different wavelength than the main LASER's alignment beam. The latter might be necessary due to wavelength selective reflectivities in the system folding optics and/or beam expander.

4.3.3.1. Boresighting

The operating principles for the boresight diagnostic of this system are as follows. The sighting telescope must have its cross-hairs set at its primary focus. A retroreflector inserted in the alignment LASER's beam at **B** returns the aligment beam to a beam splitter at **A**, and subsequently to the sighting telescope. A pellicle is necessary for this splitter in order to avoid a lateral shift in the outgoing alignment beam that would spoil alignment during high-power operation when we remove this splitter for the sake of efficiency. The retro return may be offset from the outgoing alignment beam, but parallel to it. Thus, the alignment telescope will look down this retro return in exactly the same sense it looks out along the alignment beam; but it may be laterally displaced somewhat from the alignment beam and hence the from the system axis.

The operating procedures for the boresight diagnostic of this system are as follows. Set the sighting telescope's cross-hairs at the image of an object located at "infinity". Do this by sighting on a very distant object, and then adjusting the longitudinal position of the cross-hairs, relative to the telescope's objective lens. The cross-hairs are at the image's location when there is no parallax between them. Install the sighting telescope, aside the beamsplitter at **A**, in order to catch the return from the retroreflector inserted in the alignment beam at **B**. Since any offset in this return will affect the lateral position of the sighting telescope's line-of-sight, we advise minimizing this offset by adjusting the retro

to intercept the alignment beam near the retro's vertex. Then adjust the cross-hairs and/or the orientation of the splitter and/or the position/orientation of the telescope to collocate the image of the alignment beam with cross-hairs. Once you do this, removing the retro and looking out the sighting telescope will reveal what the LIDAR output is aimed at. The target is in the cross-hairs.

4.3.3.2. Collimation

The operating principles for the collimation diagnostic of this system are as follows. The sighting telescope also serves as an autocollimation telescope. If the exit optics, including the beam expander, are insufficiently reflective at the alignment LASER's wavelength, we must insert a second, auxiliary LASER via an adjustable beamsplitter at **D** and coalign it to the alignment LASER. This beamsplitter must be a pellicle also to avoid offsetting the high-power LASER beam during operation when we remove this auxiliary splitter. The collimation test beam is either of these beams after passing through the beam expander and/or other exit optics. A retroreflector at the expanded collimation test beam's sample point returns a portion of that beam either back into the output system or over into the receiver system, depending upon the retro's sampling location. The return going back into the output system permits the sighting telescope to evaluate the quality of the expander's collimation by means of an autocollimation check. The return beam going over into the receiver system permits a focal plane test to determine the location of the LIDAR's "infinity" image spot.

The operating procedures for the collimation diagnostic of this system are as follows. Set the sighting telescope for boresighting, as we have described above. If the folding and beam expander's optics do not reflect sufficiently at the alignment LASER's wavelength, then introduce another, auxiliary LASER to supplement the alignment beam. Optical power is more critical after you expand the test beam because our expander reduces the power *density*, and hence visibility, by a factor of (1/100). Moreover, each reflecting surface affects the test beam *twice* because it is returned along the optical path for diagnostic purposes. The auxiliary's insertion point is **D**. Aim the auxiliary LASER so that it crosses the main alignment LASER's beam in the vicinity of the splitter there. To collocate these two beams, first install a temporary fold mirror at **B** to deflect these beams away from the expander and to a sighting target. The longer you make this common path, the more precisely you can collocate them. Now alternately adjust the position of the splitter and the orientation of the splitter. The former controls the lateral location of the beam and you should be checking collocation near the splitter when making this adjustment. The latter controls the orientation of the beam and you should be checking collocation at the distant sighting target when making this adjustment. By iteration, you should be able to optimize the collocation at these two, distant points simultaneously, thereby forcing the beams into the same location along their entire length. Now remove the splitter at **B**, permitting the combined beams to enter the expander, before proceeding.

The beam expander also adjusts the collimation of the exiting, expanded beam. To test the quality of this collimation, insert a retroreflector into that test beam at some sample point. If this point lies beyond the exit optics, in the "field", then be sure that the retro position is entirely within output beam, so that the return comes back into the expander, and thence into the sighting telescope via the splitter at **A**. The retro preserves any

(residual) local curvature from the test beam in the return that it produces. When that return enters the sighting telescope, now being used as an autocollimation tester, it will image at some location in front of, in back of, or at the cross-hairs. You can check the relative location of these two by looking for parallax between them. Perfect coincidence means perfect collimation, at least for that spatial portion of the beam included in the sample. Adjust the collimation of the beam expander until you achieve the minimum parallax.

You may subsequently use the same setup as for collimation testing, to align the receiving optics. If you position the retroreflector so that half of it samples the test output beam at its edge, then retro return will be offset over into the field of view of the receiving optics provided that the retroreflector's aperture is sufficient to bypass the central obscuration of the receiving telescope. Once the return is so directed, you can locate the receiver focus by the location of that return's image. This arrangement is useful for adjusting the position of the detector so that the LIDAR returns will be properly directed to it.

4.4. Receiver Optics

The coelostat directs the returning signal light into the telescope primary. Near the principal focus of this Cassegrain arrangement, transfer optics direct this return light onto a photodetector. We had some preliminary concerns about stray light intrusion, and so we placed some rudimentary shielding around the transfer optics portion of this return light path. In our first successful, experiments with the LIDAR development system (c.f. SECTION 5: SYSTEMS INTEGRATION AND TESTING) we found some promise in using a single photodiode as the sole detector, although these tests ranged only to 1.6km. In order for this scheme to accomodate the weakest anticipated return signals, the photodiode size must be very small in order to limit dark current noise which grows with the size of the photodiode. This size restriction presents some practical problems in securing the requisite beam alignment and stability to insure that the return image does not wander off the detector as the pulse propagates outward. Most especially, in a DIAL configuration, the two requisite signal paths (i.e. the off-line/on-line beam geometries) must have identical spatial relationships to the detector. Our success with the photodiode alone will depend upon how well we can focus the far-field return signal so as to capture it entirely, which capability we can only evaluate experimentally.

However, these early experimental results also indicated that some of the outgoing source pulse, promptly scattered from the locale and transmitting optics (many of which in the monostatic configuration are shared with the receiving optics), reach the detector in sufficient intensity to overdrive the receiver (c.f. SECTION 4.5: DETECTOR and SECTION 5: SYSTEMS INTEGRATION AND TESTING). This assault of parasitic light immobilizes the receiver for an unacceptably long duration of time after the output pulse leaves the system. Unacceptable means that we cannot measure the field return from at least the first several hundred meters. Thus, we realize that we need to provide some sort of protection against this effect.

A conventional method of dealing with parasitic light is by shuttering the detector during output pulse launch. We want to insert a field stop which excludes all light, except from the telescope's field of view; and then only admit light when the shutter is open. Thus the shutter must be closed when the LASER is first fired; and then be quickly opened, when

the pulse has cleared the LIDAR apparatus where it scatters parasitically, to receive functional scattering from the field. Fixing the moment in time that the shutter opens is crucial to its success at excluding undesired, parasitic light during the first part of the pulse flight, while admitting the desired return signal before the pulse has travelled too far from the LIDAR. The intervening space, where the pulse travels before the shutter opens, is "blind" to the LIDAR.

The shutters we wish to consider are essentially mechanical and move transversely to the received light. In this context, the time it takes the shutter to open ($\tau_{\mathbf{open}}$) and the moment in time ($\mathbf{T_{open}}$) at which the shutter opens are of crucial importance in determining whether the shutter achieves its purpose. [Fig.15] depicts the timing of events in the shutter opening sequence. Here, we assume the shutter is stationary both before and after opening. This is typical of a leaf shutter. In this case, we need to allow time and distance for the shutter to accelerate to its maximum speed before it crosses the return beam aperture. This requires that we anticipate the opening moment $\mathbf{t = T_{open}}$ by initiating the shutter movement from $\mathbf{y = 0}$ at $\mathbf{t = t_1}$. The shutter accelerates so that it is moving at maximum speed by the time it reaches the return beam aperture at $\mathbf{t = T_{open}}$. The opening action proceeds to full aperture during the period $\Delta\mathbf{t} = \tau_{\mathbf{open}}$. The shutter then decelerates until at $\mathbf{t = t_4}$ it is in its final (rest) position $\mathbf{y = y_{max}}$. For a rotating shutter, which moves at constant speed, no acceleration periods are needed in the opening sequence, and the timing requirements are much simpler.

To conceive of how and where we should shutter the beam, we should think of the return signal receiving process, involving the main telescope, as an imaging process. This telescope forms an "image" of the field "object", in this case the scattering, outgoing pulse. For reasons of economy in size and speed, we want to locate the field stop for the shutter at a position in the return beam where it is narrowest. This beam will be narrowest at the position it forms the pulse's image. Through the journey of the outbound pulse, the main telescope collects the light scattered from the volume occupied by the LASER pulse at any given moment. This scattered light from the pulse optically acts just like an illuminated object, broadcasting light in all directions. Since this object volume moves *away* from the primary mirror with time, its (real) image moves *toward* that mirror, in particular toward its focal plane. (This is a fundamental principal in geometric optics.) At the same time, that image is becoming smaller as the object retreats. Thus, with time, the return beam must be changing its size overall, plus shifting the location of its narrowest point. If we agree to consider only fixed stops as possibilities for shuttering, we want to know which location and size for the stop are the best compromise so that the receiver accepts the return beam in a satisfactory way. More precisely, since we know the size of the object and its position as a function of time, then we can predict its image's size and position as a function of time. Knowing that, we wish to optimize our stop/shutter to receive scattering from a propagating pulse, reducing the stop size to yet retain as much of the signal as possible, and timing the shutter to admit the signal only when it is uncontaminated by parasitic scattering.

We want to visualize the size and location, at various points in time, of the image of the outgoing pulse as that pulse moves away from the LIDAR. To express the locations of the object and corresponding image, we use [**Z**] coordinates measured from the **principal planes** of the telescope. In effect, this treats the instrument as a simple lens having

effective focal length $\mathbf{f_{eff}}$. Since the image position $\mathbf{Z_i}$ is then determined by the object position $\mathbf{Z_o}$ as in the relation,

$$Z_i = \frac{Z_o f_{eff}}{Z_o - f_{eff}}$$

the trajectory of the outbound pulse maps into a trajectory of the image, inbound toward the focal plane. If the outgoing pulse is a cylinder of fixed radius, then the trajectory of the inward bound image is a cone with vertex at the focus, like that depicted in [Fig.16]. If the pulse is of short duration, it is a thin, cylindrical section; and if we consider a pattern of these pulse positions having *constant distance spacing* (equivalent to constant separations in time), then the pattern of corresponding image positions, measured from the focus, forms a harmonic sequence converging to that focus. More specifically, if we define "normalized" position coordinates

$$Z_i' = \frac{Z_i}{f_{eff}}$$

$$Z_o' = \frac{Z_o}{f_{eff}}$$

in terms of which we rewrite the above relation,

$$Z_i' = \frac{Z_o'}{Z_o' - 1}$$

then we can rearrange this to solve for the image distance from the focus:

$$Z_i' - 1 = \frac{1}{Z_o' - 1}$$

If we now set the object distances $\mathbf{Z_o}$ to the equi-spaced sequencence $[\mathbf{Z_o}]_\mathbf{n} = \mathbf{n}\Delta\mathbf{z}$, choosing $\Delta\mathbf{z}=\mathbf{f_{eff}}$ so that

$$[Z_o']_n = n$$

the corresponding image sequence is

$$[Z_i' - 1]_n = \frac{1}{n - 1}$$

As **n** increases, this sequence becomes harmonic.

In the figure, each cross section of the cone depicts the planar image of this elemental pulse at one of the given, sequential time increments. Notice that the equal distances in object movement map into *unequal* distances in image movement. The image position converges to the focus as the object distance goes progressively to infinity, while the image sizes decrease continually toward zero. For a pulse of finite duration, the thick, cylindrical section maps into a frustrum of this cone, bounded by two of these image planes, one corresponding to the leading and the other the trailing edge of the outgoing pulse. If the pulse cylinder maintains a constant length, its image frustrum compresses in length as the it moves toward the focus. The opening angle γ of this image trajectory cone is related to the object size $\mathbf{D_o}$ and the effective focal length $\mathbf{f_{eff}}$ of the telescope approximately by

$$\gamma = \frac{D_o}{f_{eff}}$$

Note that we frequently express the aperture of light-gathering, optical instruments as the product $(\mathbf{f_{eff}}\bullet\gamma)$ in factored form. Our telescope is an "f/18" instrument, so our $\gamma = 1/18$.

But [Fig.16] is not the complete picture. In particular, it does *not* show the trajectories of individual scattered light rays which the telescope mirrors cause to converge to form each image point. The scattered rays from *each* object point go into a divergent cone that is reshaped by the telescope mirrors into a cone of rays that converge to a vertex at *single* image point. At positions other than the image, however, these rays are spread throughout their cone. The cones from neighboring object points, going to and coming from their respective image points, necessarily converge. [Fig.17] attempts to show this situation in longitudinal cross sections of several cones. It illustrates how each image point is actually formed; and also why the image is that region where the received light beam is narrowest, as we asserted above. Especially note that, of the three light cones shown, we intend that those on the top and the bottom are from the extreme lateral edges of the pulse volume. For this reason, we assert that they form the lateral extent of the image, here indicated by labelling their inter-vertex separation in the image as the image size $\mathbf{D_i}$. The opening angle α of this image cone is related to the telescope aperture size $\mathbf{D_{tel}}$ and its effective focal length $\mathbf{f_{eff}}$ approximately by

$$\alpha = \frac{D_{tel}}{f_{eff}}$$

For our system, since $\mathbf{D_{tel}} = 10\mathbf{D_o}$, then $\alpha = 10\gamma$ and divergence in the vicinity of our image plane is dominated by telescope aperture divergence. Taken together, these diagrams furnish all the qualitative information that you need to know in order to understand light control issues in the receiver.

Returning now to the question of optimal stop location and shutter action, consider that a fixed stop of a given size will always cutoff rays preferentially for images *not* in its plane. An example of an optimal stop for a *single* image would be one positioned at the image, that was exactly the image size. This would "just include" all the light rays in that image; but would, of course, cutoff some rays from most *other* images. We seek a stop that is optimized for a whole range of images; specifically for images of those pulses that have progressed at least a certain, minimal distance $[\mathbf{Z_o}]_{\mathbf{min}}$ from the LIDAR. What you see in [Fig.16] is that the segment of image trajectory that is associated with the semi-infinite path segment for a pulse, is can be truncated quite close to the primary focus provided that $[\mathbf{Z_o}]_{\mathbf{min}}$ is "sufficiently" large. Thus a stop placed at or near the primary focus and has a diameter equal to the image for the $[\mathbf{Z_o}]_{\mathbf{min}}$ object, is "optimized" for all images on that semi-infinite path. The timing requirement for a shutter at this stop then becomes that the moment at which the shutter comes fully open, $\mathbf{t_{open}} = \mathbf{T_{open}} + \tau_{\mathbf{open}}$, must be no greater than the propagation time $\mathbf{t_{open}} = [\mathbf{Z_o}]_{\mathbf{min}} / \mathbf{c}$.

We now calculate some values of relevance to our own development LIDAR system, to see how these considerations apply. For our instrument, the *effective focal length* $\mathbf{f_{eff}} = 18$m. The length of our pulse volume is about $\Delta\mathbf{Z_{pulse}} = 200$m. After the emergent pulse has travelled a distance of just one of its own lengths, it is already *ten times the focal length* away from the telescope. Thus, the majority of pulse images from this point, $[\mathbf{Z_o}]_{\mathbf{min}} = 200$m, on are very near the primary focus. The location for the optimal field stop is obviously at, or near, this primary focus.

The "object size" for this scattered light is nominally $\mathbf{D_o} = 10$cm, the diameter of the cylindrical source beam (neglecting diffraction effects). We can calculate a *largest* image

size that we must accomodate by assuming that, for reliable data, we will only capture power from those images received *after* the trailing edge of the pulse has propagated to a range of $[\mathbf{Z_o}]_{\mathbf{min}} = \mathbf{c}\tau = 200\text{m}$ from the LIDAR. At this point, the pulse object is about ten focal lengths distant, and it is not unseemly in our calculation to use the "infinite object" approximation (i.e. $\mathbf{Z_i} = \mathbf{f_{eff}}$). Then

$$[D_i]_{max} = D_o\left(\frac{f_{eff}}{Z_o}\right) = 10\text{cm}\left(\frac{18\text{m}}{200\text{m}}\right) = 9\text{mm}$$

We interpret this to mean that we will achieve "optimal" screening of the detector, with no sacrifice of signal throughput, if we place a field stop of diameter 9mm at the primary focus of the receiving telescope. It is interesting to note what effect this stop will have on the signal throughput from pulse positions *closer* that 200m. Since the image of the pulse in this range sector is both larger and more distant than the stop position, the stop vignettes the received light beam and the signal throughput goes down, as we have described above. In a simple LIDAR where you hope to measure the absolute strength of the return signal this effect is very compromising. But the in a DIAL system where you need only measure the *ratio* of two return signals, this is not bad. In fact, we have done a theoretical study which points out how such "spatial filtering" can both reduce the dynamic range requirements of the system's detector and reduce the need for a shutter to protect the detector from initial overload.[30]

Many existing LIDAR systems use rotating mechanical shutters to protect the photodetector elements. For photomultiplier tubes some such precaution is essential, for they have a relatively long "optical memory" to input light overloads. However, as we describe in SECTION4.5:DETECTOR below, we are experimenting with photodiodes as photodetectors. We have some evidence that, under appropriate conditions, these are more immume to overload transients. However, we feel obliged to look at shuttering possibilities, provided that the technologies are not too exotic. Of several alternative methods for shuttering, we decided at this time to measure the capabilities of only an electro-mechanical, leaf shutter Newport Model 844. The results of these tests indicate that such a system cannot react fast and reproducibly enough, in synchrony with the LASER pulse trigger, to provide an opening sufficiently fast and reliable to accomplish the shielding objectives.[31]

Another photodetector issue affecting the receiver optics is that of accomodating the tremendous range in return signal intensity which results from $1/R^2$ fall-off with increase in pulse distance. We discuss this problem further in SECTION4.5:DETECTOR below. If the solution is to use multiple detectors, we would have to provide each of these with a separate beam path, sub-dividing the returning beam. Thus, we might have to split the return signal at the receiver optics and direct part of it to a second detector. We currently have not pursued any solutions to the exit optics presented by multiple detector problems.

4.5. Detector

LIDAR systems for many applications use photomultiplier tubes (PMT) as detecting elements.[32] Because our intended application is in the infrared, and because we are intent on exploring new concepts with our developmental system experiments, we decided to test

the possibilities of using silicon photodiodes. These have several advantages: more efficiency, especially in the near infrared region of the spectrum; not so vulnerable to lasting after-effects of input overload as a PMT; more uniform responsivity over the area of the detector as a PMT. This latter pathology inherent in PMT's produces nonlinear output changes with respect to illumination with spots of various sizes and positions on the photocathode face.[33] For a system with constant illumination geometry, this is not problem. But it is a potential problem with our system where the image of the scattering may change throughout the pulse's journey. We have calculated the useful light range for currently available silicon photodiodes, taking into account saturation an noise figures.[34] Our conclusion is that a single, silicon photodiode, provided it is sufficiently small, should be able to accomodate the strongest return signals from just in front to the transmitter while realising adequate signal-to-noise to detect the weakest of the LIDAR returns from atmospheric Rayleigh backscatter at altitude of 15km. We hoped such a detector also would recover quickly from any input overload that might come from parasitic scattering without the intervention of a shutter. As reported above, this hope was short-lived. We now discuss these issues in somewhat more detail.

At best, a geometrical decrease in power (inverse square law) from the (point) scattering volume determines the range of inputs to which our detector must respond. There is additional fall-off from attenuation caused by absorption and scattering. The "best case" estimate for the return signal range is

[Eq.14] $$\text{Dynamic Range} = \frac{\text{Max}}{\text{Min}} = \left(\frac{15\text{km}}{0.2\text{km}}\right)^2 = 75^2 = 6000$$

Here we have used the value $[\mathbf{Z_0}]_{\mathbf{min}} = 200\text{m}$ that we determined, above, is the minimum distance from which we should expect valid data. A more realistic estimate must include attenuation due to scattering, characterized by an *volume total scattering* coefficient $\beta = \beta_m + \beta_p$. This includes the effects of both molecular scattering and particle scattering, and has a range of values depending upon atmospheric conditions. For molecular scattering only from the standard atmosphere, $\beta_m \cong 0.01\text{km}^{-1}$. For clear air, in which small particles do most of the scattering, $\beta \cong 0.2\text{km}^{-1}$.[35] Using the Beer-Lambert Law we can calculate the corresponding attenuation factors.

Pure standard, air at STP $e^{-\beta(2Z)} = e^{-0.01(2)(15)} = e^{-0.3} = 0.7$

Clear air, at STP $e^{-\beta(2Z)} = e^{-0.2(2)(15)} = e^{-6} = 0.002$

Including these factors in equation [14] result in new estimates, each of which is a "worst case" for the operational LIDAR since these factors assume air at sea level density throughout the path.

$$\text{Dynamic Range} = \frac{6000}{0.7} = 8000$$

$$\text{Dynamic Range} = \frac{6000}{0.002} = 2 \times 10^6$$

We should point out that the estimates of return signal power that we made in the introduction to SECTION4: COMPONENT DEVELOPMENT AND TESTING, do *not* reflect the

effects of attenuation that we have calculated here; nor do our estimates for silicon photodiode efficiency.[36] Thus we acknowledged that a simple photodiode detector may not be sufficient. Accordingly, our detector designs include both photomultiplier tubes and avalanche photodiode detectors. For example, if we apply the clear air attenuation factor to the return power estimate from the introduction, at the same time adjusting that result to scattering from 15km here as compared to 10km there

$$[\mathcal{P}_r]_{net} = 7 \text{ nanowatts} \left(\frac{10km}{15km}\right)^2 0.002 \cong 7 \text{ picowatts}$$

This value approaches the detectivity limit of most silicon photodiodes, but perhaps is within the regime of an avalanche photodiode. Also

$$[\mathcal{P}_r]_{net} = 6 \times 10^9 \text{ photons/sec} \left(\frac{10km}{15km}\right)^2 0.002 \cong 5 \times 10^6 \text{ photons/sec}$$

This rate is within the regime of photon counting.

In any satisfactory detector configuration, we have the problem of providing amplifiers of suitably expansive dynamic range; and the signal processing equipment must likewise be sufficiently accomodating. In our designs we include preamplifiers with dynamic ranges to handle these inputs and yet have sufficiently fast response times. Since sufficiently fast digitizers are rarely found with resolutions greater than 10-bits(1024), some sort of signal compression is in order. In our designs we include amplifier configurations which exert signal compression. We also have the electronics equipment needed to process these photocurrents down to the photon-counting regime if necessary.

For the detector/preamp of our LIDAR development system we chose an EG&G Model HFD-1100, which is a hybrid of a $1.5mm^2$ silicon photodiode and an integrated, high frequency preamplifier. This unit has a specified responsitivity of 3.5×10^4 volts/watt and a minimum detectable power of 18nanowatts at $\lambda = 633nm$ when configured, as ours is, with a $R_f = 100K\Omega$ feedback resistor. However, we directly measured this minimum detectable power using the output of a HeNe ($\lambda = 633nm$) LASER attenuated with neutral density filters and found it to be about one nanowatt.[37] This hybrid amplifier has a gain/bandwidth product of 1.2Ghz. [Fig.18] is a schematic diagram for our complete receiver, consisting of the hybrid detector/preamp and a driver amplifier.

We achieved additional amplification by transporting the signal through one meter of 50Ω coaxial cable to an amplifier in our CAMAC crate. Here the amplified signal was ported to a crate companion, our highspeed digitizer. These crate elements were all made by LeCroy. Specifically

Model 8013a CAMAC bin
Model 6102 Amplifier
Model TR8837f Transient Recorder
Model 8901a GPIB Interface.

In related work, we constructed a photodetector test and calibration facility as part of this project. This is a light-proof box, large enough to accomodate a PMT with its associated housing. The detector mount inside is driven by three, electro-mechanical translating stages, giving x-y-z degrees of freedom. It has light-proof electrical feedthroughs to

supply power and control signals for the translators, power for a light source, and operating voltage to the detector, while extracting signal from the detector.[38]

We attempted to address several issues of the detection system electronics. One of these is the diagnosis of the parasitic oscillations which we describe in SECTION5: SYSTEMS INTEGRATION AND TESTING. Another is our signal processing equipment listed above. This system is capable of eight-bit digitization at rates of up to 30 megasamples per second. It has 8 kilobytes of buffer memory. These sampling capabilities are more than adequate to accomodate the data rates and the data sample sizes associated with the $\tau = 1\mu s$ pulses of our source LASER. However, the eight-bit precision is not nearly enough accomodate the range of return signal strengths, as we described above. Accordingly, we procured, but did not test, a fast logarithmic preamplifier to achieve signal compression, as a solution to accomodate the vast range of the return signals. We designed a system for gain-switching amplifiers in the system. This system multiplexes a pair of detectors as well as switching the signal path to include none, one, or two amplifiers.[39] We have acquired sufficient amplifiers and the requisite signal switching capability to switch the detection system gains in a manner programmed to accomodate the diminishing signal strength as the returns arrive from increasing distances. All of these analog and digital electronics are modular and reside in either the system NIM bin or in the system CAMAC crate.

4.6. Computer

Our experiments use several different computers at various levels of instrument control, data acquisition, and data analysis. Although these may operate alone in the simpler component development experiments, they operate simultaneously in the integrated system. Having discussed the component computers' roles in the individual component subsections, we here present only the system aspects of the integrated ensemble. [Fig.19] is a block diagram of the integrated system's microcomputer configuration.

We use several microcomputers operating simultaneously. The LASER INSTRUMENT CONTROL COMPUTER is a PC which operates the LASER cavity tuning elements, triggers the LASER driver, and records both the output pulse energy and the output wavelength spectrum. Within this system, another, single board microprocessor (M6801) operates the spectrometer detector array and controls the timing of the trigger pulse to the LASER power supply. This SPECTROMETER/FIRING CONTROL COMPUTER passes the spectral data to the LASER INSTRUMENT CONTROL COMPUTER. The DATA ACQUISITION COMPUTER is a PC/XT which supervises the acquisition of the return signal data from the receiver. These data are read from the Transient Recorder's memory and archived an disk for subsequent transport to the various analyses computers. To realize computing speed, we use a PC/AT as the PRIMARY ANALYSIS COMPUTER for initial data analysis. This microcomputer has a modem connection for transmitting data files to a VAX-11/780 which is the COMPREHENSIVE ARCHIVING AND ANALYSIS COMPUTER.

This distributed data processing approach stands in contrast to using a single, master mini-computer (c.f. [Fig.4]) to control the entire instrument system, which was envisioned in the AMOS LIDAR proposal.[40] In the latter, you must configure the master computer to multi-task in order to service all the system component needs in real time.

This is a complicated programming task. In the former, our approach, you must tolerate data storage in several different places, and possibly in different formats. You must also sometimes substitute manpower for computer power in that several people may have to operate the several computers in the course of an experiment. This penalty for the distributed approach is ameliorated for us because in the development environment, in contrast to the operational environment, each participating individual can personnaly monitor their component sub-system for unexpected and inadequate behavior. This greatly reduces the chance of spending long periods gathering experimental data which are invalid because of deficiencies in one component. The distributed approach also has the merit of flexibility. For example, may use the individual sub-systems in a stand-alone manner (c.f. the detector array from the spectrometer used in etalon studies).

4.6.1. LASER Instrument Control

This PC computer controls the firing sequence and manages the LASER output diagnostics for wavelength and energy. We have developed two programs for our experimental purposes. One of these is the CAVITY TUNING PROGRAM by means of which we set the orientational alignment of the total reflector end mirror. This program also records the LASER pulse energy. We originally developed it for and used it extensively with our tuning and dye degradation experiments. The PC controls the cavity reflector by means of electro-mechanical micrometers which we describe elsewhere. This control is mediated by a dedicated electronics (NRC Model 815) connected to this computer by means of an IEEE-488 instrument bus, and to the micrometers by means of a specialized umbilical for passing command and encoder feedback information. The PC program executes its pulse energy readout function by constantly listening to its serial input port for a transmission which signals that energy data are available. This happens whenever the energy meter is triggered by an arriving LASER pulse. The connection between the PC and the energy meter is through a slightly modified RS232c serial interface. [Fig.19] shows all these connections.

The other program is the PHOTODETECTOR ARRAY PROGRAM. This PC program works solely with a single board computer (SBC), the SPECTROMETER/FIRING CONTROL COMPUTER. Its function is to send firing commands to a program running on the SBC, and to interrogate the SBC's memory for spectral data when they are available. This program communicates with the SBC, in ASCII code, through a standard RS232c serial interface.

4.6.2. Spectrometer/firing Control

The SPECTROMETER/FIRING CONTROL **SBC** is based upon the Motorola M6801 microprocessor.[41] This microprocessor is specified to run with a 1 MHz clock; but we use a 4 Mz clock with the recommendation of the manufacturer because we need additional speed. This microprocessor is actually a complete microcomputer in itself, containing a small cache RAM, a TTL serial interface, and a ROM with a monitor program (**LilBug**). This monitor mediates SBC communication with the LASER Instrument Control host (PC) via the SBC's serial interface. We have placed 4K of additional RAM and an 8-bit analog to digital convertor onboard the SBC. This memory is a data storage buffer, and contains a program that we have written to control event timing in response to commands transmitted from the host PC. In proper sequence, this

SBC program properly initializes the photodiode array, transmits the LASER trigger, and clocks out the photodiode data with sufficient promptness to insure their validity. We intend the SBC specifically to control a Reticon RL1024G Photodiode Array through a companion Sampling Circuit board.[42] This RC100B motherboard connects to the array through a Reticon RC106 amplifier/clock board. The RC100B interfaces to the SBC by means of digital lines through a ribbon cable. The SBC has a TTL logic line connecting to the LASER driver through 50Ω coaxial cable. [Fig. 19] shows all these connections.

4.6.3. Data Acquisition

To control the data acquisition and archiving of successive pulses, we have a PC/XT interfaced to the CAMAC crate which contains the digitizer. This TRANSIENT RECORDER SYSTEM is capable of eight-bit digitization at rates of up to 30 megasamples per second. It has 8 kilobytes of buffer memory. The interface between these two is an IEEE-488 instrument bus. The software we use on the PC to log and archive data onto its hard disk is LeCroy's **Catalyst Plus**.

The Transient Recorder continually digitizes and stores data in a ring buffer. It responds to a trigger pulse from the LASER power supply by freezing this ring buffer after a number of post-trigger data have been recorded, corresponding to a certain percentage of the buffer memory. In this way a selected number of "pre-trigger" data are retained. This methodology permits us to accomodate a variety of intersystem delays without having to implement an elaborate sequence of timing pulses to control the various LIDAR components. The **Catalyst Plus** permits us embed the pre-trigger value, as well as CAMAC amplifier gain, digitization rate, and display and storage formats in a "setup file", which in effect programs the data acquisition process.

Catalyst Plus has a facility for viewing the data in various ways, which permits us to do some real time, preliminary analysis and use that information to direct the course our experiments. It permits us to store data, which we do onto 20Mb hard disk which is our primary archive. It also has a facility for re-coding binary data files into ASCII format, which we can then write to floppy disk for transport to other computers for input to other analysis programs.

4.6.4. Comprehensive Archiving and Analysis

We use a variety of computers to process the archived data from all of our developmental experiments. To permit this, we developed methods to pass data from **Catalyst** to **Asystant** (a scientific analysis program) within the PC environment, and from the PC environment to that of the VAX/11-780. For the former transfer, we chose to use **Catalyst** to reformat its binary data files into ASCII format. Although the latter format is much less efficient than a binary format, such files can be unambiguously read by any good analysis program. Because this data transfer stays within the PC environment, we can use floppy disks at transer media. For the latter transfer, we also start with the ASCII file format, but go one step further. Because this data transfer requires that we cross computer operating system environments, we use a telecommunications program (**Kermit**) to achieve this transfer via a high-speed modem. Compatible versions of **Kermit** run both on the PC/AT and the VAX computers, and can supervise such transfers on their respective machines.

We use a PC/AT as the *Primary Analysis* computer for systematic data analysis. This computer has a modem connection for transmitting data files to a VAX-11/780 which is the *Comprehensive Archiving and Analysis* computer. We chose the PC/AT to realize computing speed, while retaining the same operating system and hardware environment of the data acquisition system. **Asystant** is a commercial program that has a wide range of analysis features. With it we may edit datafiles, perform Fourier analysis, average data, filter data, transform and "correct" data, and so forth. It also enables us to produce publication quality graphs having our own choice of format.

We have not used the VAX extensively, except to prove the transfer process. Clearly, however, we will require its extensive computing and storage power once the data quantities become very large.

5. Systems Integration and Testing

We report here the preliminary field test results for the period up to 23 Nov 1987. For these tests, we constructed the LIDAR development system, which we have previously outlined above, at the AOTF. We conducted several experiments using this system, acquiring data over a number of running nights. We were primarily concerned with examining the signal returns for their strengths; but also were able to deduce detector performance capabilities and defects, and to assess the system optical alignment sensitivity. These results, in turn, contribute to the recommendations of the project (c.f. Section 6.0). Here we briefly list the components that were in the integrated system, and describe how we conducted the system tests.

Our development system contained a single source dye LASER and exit optics sufficient to transport the output beam through the beam expander and out of the coelostat. For some tests we also included the beam sampling optics and operated the pulse energy measurement system. On these occasions we also optimized the cavity tuning during course of the experiments. We did not use the spectrometer to obtain an output wavelength measurement, as we always operated the source LASER in the broad-band mode, without any tuning elements. In the outdoor tests we used the coelostat and the telescope for both transmission and reception. In all experiments we used only a single photodiode detector; although we changed our design from a preamplifier integrated with the detector, into a discrete preamplifier connected as a separate op-amp circuit to a bare detector. We used various mountings for the detector, including one which permits us to scan the detector laterally in a carefully controlled manner between individual LIDAR shots. We used increasingly complete and sophisticated light shielding around the photodetector to screen out stray light reflected from the walls around the room; but we did not attempt to baffle or otherwise restrict the FOV of the photodetector, in the manner of a field stop that we have described previously (c.f.SECTION 4.4: RECEIVER OPTICS).

We made our runs entirely at night. Although we did some preliminary tests to investigate the possibility of running during the daytime as well, the results are inconclusive at this point. The primary problem with daytime operation over this range appears to be turbulence-induced scintillation. For each running period, we adjust the beam expander for collimation by a technique which we developed and we describe elsewhere. We bore-sight the beam expander during the day before the night-time running period. For this operation we use the HeNe LASER arranged as for dye LASERcavity alignment, a telescope with cross hairs, a beamsplitter, and a retro-reflector. The procedure is one we developed, and we describe it in SECTION 4.3.3: BORESIGHT/COLLIMATION DIAGNOSTIC.

The test range is a path of length 1.6km leading from the coelostat atop the AOTF building, across an open field along the Verona test range, to white-painted, wooden test shed. In early experiments we opened the AOTF-facing doors of this shed and mounted a 2" retroreflector inside, within the beam area. In later experiments after we discovered the amplifier oscillations from the light-saturated detector, we simply closed the shed doors and used the diffuse reflection therefrom to furnish the terminal light pulse back to the detector.

We acquire data of the atmospheric returns at a bandwidth of 10 Mhz and an intersample time of 30 nanoseconds, using 8-bit digitizing precision. A typical test run protocol starts with preliminary shots to establish that the system is reasonably aligned. Next we conduct test a number of test shots which we record to establish baseline statistics. Then we vary the parameter we are trying to test, and make a number of data shots. At intermediate points we might return to the baseline parameters and make a reference check consisting of one or two shots. Because we do not want to rely upon signal averaging at this point, which might obscure significant data inhomogeneities, we save all data. Thus we must be parsimonious in our data acquisition. **Catalyst** stores the full 8-kB buffer for each shot, and we soon would otherwise have more data than we could handle.

For the LIDAR receiver using a single silicon photodiode coupled to a fast, low-noise, integrated circuit preamplifier, we observed returns from LASER shots over this course of 1.6km. We recorded these results in 8-bit digitized form. [Fig.20] shows a record of our first successful observation of a LIDAR return from our 1.6km test range at the AOTF. Though they lack dynamic range sufficient to reliably show the atmospheric Rayleigh backscatter along the path, they do reveal some information with important implications for detector design.

The colinear arrangement of the transmitter and receiver allows high intensity light scattered by the exit optics to blind the detector. We felt that the fast response of the photodiode would allow it to return from saturation to a linear region of operation after the trailing edge of the output pulse cleared the exit optics. We found that this was true; however the electronics used to amplify the photodiode output tend to oscillate when the photodiode is saturated, which oscillation continues into the regime where we expect valid signal returns. This oscillation is genuinely associated with the optical power into the photodetector, and is not an artifact of RF from the flashlamps or spark gaps penetrating inadequate electromagnetic shielding on the detector electronics. We confirmed this assertion by placing a retro-reflector at the 1.6km range terminus, in place of a diffuse reflector normally there. The parasitic oscillation recurred for the retro-reflection return which strongly saturated the detector, but not for the weaker diffuse return which did not.

6. Conclusions and Recommendations

From the experiments described above we have learned the following:

- •We have a rudimentary LIDAR system in which we observe Rayleigh backscatter from air over a range of 1.6km and diffuse scatter from a terminal, hard target.
- •We have operational beam diagnostic subsystems for monitoring the wavelength with resolution ($\Delta\lambda/\lambda = 10^{-4}$) and the intensity profile of the LASER output, although these have not been installed and tested in the integrated LIDAR development system.
- •Using the Candela CL-1200 flashlamp/dye cells, our operating output power is easily 200mJ/pulse at 500 nm. from Coumarin 504 broadband with a pulse length of about 1 microsecond.
- •Photo-degradation of the LASER dyes from the flashlamp radiation has a significant effect on the LASER output, at least for the Coumarin 504.
- •The single photodiode detector scheme has some promise for replacing the conventional PMTs in the LIDAR detection system.
- •The commercial data acquisition software **Catalyst** is adequate, if a bit cumbersome, for LIDAR data collection.

Based upon these results, we recommend the following:

- •The least-complete part of this study is the electronics of the detection system. We have obtained amplifier parts and multiplexor switching which ought to be configured and tested for the requisite capability.
- •For system performance adequate for DIAL water vapor profiling along the LIDAR line-of-sight the system must have a high-resolution wavemeter with potential for exercising realtime LASER wavelength control through a "closed-loop" control arrangement. An optogalvanic detector with feedback is probably suitable to control the "fine" etalon in a triple-etalon tuning of the dye LASER cavity.[43,44]
- •Some kind of shutter system to protect the detector from radiation scattered out of the outgoing pulses by the exit-optics structures will likely be necessary. An electro-optic shutter might be suitable here. We have obtained a crystal "Q-switch" which ought to be tried.
- •Some additional system testing, especially after installation of the completed detection sub-system, ought to be done either at the AOTF and/or the AMOS facility on Maui, depending on the outcomes of the project experiments.

7. Acknowledgements

The work described here was done under the auspices of the RADC Laboratory Director, Dr. Fredric Diamond, under the terms of a grant from his Laboratory Director's Fund. We gratefully acknowledge his support and encouragement for this work.

1. E.R Murray, R.D. Hake,Jr., J.E. van der Laan, and J.C. Hawley, *Appl.Phys.Lett.* **28**, 542 (1976).
2. E.V. Browell, T.D. Wilkerson, and T.J. McIlrath, *Appl.Optics* **18**, 3474 (1979).
3. E.V. Browell, A.F. Carter, and T.D. Wilkerson, *Optical Engineering* **20**, 84 (1981).
4. C. Cahen, J.-L. Lesne, J.N. Michelin, and J. Lefr`ere, "Simultaneous Measurement of Water Vapor Mixing Ratio and Aerosol Content Using a DIAL Technique at 0.72 mm: Comparison with Radiosounding and Lidar Measurements at 1.06 mm", *Proc. XI Int Laser Radar Conf.*, Madison, WI (June 1982).
5. N.J. Chonacky, LDF Proposal: "Advanced Remote Sensing Applications to Strategic Surveillance", RADC/OCSP (Oct. 1984), Work Unit Plan, Section IV.
6. T.D. Wilkerson and G.K. Schwemmer, "LIDAR Utilization for Determining Atmospheric Transmission at AMOS/MOTIF", Report to Avco Everett Research Laboratory for Contract No. F30604-80-C-0323 (August 1982).
7. Raymond Measures, *Laser Remote Sensing: Fundamentals and Applications*, J.W. Wiley & Sons, New York (1984).
[Fig.1] Block diagram of a basic LIDAR system.
[Fig.2] Block/schematic diagram of a monostaticLIDAR system.
[Fig.3] Simple transmission model for DIAL.
[Fig.4] Block diagram for a LIDAR system proposed for AMOS (Figure 3 from Wilkerson's report II, pg.30).
8. T.D. Wilkerson, G.K. Schwemmer, and L.J. Cotnoir, "LIDAR for Improved Determinations of Atmospheric Transmission at AMOS/MOTIF", Report to Avco Everett Research Laboratory for Contract No. F30604-80-C-0323 (November 1983), pg.30.
[Fig.5] Schematic diagram of a development LASER system.
[Fig.6] Block/schematic diagram of a development LIDAR system.
9. N.J. Chonacky, LDF Proposal: "Advanced Remote Sensing Applications to Strategic Surveillance", *Op.Cit.*, Schedule for Activities,pg.1.
10. *Ibid*,pgs.2-4.
11. Raymond Measures, *Laser Remote Sensing: Fundamentals and Applications*, J.W. Wiley & Sons, New York(1984).
12. Earl J. McCartney, *Optics of the Atmosphere: Scattering by Molecules and Particles*, John Wiley and Sons (1976).
13. Raymond Measures, *Laser Remote Sensing: Fundamentals and Applications*, *Op.Cit.* Pg.43, Table 2.3.
14. R.T.H. Collis and P.B. Russell, "LIDAR Measurement of Particles and Gases by Elastic Backscattering and Differential Absorption," *Laser Monitoring of the Atmosphere* (E.D. Hinckely, ed.) Springer-Verlag (1976), pg.89.
15. Earl J. McCartney (1976), *Op.Cit*, pg.83, Table 2.6.
[Fig.7] H_20 absorption spectrum obtained with a 300m absorption cell and a ruby-pumped dye LASER.
16. E.V. Browell, T.D. Wilkerson, and T.J. McIlrath, *Appl.Optics* **18**, *Op.Cit.*, pg.3478, Fig.5.
17. T.D. Wilkerson and G.K. Schwemmer, "LIDAR Utilization for Determining Atmospheric Transmission at AMOS/MOTIF", *Op.Cit.*,pg.10.
[Fig.8] Quadraxial Dye LASER tube details.
[Fig.9] Developemt LASER system resonator details.

18. *Laser Dyes Catalog*, Exciton Corporation, Dayton OH (1987), pg.3.
19. N. Chonacky, "Photodegradation of Coumarin 504 in a Flashlamp-pumped Dye LASER", RADC Technical Report, in preparation.
20. N. Chonacky, "Photo-degradation Studies of Coumarin 504 in a Flashlamp-pumped Dye LASER", Bulletin of the American Physical Society, **32**, No.3, March 1987, pg.567.
21. RADC In-house Research Quarterly Achievement Award (March 1988).
22. A.E. Siegman, *LASERS*, University Science Books, Mill Valley CA (1986), p419 & p.524.
23. J. Theimer, "Etalon Measurements", RADC Technical Memo, in preparation.
24. *Operations Manual*, Scientech Model 38-0101 Volume Absorbing Disc Calorimeter, Scientech Corporation, Boulder CO (March1983).
[Fig.10] Deployment details of the SciTech Model 38-0101 Volume Absorbing Disc Calorimeter: solid drawing is position for LASER development work; dashed drawing, with beam sampler inserted, is position for LIDAR development work.
25. M.B. Morris and T.J. McIlrath, "A Portable, High-Resolution, LASER Monochromator/Interferometer with Multichannel Electronic Readout", Institute for Physical Science and Technology, University of Maryland - College Park, Technical Report BN921, August 1979.
26. D. Green, "Microprocesser-mediated Operation of a Reticon Photodiode Array for Pulsed-LASER Measurements", RADC/OCSP Technical Memo (1 Oct 1984), unpublished.
27. J. Theimer, "Two-wavelength Calibration of a Grating Spectrometer Having a Digital Output Generated by a Microprocessor", unpublished technical memo, RADC/OCSP (1987).
28. J. Theimer, "Etalon Measurements", RADC Technical Memo, in preparation.
[Fig.11] Schematic detail of the exit, optical train of our development LIDAR system.
[Fig.12] Structural Details of the Main Telescope at the AOTF.
29. R.H. Zacharias, E.M. Nelson, and A.R. Phillips, "Technical Proposal for a 40-inch Aperture Cassegrain Telescope", Project F(1)-1222-047-014-2044, Fecker Systems Division of Owens-Illinois, Pittsburgh (27 April 1944).
[Fig.13] Optical Schematic Layout of the AOTF Main Telescope.
[Fig.12] Structural Details of the Main Telescope at the AOTF.
[Fig.14] Boresight/collimation Diagnostic System Schematic Diagram.
[Fig.15] Shutter Timing Sequence: Aperture versus time.
[Fig.16] Image position/size trajectories in the vicinity of the primary focus of the receiving telescope.
[Fig.16] Image position/size trajectories in the vicinity of the primary focus of the receiving telescope.
[Fig.17] Construction of an image showing only the contribution from three, principal cones of light, and these shown only in cross section.
[Fig.16] Image position/size trajectories in the vicinity of the primary focus of the receiving telescope.
30. D. Norton, "Spatial Filter Proposal: An alternative to shuttering", RADC/OCSP Technical Note (27 February 1987), unpublished.
31. C. Vernold, "Measurements of the Opening Characteristics of an Electro-mechanical Shutter", RADC/OCSP Technical Note (August 1986), unpublished.

32. Raymond Measures, *Laser Remote Sensing: Fundamentals and Applications, Op.Cit.* Pgs.217ff.
33. P. Cook, "Non-uniformity in the Responsivity of Photomultiplier Photocathodes", RADC/OCSP Technical Note, unpublished
34. P. Cook, "Characteristics of Avalanche Photo-diodes", RADC/OCSP Technical Note (23 January 1987), unpublished.
35. Earl J. McCartney (1976), *Op.Cit.* pg.30.
36. P. Cook, "Characteristics of Avalanche Photo-diodes", RADC/OCSP Technical Note (23 January 1987), unpublished.
37. T. Busch, RADC/OCSP (24 May 1988), private communication.
[Fig.18] Schematic Circuit Diagram of the Development LIDAR Receiver.
38. D. Norton, "Lightproof 'Dark Box' for Light Detector Testing and Calibration", RADC/OCSP Engineering Plans (1987).
39. N. Chonacky, "CAMAC-based Switched Gain LIDAR Amplifer System", RADC/OCSP Technical Memo, unpublished.
[Fig.19] Block Diagram of Distributed Microcomputer System.
40. T.D. Wilkerson, G.K. Schwemmer, and L.J. Cotnoir, "LIDAR for Improved Determinations of Atmospheric Transmission at AMOS/MOTIF", Report to Avco Everett Research Laboratory for Contract No. F30604-80-C-0323 (November 1983), pg.30.
[Fig.19] Block Diagram of Distributed Microcomputer System.
41. D. Ruhberg, "Application Prototype Board for MC6801 MCU", Application Note AN799, Motorola Corporation - Semiconductor Products, Austin TX 78721 (1980).
42. T. Busch, "A M6801 Program for Controlling Synchronous Operation of a Reticon RC100B Sampling Circuit with a Reticon RL1024G Photodiode Array", RADC/OCSP Technical Note (1987), unpublished.
[Fig.19] Block Diagram of Distributed Microcomputer System.
[Fig.20] First Successful Observation of a LIDAR Return: hard target is a shed at 1.6km
43. D.S. King, P.K. Schenck, K.C. Smyth, and J.C. Travis, "Direct Calibration of Laser Wavelength and Bandwidth Using the Optogalvanic Effect in Hollow Cathode Lamps", *Appl. Optics* **16**, 2617 (1977).
44. J.E Lawler, Univ. of Wisconsin, Dept. of Physics (1984), private communication.

List of Figures

Altitude (km)	Temperature (°K)	Pressure (mb)	Density (kg/m^3)
0	288.15	1013.25	1.225
11	216.65	227.00	3.648×10^{-1}
20	216.65	55.29	8.891×10^{-2}
32	228.65	8.89	1.356×10^{-2}
47	270.65	1.16	1.497×10^{-3}
52	270.65	6.22×10^{-1}	8.01×10^{-4}
61	252.65	1.97×10^{-1}	2.703×10^{-4}
79	180.65	1.24×10^{-2}	2.349×10^{-5}
88.74	180.65	2.07×10^{-3}	4.0×10^{-6}

Table 1: Atmospheric Model: U.S. Standard Atmosphere - 1962

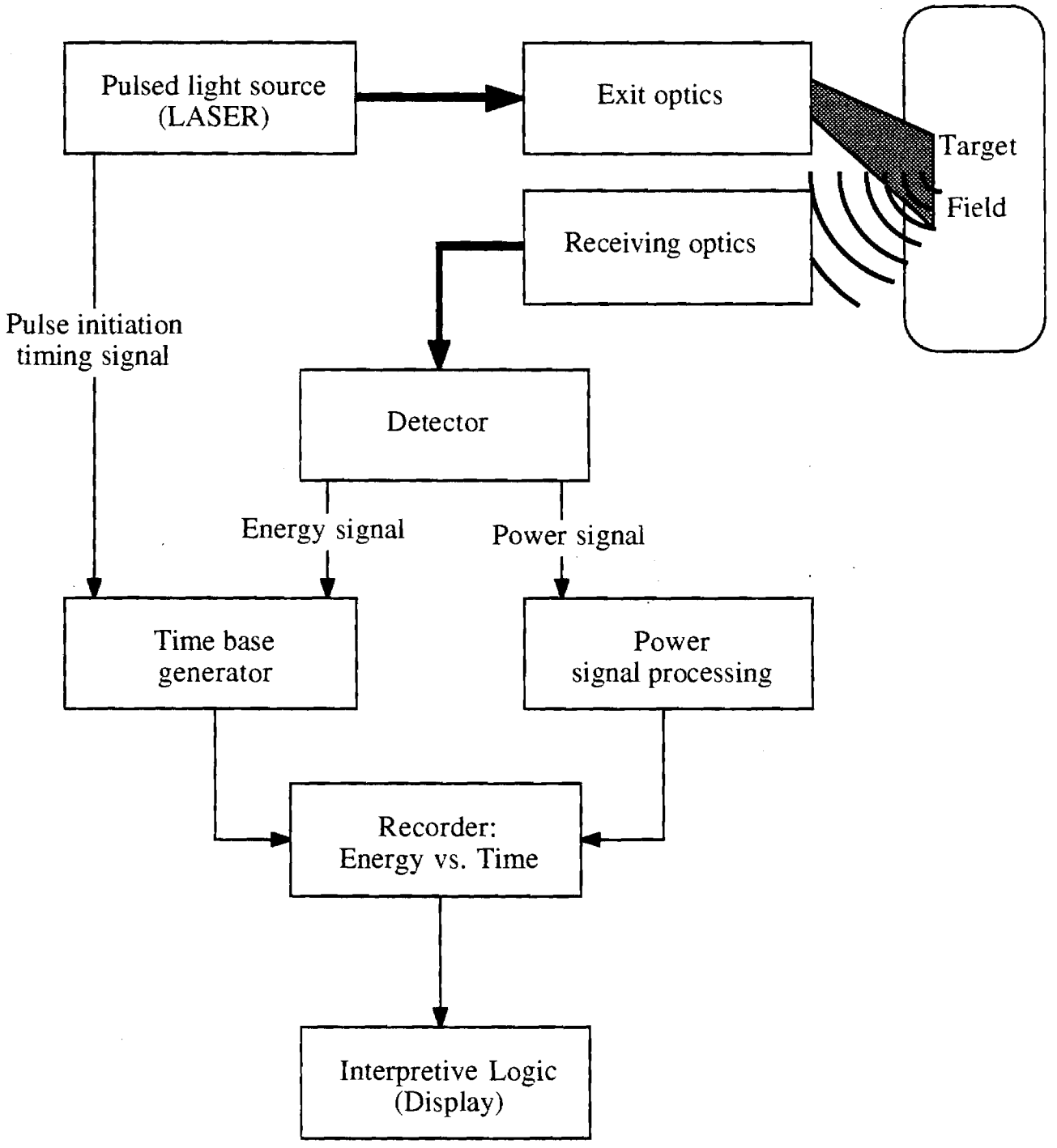

Figure 1: Block functional diagram of basic LIDAR

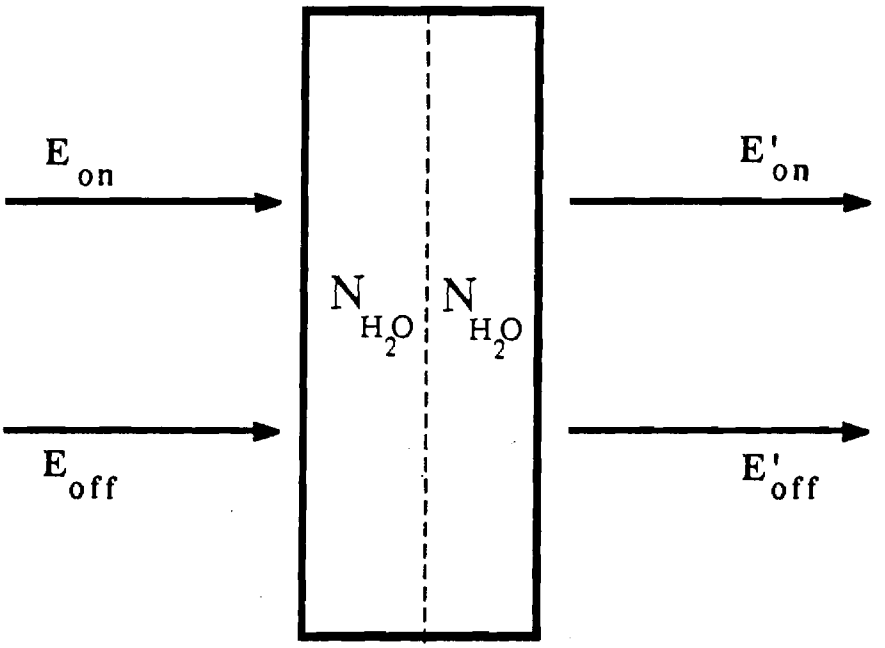

N_{H_2O} = (mole) number of target (water) molecules.

Figure 3: Transmission model for DIAL system.

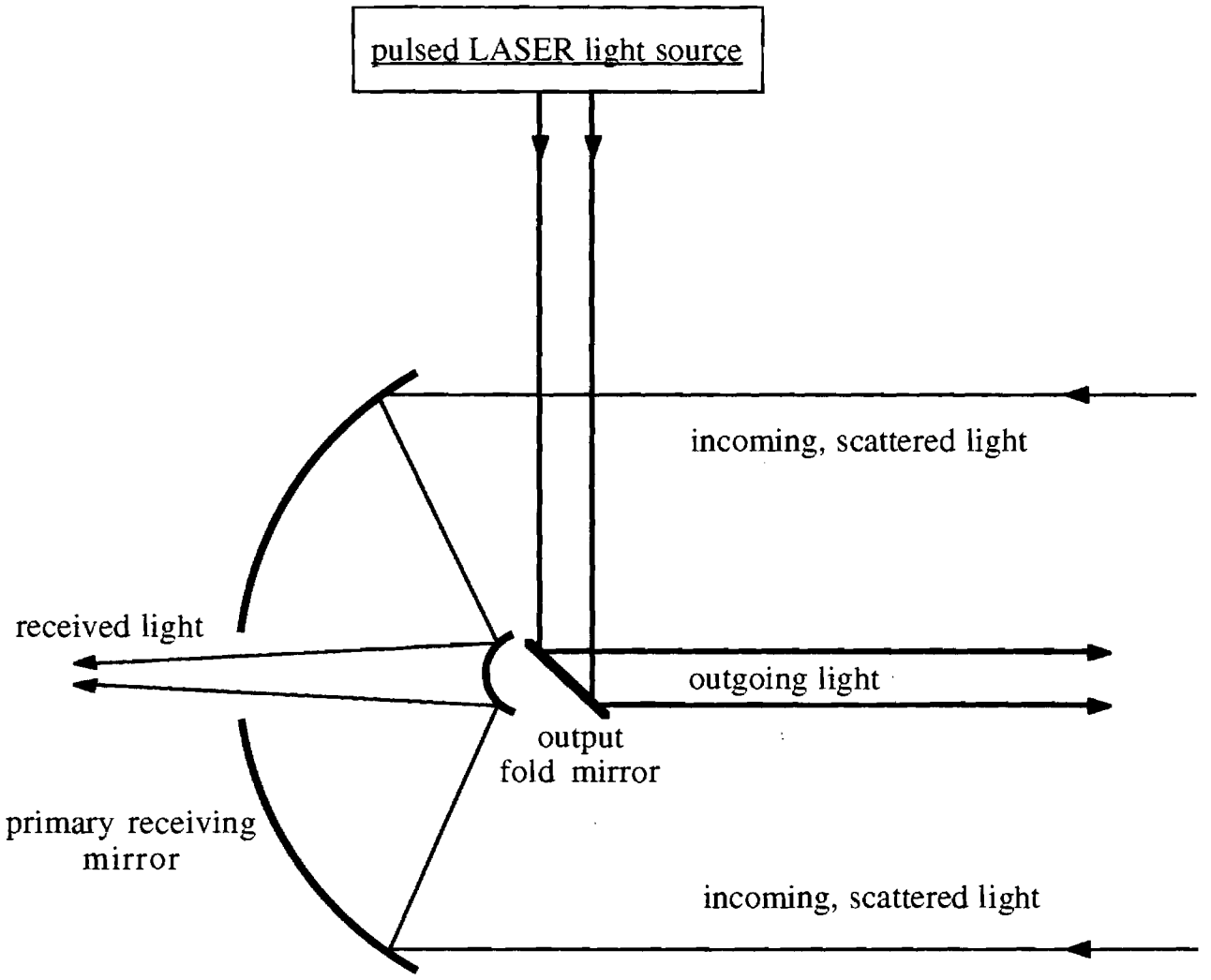

Figure 2: Schematic diagram of monostatic LIDAR

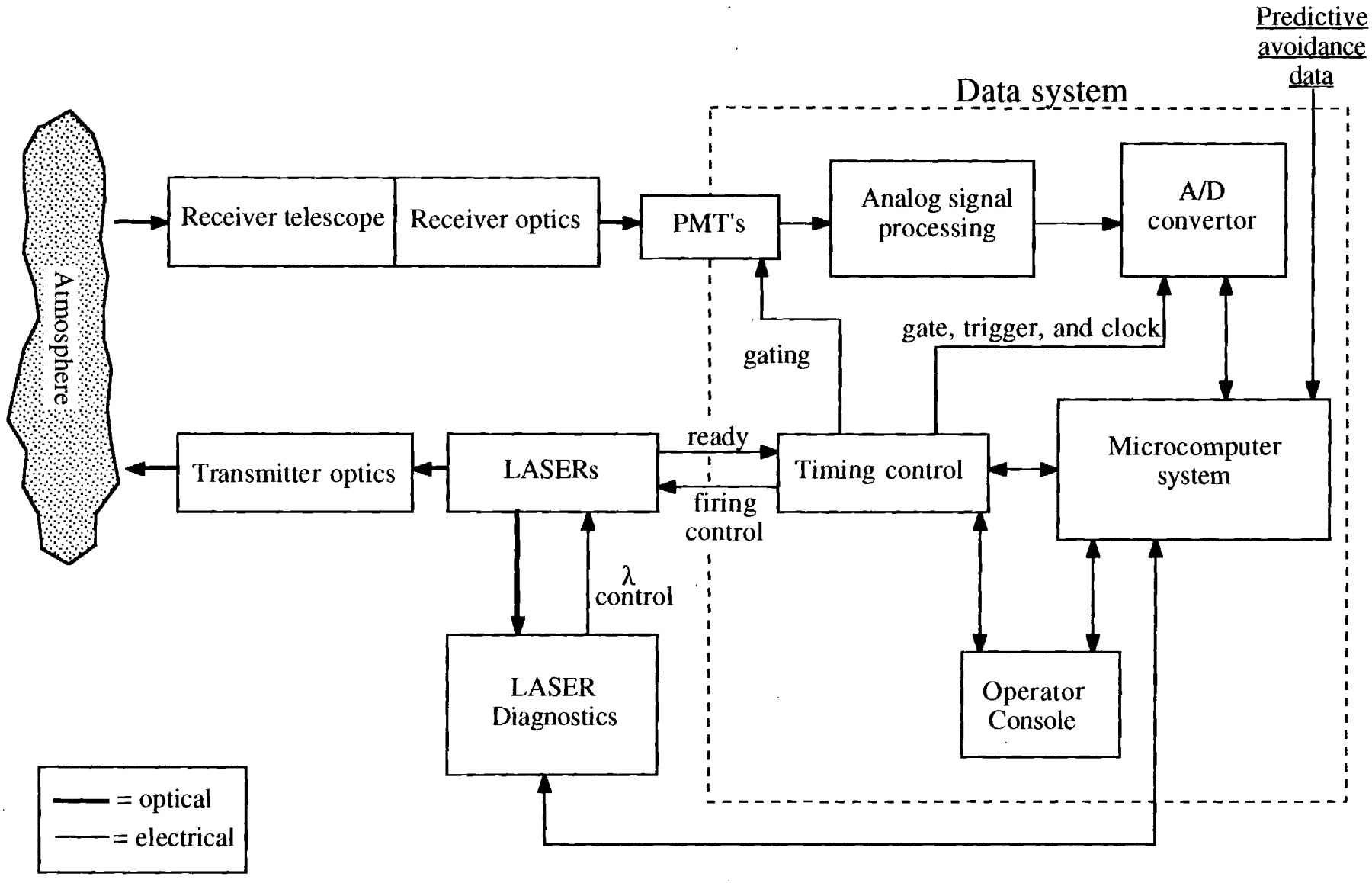

Figure 4: Block diagram of a LIDAR system proposed for AMOS

(from Wilkerson's report II, pg.30.)

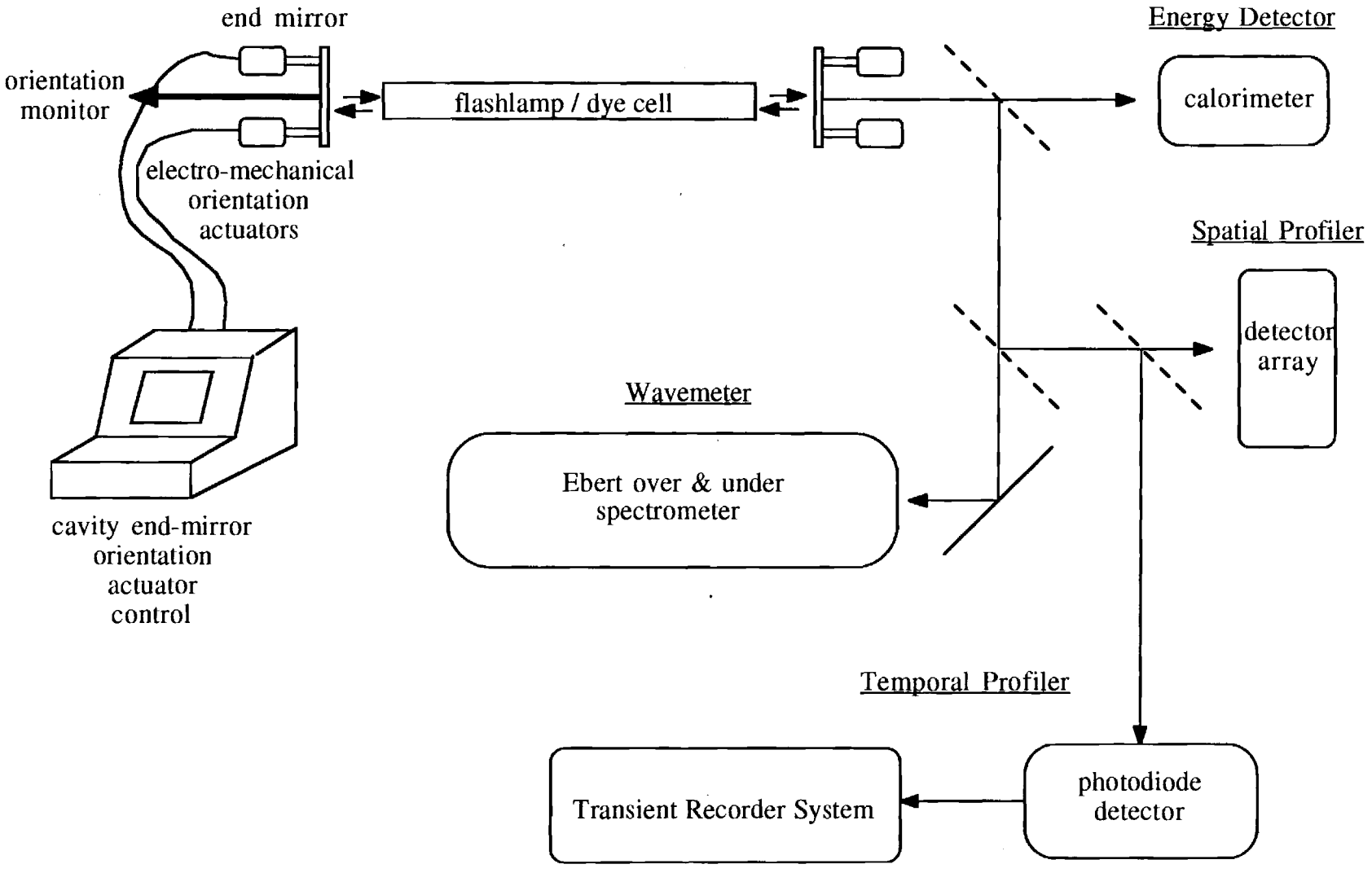

Figure 5: Schematic diagram of a developmental LASER system.

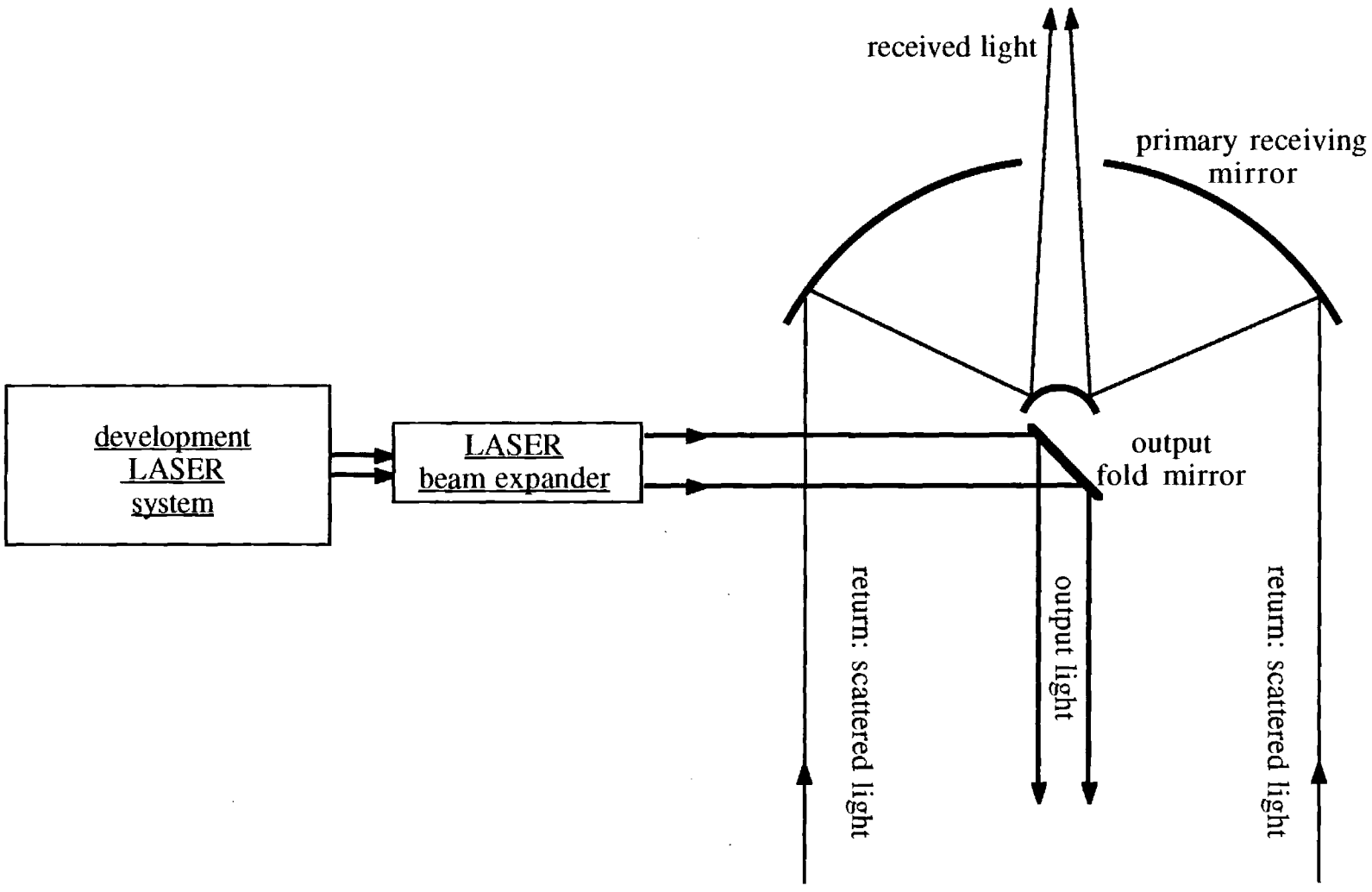

Figure 6: Block/Schematic diagram of a developmental LIDAR system.

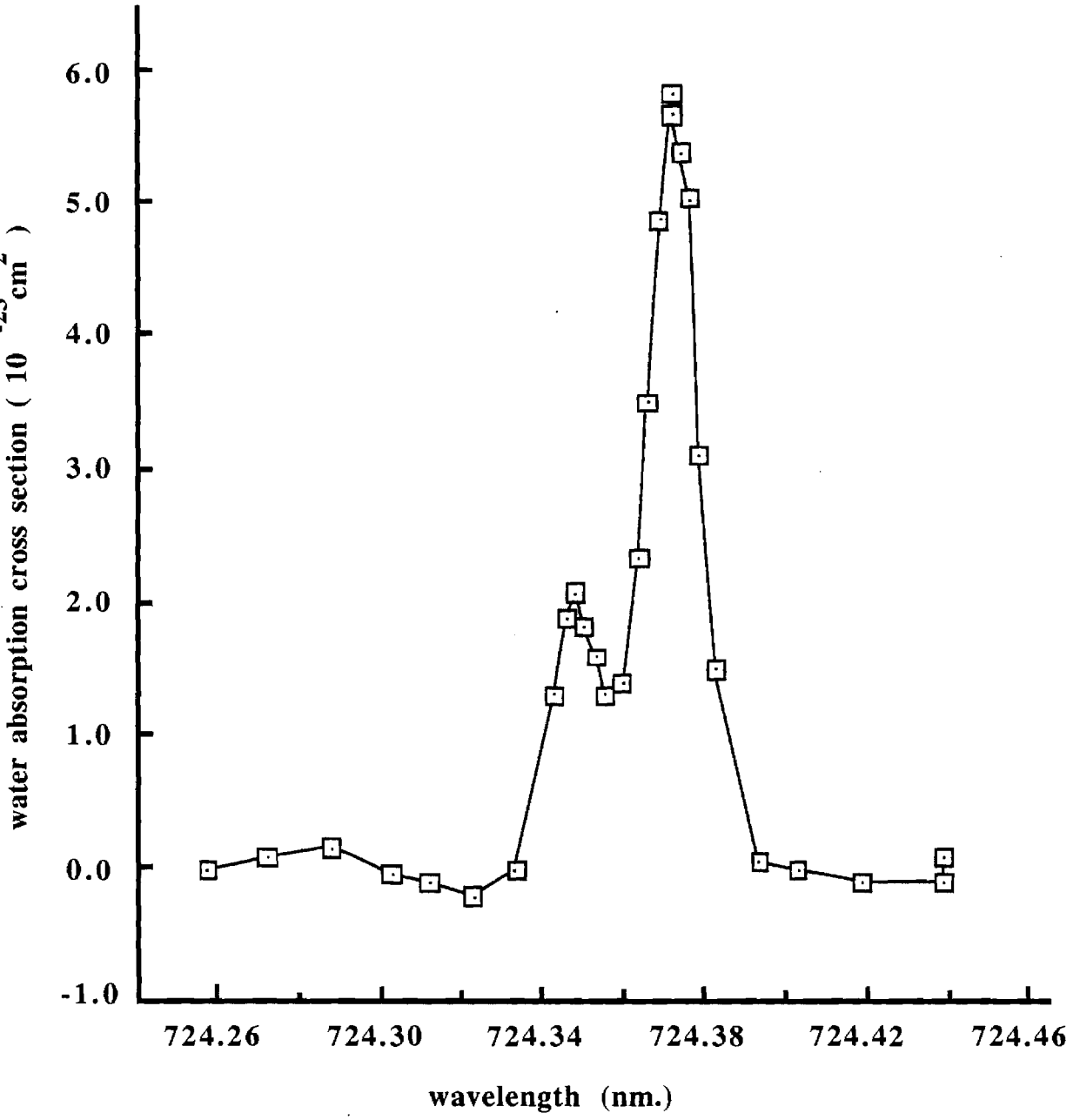

Figure 7: H_2O absorption spectrum from a 300m absorption cell and a ruby-pumped dye laser.
from Browell, Wilkerson, and McIlrath, **Applied Optics** 18, 3478 (1979)

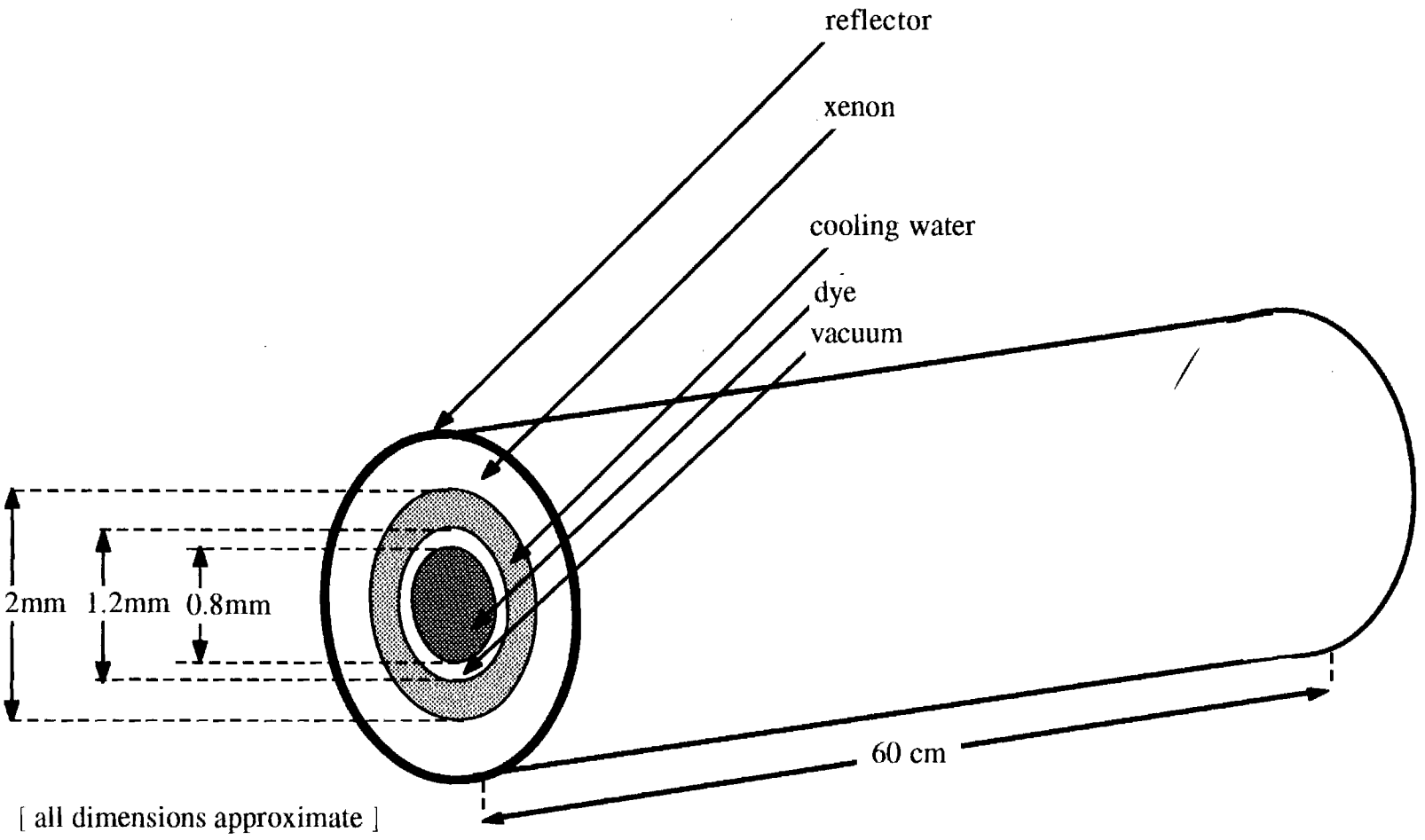

Fig.8: Candela QL-1200 Quadraxial dye LASER tube details.

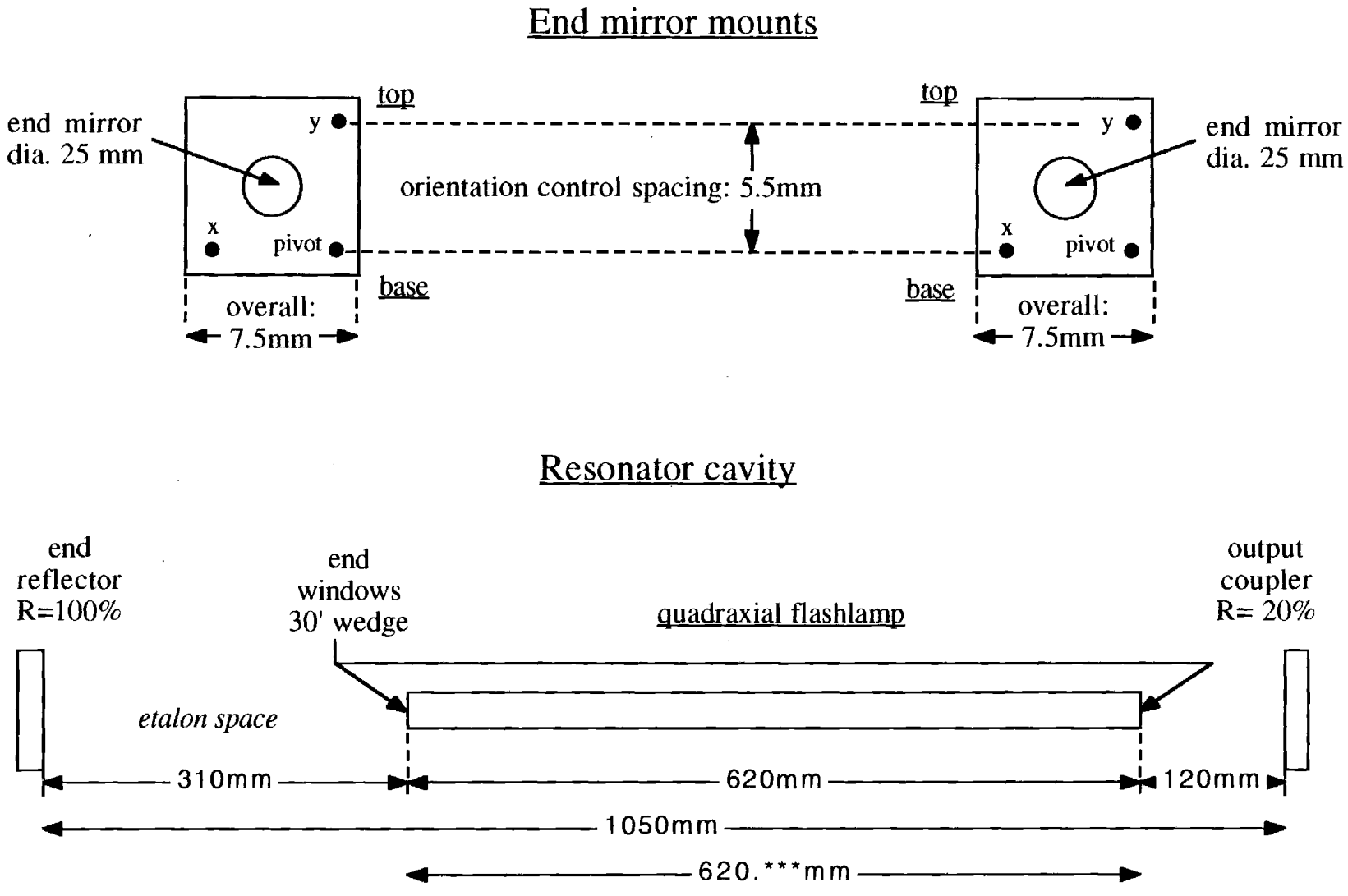

Fig.9: Candela development dye LASER system resonator details.

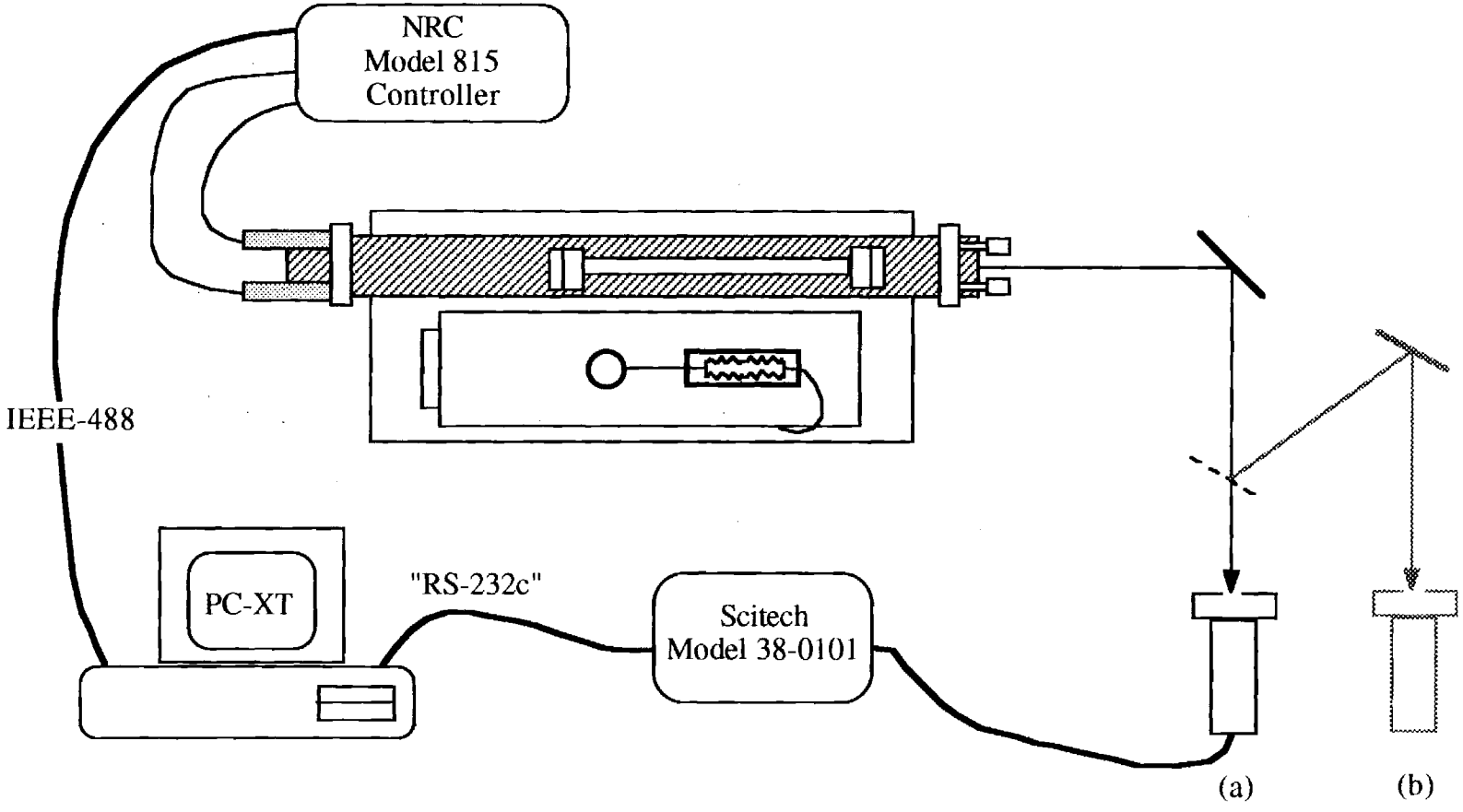

Fig.10: Deployment details of the SciTec Model 38-0101 Volume Absorbing Disc Calorimeter:

a.) solid drawing is position for LASER development work;
b.) dashed drawing, with beam sampler inserted, is position for LIDAR development work.

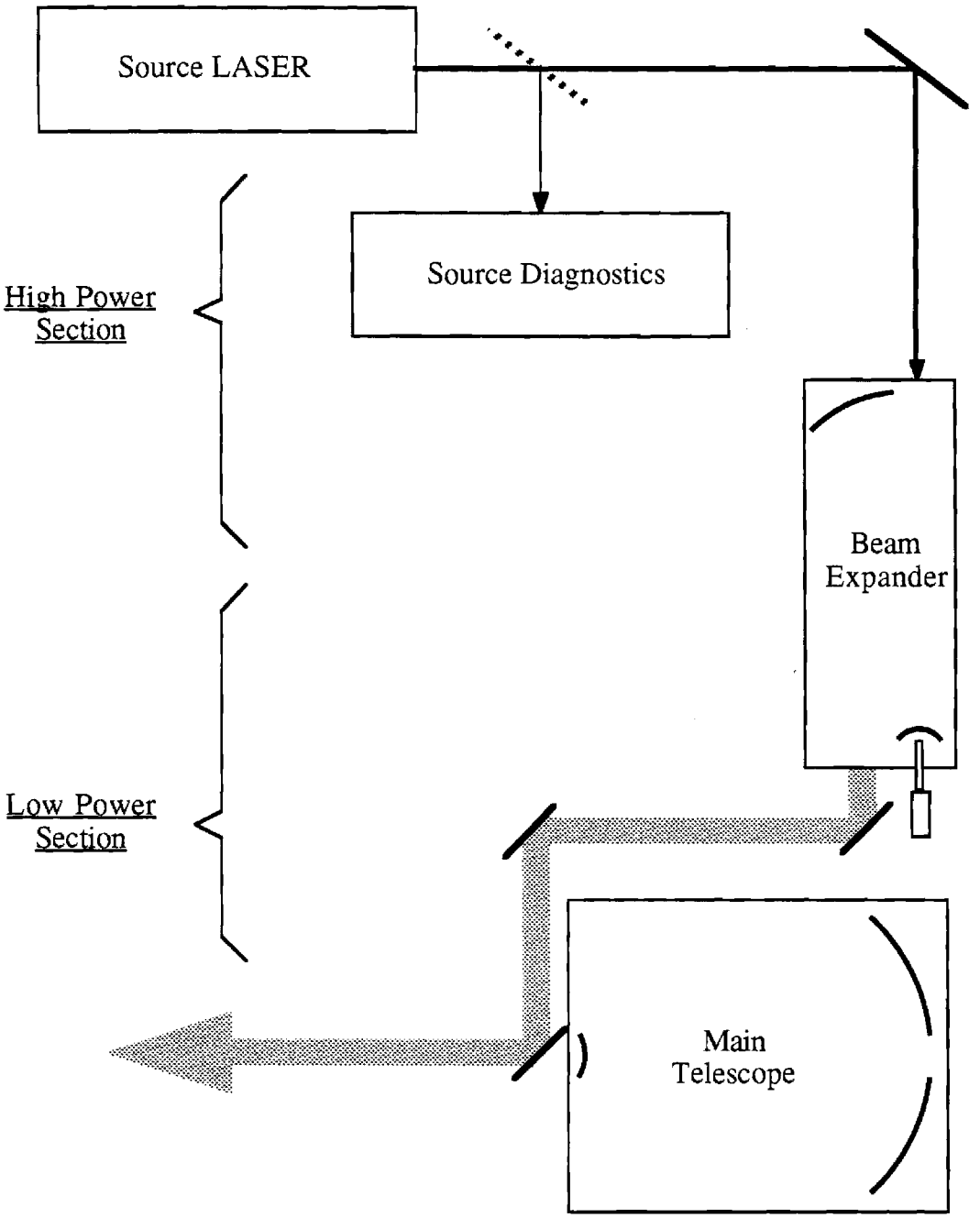

Figure 11: Schematic of the exit optics, development LIDAR system.

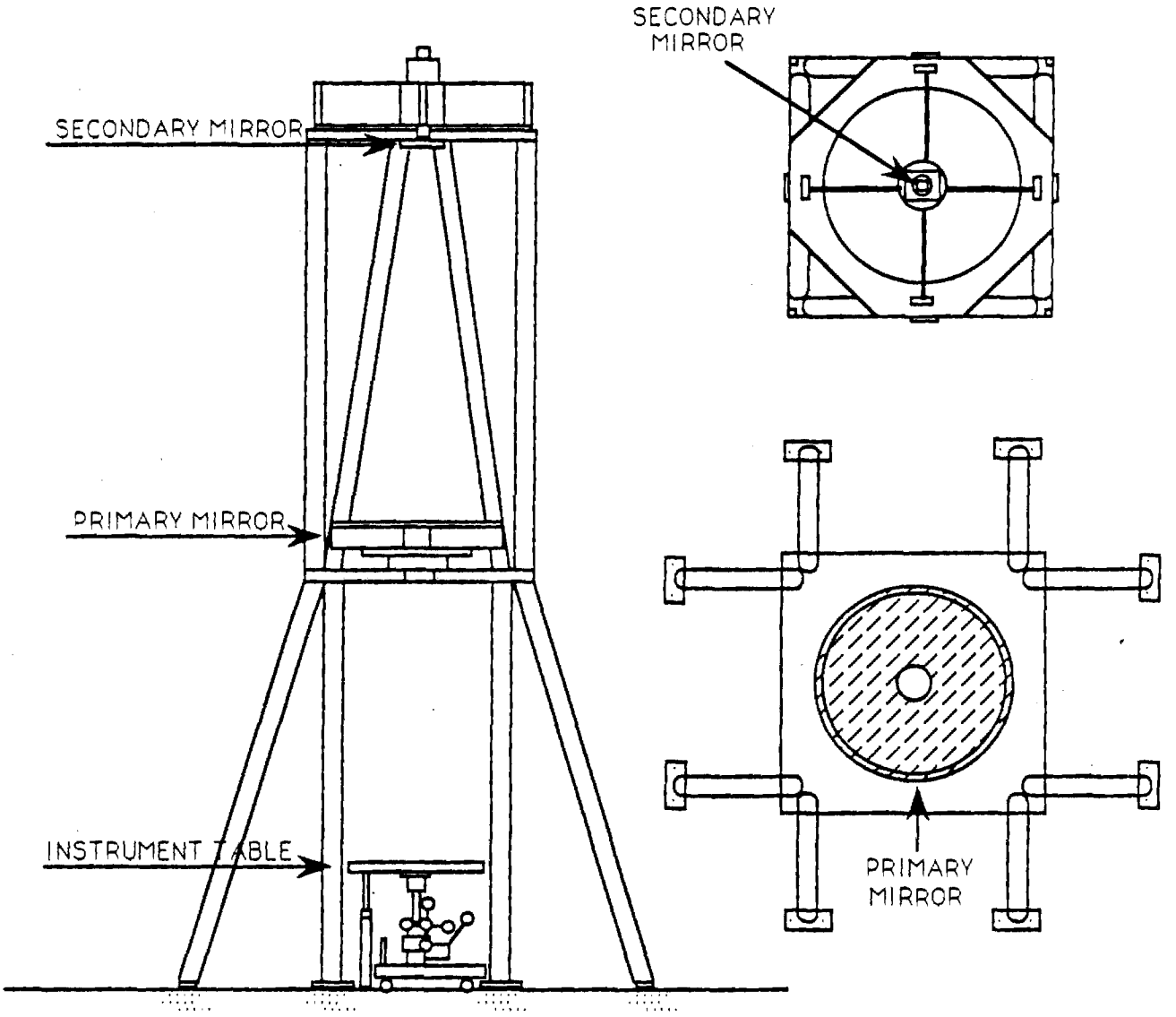

Figure 12: Structural Details of the Main Telescope at the AOTF.

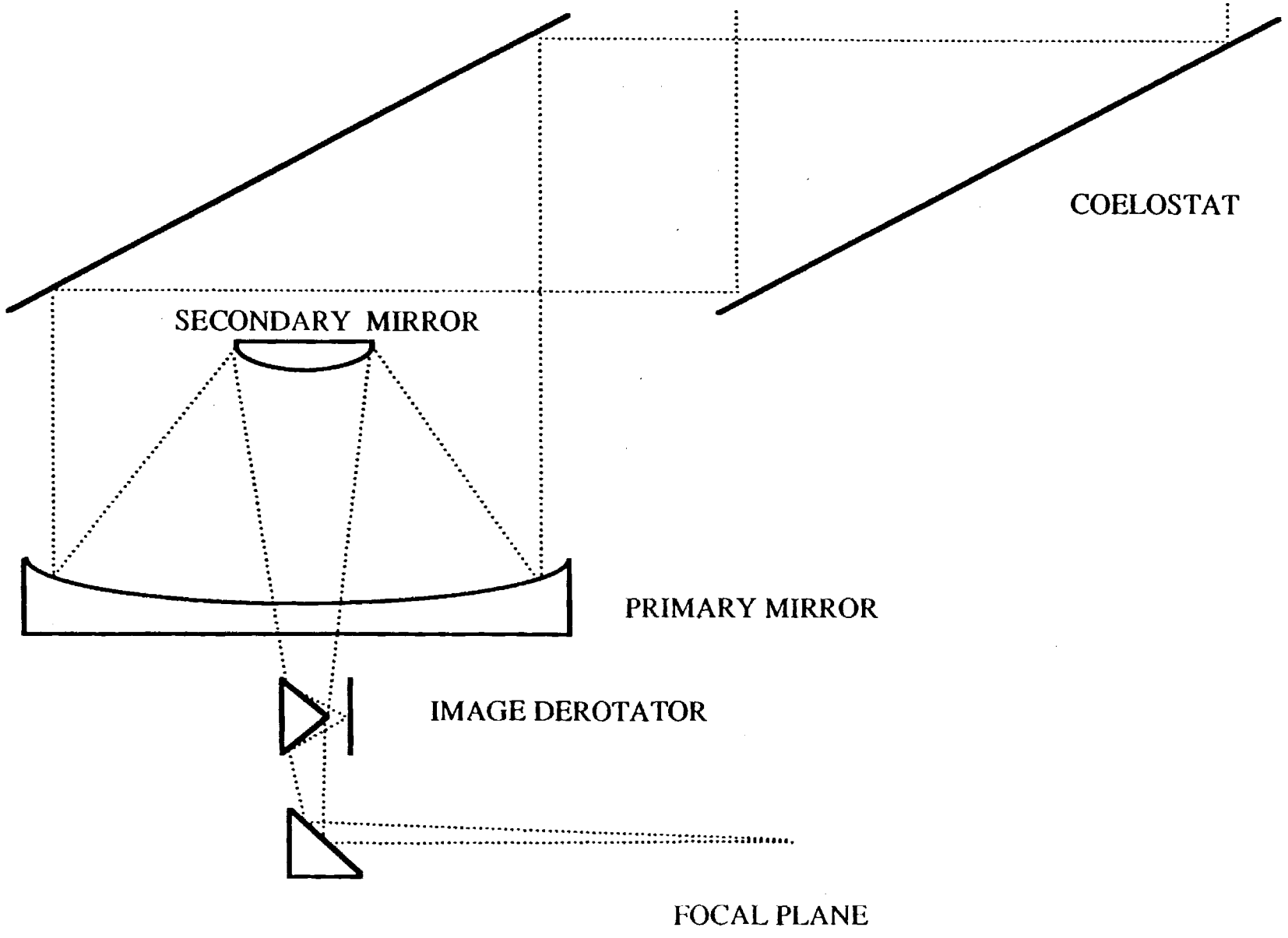

Figure13: Optical Schematic Layout of the AOTF Main Telescope.

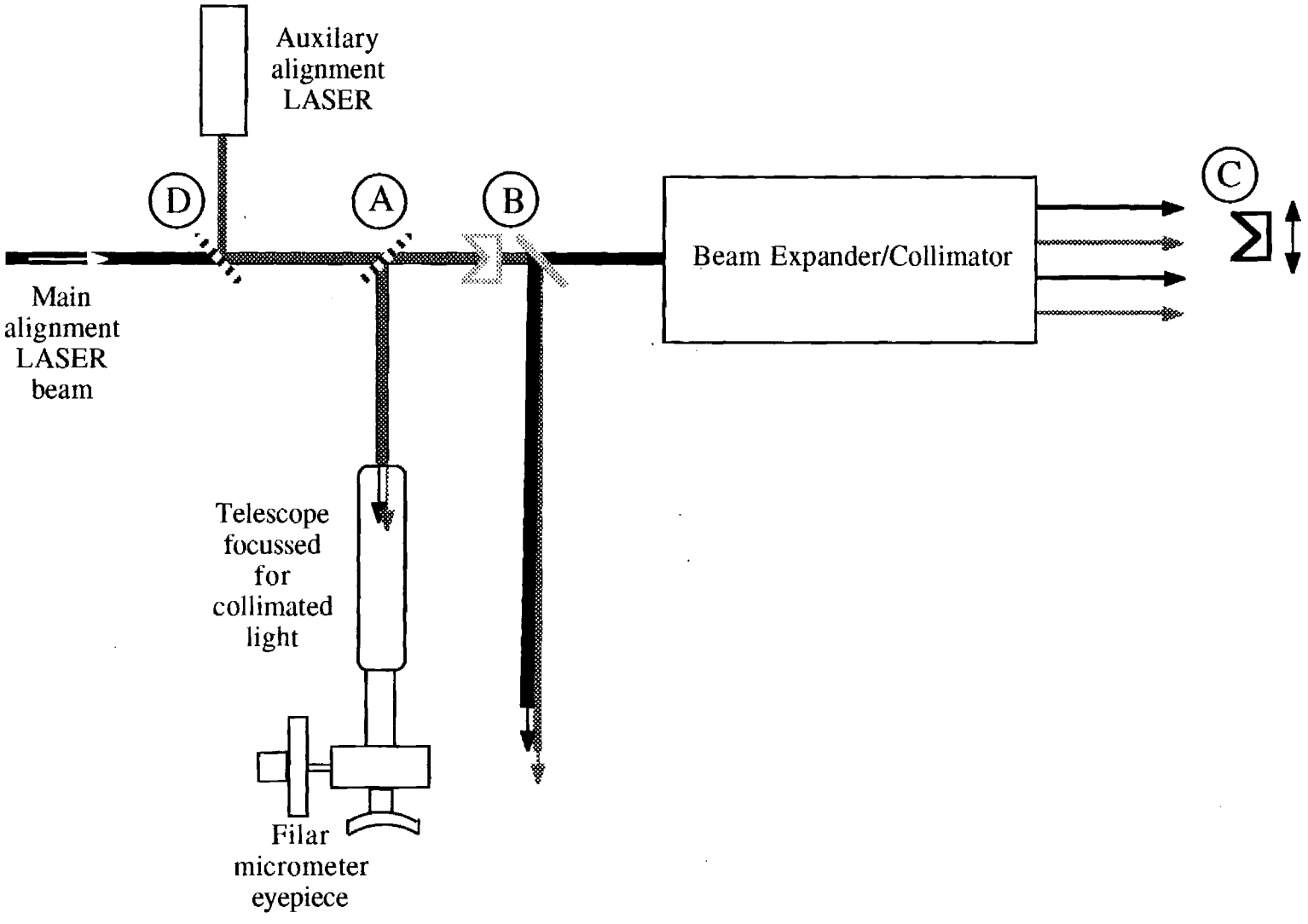

Figure 14: Boresight/collimation Diagnostic System Schematic Diagram.

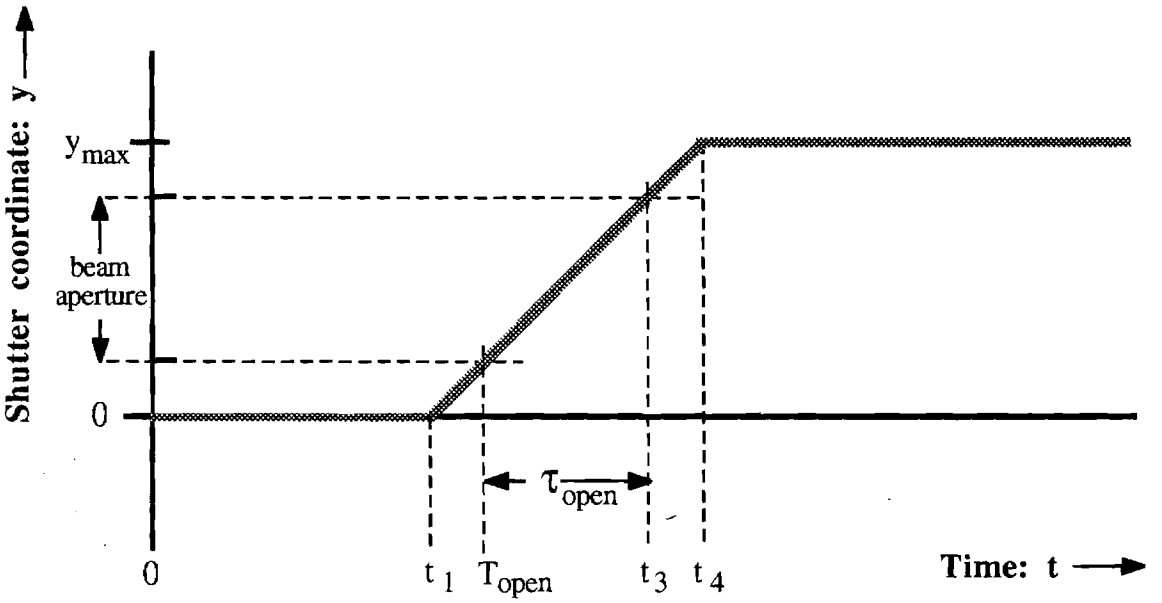

Figure 15: Shutter Timing Sequence: aperture versus time.

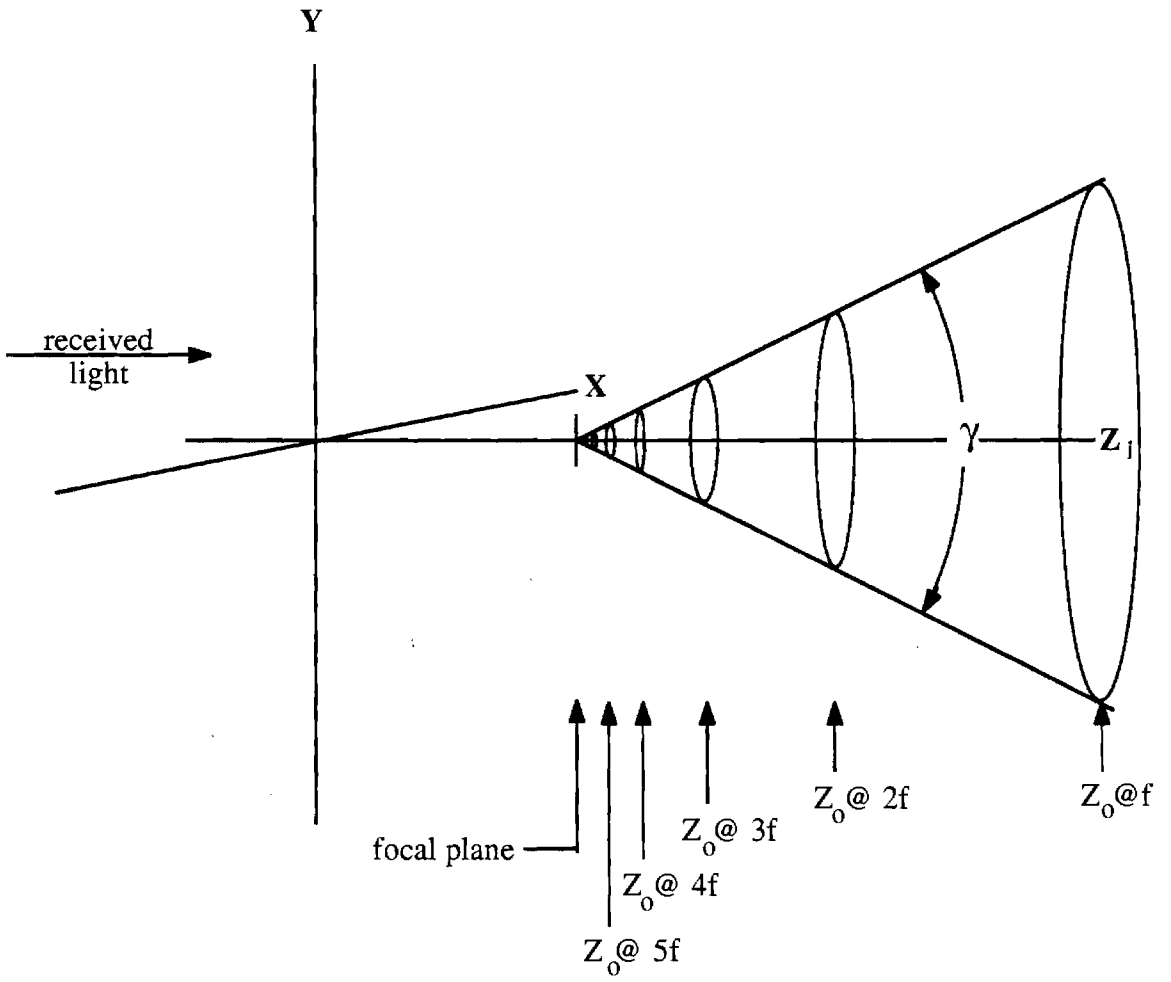

Figure 16: Image position/size trajectories in the vicinity of the primary focus of the receiving telescope.

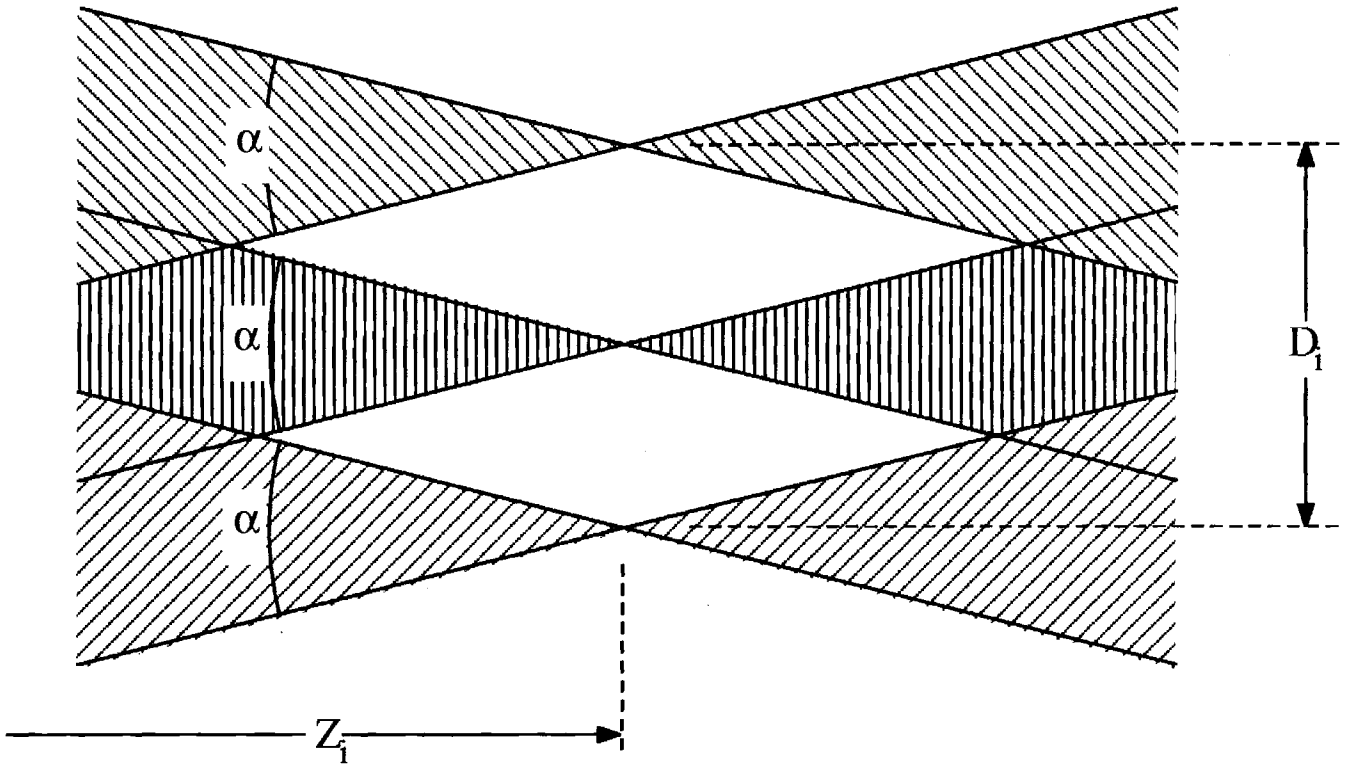

Figure 17: Synthesis of an image depicting only the contributions from three cones of light, here shown in cross section.

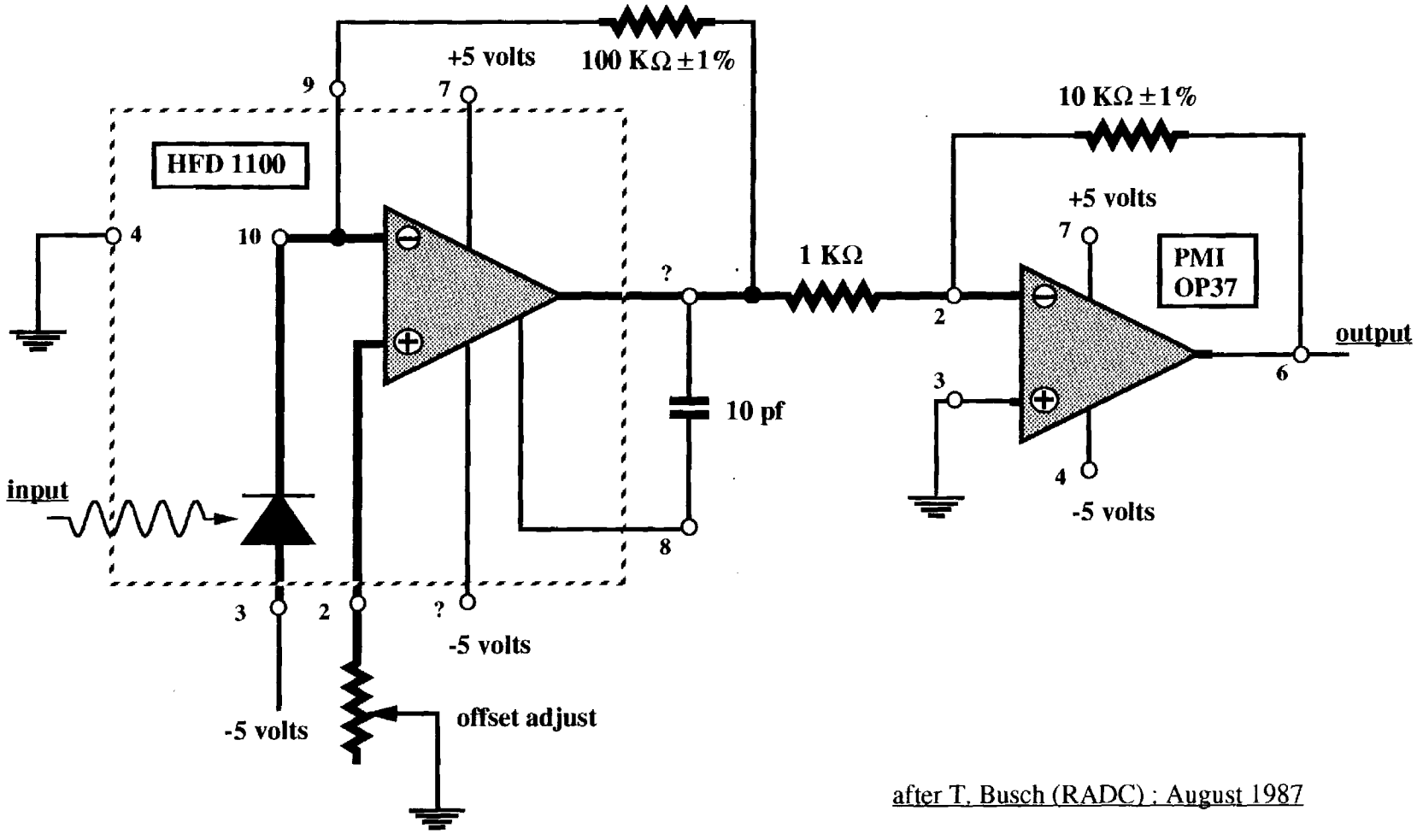

Figure 18: Schematic Circuit Diagram of the Development LIDAR Receiver.

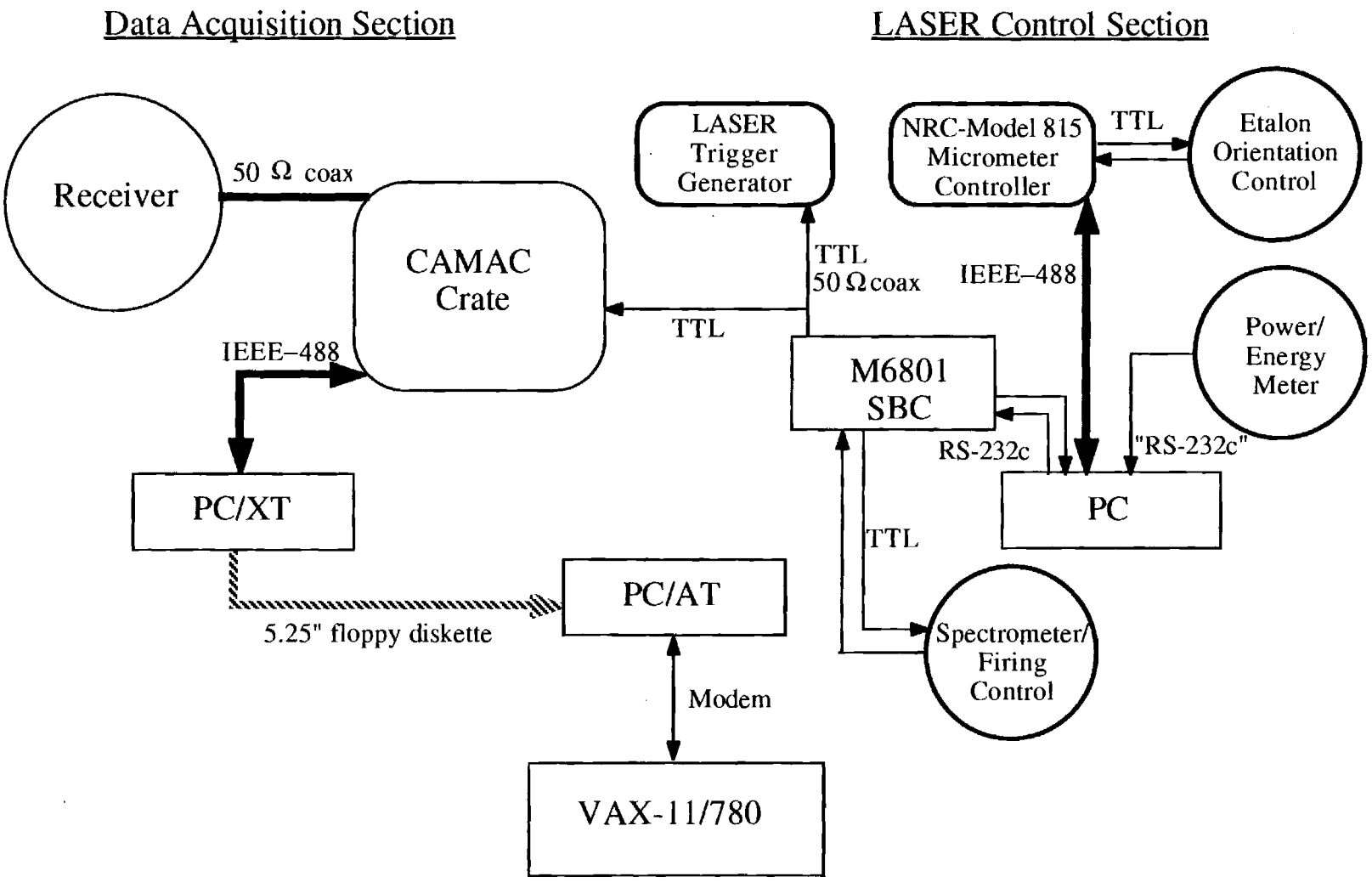

Figure 19: Block Diagram of Distributed Microcomputer System.

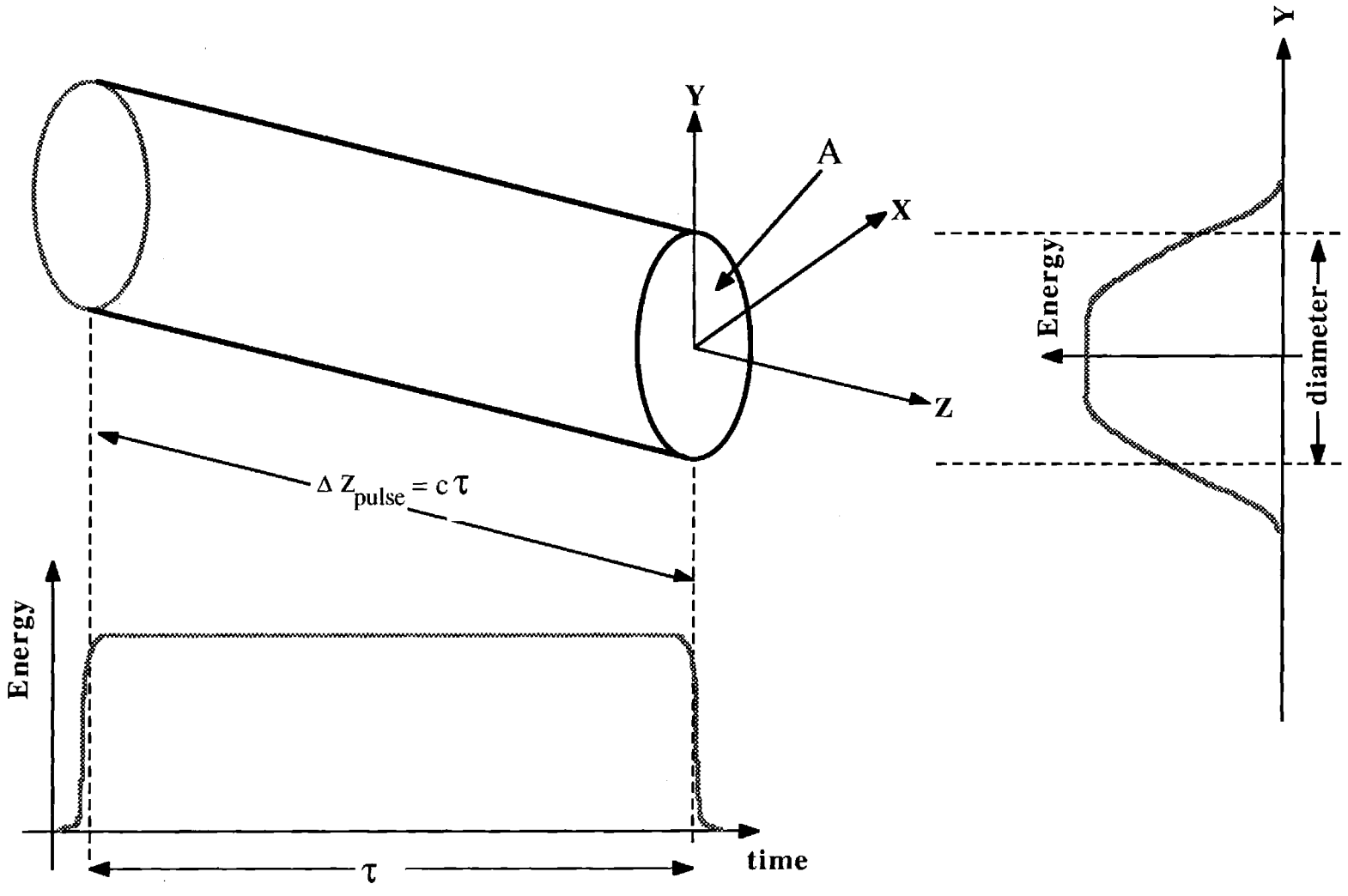

Figure 21: View of the propagating pulse showing its various dimensions.

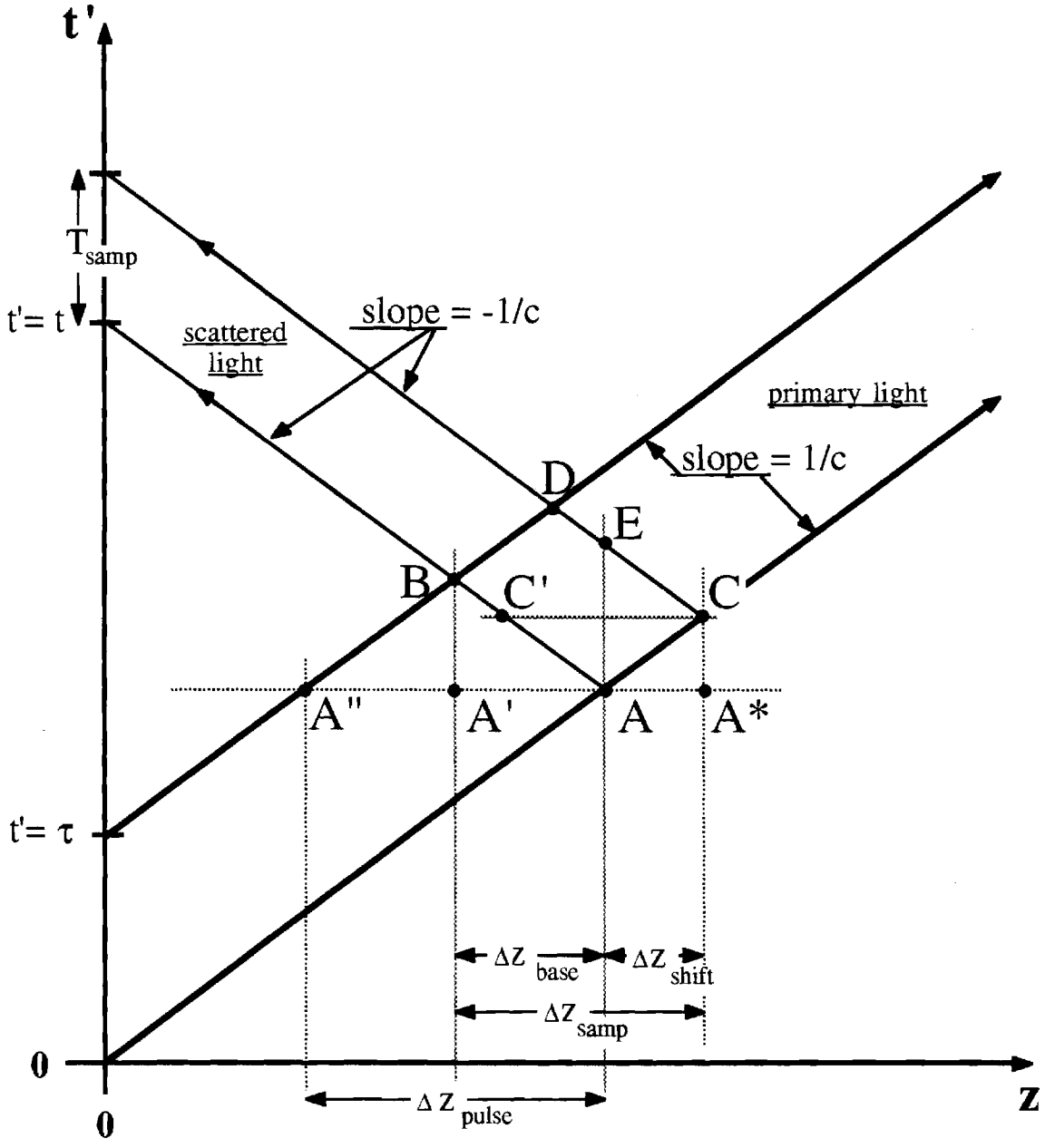

Figure 22: Space-time trajectories for various parts of a pulse having duration τ, transmitted from the origin at t = 0, and partially scattered back again into a detector at the origin.

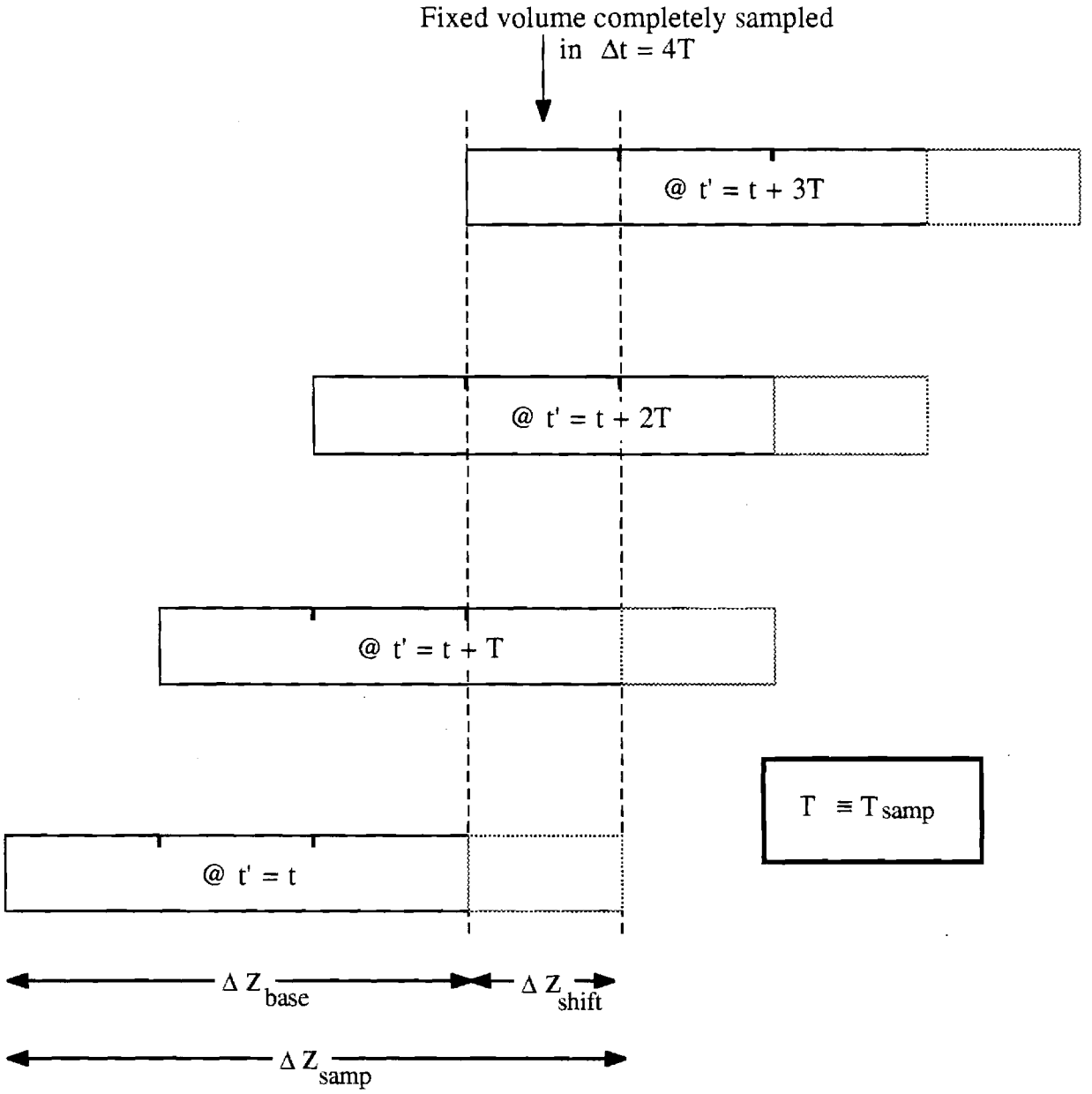

Figure 23: Time history of a primary pulse depicted as a series of "snapshots" separated in time by the sampling period T_{samp}. The value of *sample number* for the situation shown is f = 4.

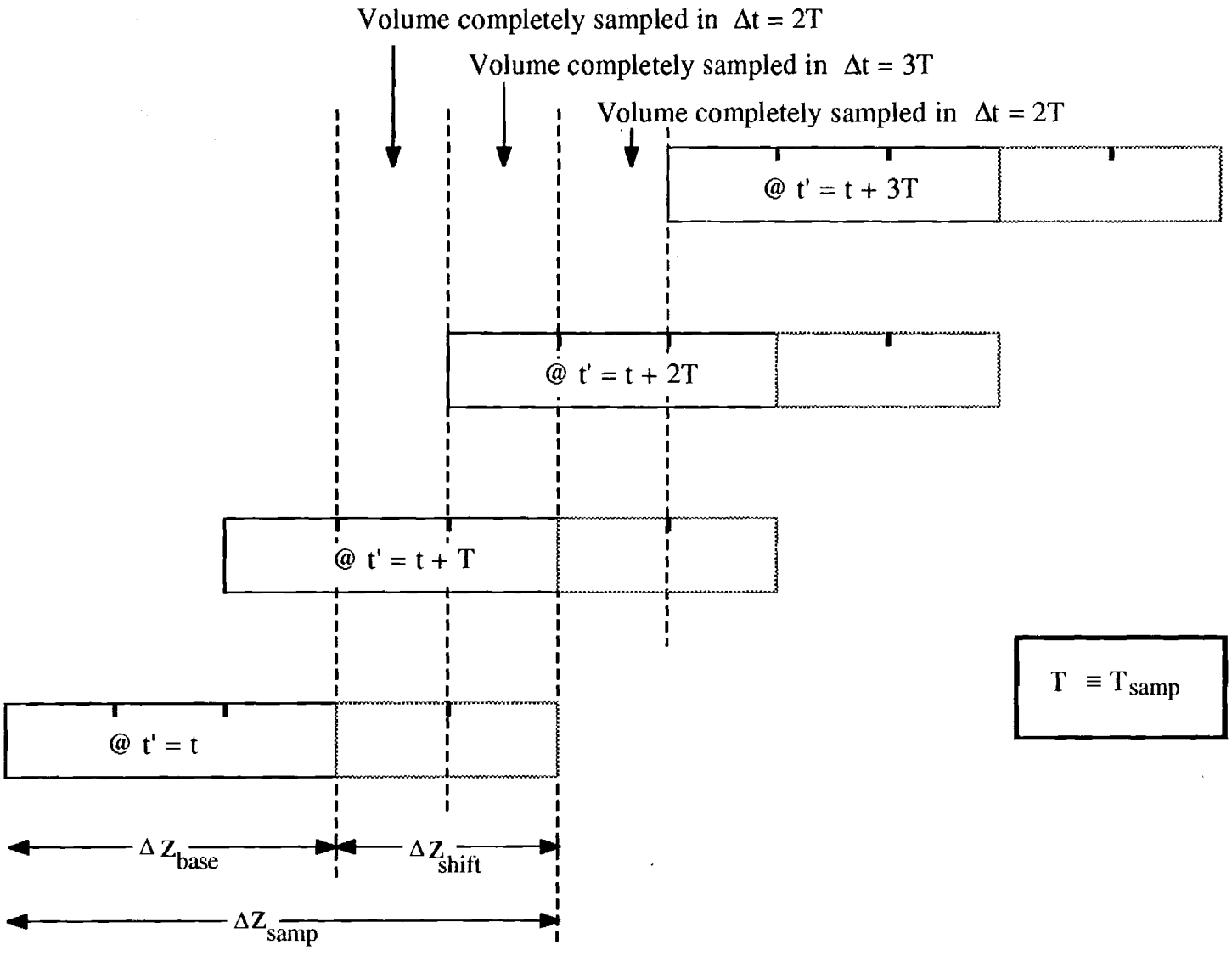

Figure 24: Time history of a primary pulse depicted as a series of "snapshots" separated in time by the sampling period T_{samp}. The value of *sample number* for the situation shown is f = 2.5 .

Appendix A:

Original phases and time schedule.

1. Laser reactivation [May - December 1984]
   a. Mechanical and electrical.
      (1) dye pumps, cooler: checkout.
      (2) flashtube: repair and testing.
   b. Optical.
      (1) external alignment.
      (2) end reflector installation.
      (3) cavity shape tuning.

2. Diagnostic instrumentation [October 1984 - February 1985]
   a. Wave meter.
      (1) echelle grating tests.
      (2) collimator tests.
      (3) Reticon detector array installation.
      (4) system integration.
      (5) calibration using c.w. laser as standard.
      (6) system testing using pulsed dye laser as source.
   b. Line-width spectrometer.
      (1) Fabry-Perot checkout.
      (2) Collimated mode operation using c.w. sources.
      (3) extended source operation using c.w. sources.
      (4) integration of Reticon detector array.
      (5) line width tests using Reticon with both c.w. and pulsed dye laser sources.

3. Etalon retrofitting [February - April 1985]
   a. Preliminaries.
      (1) mechanical (mount) control design and testing.
      (2) spectral response measurements using c.w. sources.
   b. Dye laser tuning.
      (1) staged tests of each etalon individually.
      (2) etalon cascade and fine tuning tests.
      (3) high-power degradation evaluation.

4. Detection system [January - September 1985]
   a. Detectors.
      (1) photomultiplier tests; gating and amplification.
      (2) signal digitization.
   b. Data acquisition.
      (1) CAMAC components: selection, purchase, and evaluation.
      (2) signal digitization.
      (3) system software development.
   c. Integrated system testing.

5. Indoor system testing [April - June 1985]
   a. Laser control.
      (1) spectral line center and width detection system: competitive design evaluation.
      (2) spectral line center and width detection system: construction and testing.
   b. Detector control.
      (1) gating system for single stage detection.
      (2) computer interfacing and testing.

6. Beam extraction optics [February - June 1985]
   a. calculations of beam energies at various system points.
   b. "Hardening" of vulnerable parts of the exit beam optics.
   c. Alignment tests.
   d. High-power tests.

7. Outdoor testing. [July - September 1985]
   a. Integrated system test at low pulse power along a horizontal path.
      (1) diagnosis of return signals: data-processing checkout.
      (2) spectrally resolved return analysis.
   b. High-power tests.
      (1) horizontal tests.
      (2) pointing and slewing tests.

Appendix B:

Derivation of range, sampling, and timing relations.

This appendix describes the space/time relations of the propagating/scattering pulse in greater detail than the report text. We start with [Fig.21] whose perspective drawing depicts the spatial features of a pulse of duration τ travelling along the z-axis, where its length is $\Delta z_{pulse} = c\tau$. The spatial profile of this pulse's irradiance is approximately uniform over the pulse's cross section **A**, as we show in the right-hand projected irradiance graph. The temporal profile of this pulse's irradiance is also approximately uniform over the pulse's duration τ, as we show in the lower projected irradiance graph.

A space-time diagram [Fig.22] of pulse component trajectories reveals connections between the propagating and scattered components of this pulse, and conditions for reception of its scattering at a detector coincident with its transmitter. Here we assume that pulse transmission begins at the origin of our coordinates at time $t' = 0$, and ceases there at $t' = \tau$. This pulse propagates in the direction of the positive **z**-axis at a rate **c**. The ray trajectories depict this by their positive slopes. Notice that the projection on the **z**-axis of any constant-time slice of this pulse, between its limiting trajectories, is just its spatial length Δz_{pulse}; while the projection on the **t'**-axis of any constant-position slice is just the pulse's duration τ.

Scattering of a portion of the transmitted pulse takes place at *every* point in this diagram within that space-time sector between the bounding trajectories of the positive-propagating pulse edges. A scattering event changes the direction of each transmitted trajectory into that of a scattered component. A typical scattering event is at point **B** in the diagram. This scattering from **B** propagates in the direction of the *negative* **z**-axis at a rate (**-c**) indicated by the slope of its trajectory. The scattering action simply "reflects" the incident component trajectory about a horizontal line through the scattering point in the space-time diagram. These scattered components of the radiation have *no* natural bounding trajectories as do the transmitted pulse trajectories. The scattering, therefore, is not in the form of a pulse, but rather in the form of a *continuous stream* of returning radiation. Also unlike the transmitted radiation, the scattering is not restricted to the **z**-axis, but rather propagates in virtually all directions. This has the effect of decreasing the irradiance of the scattering in *inverse proportion* to the *square of the distance* from the scattering site back to the receiver at the origin. This effect is implicit in the definition of the backscattering coefficient β_{π}^{z} in equation [5], and is explicit in the appearance of the reciprocal distance factor z^2 in equation [10].

One significant effect of the non-zero duration of the transmitted pulse, given the continuous nature of its scattering, is that the scattering destined to arrive at the receiver at any given instant is the superposition of many, single event scatterings. In [Fig.22], all events along the line between points **A** and **B**, and *only* events from this range of points, compose the scattering received at the instant $t' = t$. The receiver acts as a signal sampler, either directly or effectively due to its finite bandpass. In either case, the receiver has an associated integration time interval, which here we designate as T_{samp}. Considering this time interval, we designate points **C** and **D** also as special scattering points. The trajectory through *these* two points intersects the receiver space at the

moment $\mathbf{t' = t+T_{samp}}$. Consequently, scattering from all events bounded by the parallelogram **ABCD** appear within that sample which we designate by the time **t**. This is the same time coordinate that appears in the quantities $\mathbf{\mathcal{E}_r(t)}$ and $\mathbf{\Phi(t)}$ which we define by equations [6a,b] as integrals over that sample window designated by **t**.

Now that we have outlined our paradigmatic scattering trajectories, we can derive expressions for different volume elements associated with the scattering and sampling processes. First, scattering contributions to the *instantaneous* received power must come from events within a space such as that between points **A** and **B**. The size of this space is the projection of this line onto the **z**-axis, which in our diagram is the same as the length of the line **AA'**. We refer to this space as the *base volume* $\mathbf{V_{base}}$ and to this length as the *base length* $\mathbf{\Delta z_{base}}$. The symmetry which the diagram reveals leads us to conclude that $\mathbf{AA' = 1/2\,AA''}$. But since **AA"** is what we have been calling $\mathbf{\Delta z_{pulse}}$ above, this implies that

$$\Delta z_{base} = 1/2 * \Delta z_{pulse}$$

We have indicated these lengths appropriately in our diagram. Combining this with relations for $\mathbf{\Delta z_{pulse}}$ from above and acknowledging that the scattering volume has the same cross sectional area **A** (N.B. *not* point **A**) as the transmitted beam, we obtain

[Eq. 8] $$V_{base} = \left[A\left(\frac{c\tau}{2}\right)\right]$$

which refers back to a relation used in the text.

Scattering contributions to the integrated (sampled) received power must come from events within a space such as the parallelogram designated **ABCD**. The size of this space is the projection of the parallelogram diagonal **BC** onto the **z**-axis, which in our diagram is the same as the sum of the lengths of lines **AA'** and **AA†**. We refer to this space as the *sample volume* $\mathbf{V_{samp}}$ and to this length as the *sample length* $\mathbf{\Delta z_{samp}}$. The length of **AA†** is the distance that leading edge of the pulse can move forward, and still contribute scattering within the sampling window. We refer to this length as the pulse's *shifting* distance $\mathbf{\Delta z_{shift}}$. From our definitions, we can conclude that

$$\Delta z_{samp} = \Delta z_{base} + \Delta z_{shift}$$

We have indicated these lengths appropriately in our diagram. The time during which it can move forward and still contribute is the length of the projection of **AC** onto the **t'**-axis. The symmetry which the diagram reveals leads us to conclude that $\mathbf{AC' = 1/2\,AE}$. But since **AE** is just the sampling time $\mathbf{T_{samp}}$, this implies that

$$\Delta z_{shift} = 1/2 * cT_{samp}$$

Combining this with relations for $\mathbf{\Delta z_{pulse}}$ from above and acknowledging that the scattering volume has the same cross sectional area **A** (N.B. *not* point **A**) as the transmitted beam, we obtain

[Eq. 9a] $$\Delta z_{samp} = \frac{c}{2}\left[T_{samp} + \tau\right]$$

Using the same reasoning as to the size of the cross sectional area of the scattering volume

as above

[Eq. 9b] $V_{samp} = A \bullet \Delta z_{samp}$

These both refer back to relations used in the text.

Finally, we must derive the relations for sample number $\mathbf{f}$ and interpret this paramenter for both integral and non-integral values by means of spatial diagrams. Recall from the text that we define $\mathbf{f}$ as the number of (adjacent) sampling windows in which scattering from any given point appears. We can visualize the situation by means of a "multiple exposure" diagram such as that in [Fig.23].

In this diagram, we show four images of the sampled region, displaced from one another vertically for the sake of clarity, each positioned horizontally where it would be at time intervals of $\Delta \mathbf{t} = T_{\mathbf{samp}}$. Each sample region is composed of two parts. The first of these is the base region (length $\Delta z_{\mathbf{base}}$). In the text we identify this as the effective scattering region for the pulse's contributions to the power received at a given instant. The second region is the shift region (length $\Delta z_{\mathbf{shift}}$). This is generated by the pulse's forward movement during the time $\Delta \mathbf{t}$ where the extention includes the additional scattering region for the pulse's contributions to the power received during this time. Together these two regions define the entire volume sampled during $\Delta \mathbf{t} = T_{\mathbf{samp}}$.

In each sample region, the solid lines delineate the base and shift regions. The dashed lines subdivide the base region into thirds, and here are spaced at distances $\Delta z_{\mathbf{shift}}$. This means that, in this example, we must have $\Delta z_{\mathbf{shift}} = \Delta z_{\mathbf{base}}/3$. The dashed lines help to show the shift in the position of the base region relative to its previous position during $\Delta \mathbf{t}$. In this example, you should be able to see from these marks that the base region moves forward by exactly 1/3 of its own length during $\Delta \mathbf{t}$. This means that after exactly 3 intervals of $\Delta \mathbf{t}$, the base region will have "cleared" itself. Now draw two, adjacent vertical connections along these dashed lines and through adjacent sample pictures, as in the diagram. Since these lines stay fixed as the scattering region moves through with time, the region of space between them represents a *fixed* region of space, not a moving one such as the scattering region. Call this fixed region of space the *sampling analysis region.* You can see in the diagram that the sampling analysis region appears in *exactly four* samples. Thus for this situation we must have, by definition, $\mathbf{f} = 4$. A bit more thoughtful inspection should convince you that this sampling analysis region is a paradigm for *every* region. Thus, in this situation, *every* region of space is sampled four times.

A logical analysis of the preceding relations leads to a formula for calculating the sample number $\mathbf{f}$. Refer to the first shift region ($\Delta z_{\mathbf{shift}}$) of the lowest (earliest) sample rendering in the diagram. It is the first sample region to enter the sampling analysis region; thus it is **1** in the count of samples in which this sampling analysis region appears. A length of that sample region trails behind and moves forward in increments of $\Delta z_{\mathbf{shift}}$. In order for the moving sample region to *completely clear* the sample analysis region, it must move forward ($\Delta z_{\mathbf{samp}}/\Delta z_{\mathbf{shift}}$) more increments. This is *one more* than the number of samples in which this sampling analysis region appears. Thus, we count the number of samples in which the sampling analysis region appears as **1 +**

$[(\Delta z_{samp}/\Delta z_{shift}) - 1]$. But this count is, by definition, the sample number f. We conclude that

$$f = 1 + \frac{\Delta z_{samp}}{\Delta z_{shift}} - 1 = \frac{\Delta z_{samp}}{\Delta z_{shift}}$$

Using the relations for Δz_{samp} and Δz_{shift} in terms of τ and T_{samp} obtained above

[Eq. 13] $$f = \frac{\Delta z_{samp}}{\Delta z_{shift}} = \frac{T_{samp} + \tau}{T_{samp}}$$

This refers back to a relation used in the text.

The interpretation we have presented above applies validly to any situtation in which the value of f is an integer. For non-integer values of f the same analysis holds regarding the derivation of equation [13]; however the sampling interpretation is slightly different. To explore this, we present [Fig.24] which depicts a situation where $f = 2.5$. Again we may start by fixing our attention on the first shift region (Δz_{shift}) of the lowest (earliest) sample rendering in the diagram. Define the region above this as the sampling analysis region by extending vertical lines upward through the subsequent samples. Counting the number of incremental movements of the sampling region needed to clear the sampling analysis region leads to the same conclusions regarding the formulation of f in terms of τ and T_{samp}.

However, referring to the picture, you will see that there are now two categorically distinctive subregions of the sampling analysis region. Subregion TYPE A is sampled twice, while subregion TYPE B is sampled three times. In this case, each of these subregions is of equal size; but in general they have unequal sizes. Some thought should convince you that

the value for $\mathbf{f}$ calculated from equation [13] is actually an average of the two categorical sample numbers $\mathbf{f}_A$=2 and $\mathbf{f}_B$=3, the weights being provided by the relative sizes of the respective regions. Thus, as before

$$\mathbf{f} = \frac{T_{samp} + \tau}{T_{samp}}$$

and

$$\mathbf{f}_A = \text{INT}(\mathbf{f});\ \mathbf{f}_B = \mathbf{f}_A + 1$$

$$W_A = \frac{\mathbf{f}_A}{\mathbf{f}_A + \mathbf{f}_B};\quad W_B = \frac{\mathbf{f}_B}{\mathbf{f}_A + \mathbf{f}_B};\quad \text{and, of course,}\quad W_A + W_B = 1.$$

where W_A and W_B are the relative lengths of subregions type A and B, respectively. Thus

$$\mathbf{f} = W_A \mathbf{f}_A + W_B \mathbf{f}_B$$

It should now be clear than whenever the sample number has a non-integral value, the scattering region, from the standpoint of sampling, becomes partitioned into regions of total length Δz_{shift}. Within each such region appear two subregions. One of these is sampled INT($\mathbf{f}$) times and has length

$$\Delta z_A = \Delta z_{shift} \bullet W_A$$

The other is sampled INT($\mathbf{f}$) + 1 times and has length

$$\Delta z_B = \Delta z_{shift} \bullet W_B$$

Here INT($\mathbf{f}$) means the greatest integer less than $\mathbf{f}$. The sampling picture of the entire scattering region, then, is one of alternating regions, one each of the type we have just described.

[Fig.21] View of the propagating pulse showing its various dimensions.
[Fig.22] Space-time trajectories for various parts of a pulse of duration τ, transmitted from the origin at **t**=0, and partially scattered back into a detector at the origin.
[Fig.22] Space-time trajectories for various parts of a pulse of duration τ, transmitted from the origin at **t**=0, and partially scattered back into a detector at the origin.
[Fig.23] Diagram depicting the time history of a pulse as a series of "snapshots" separated in time by the sampling period $T_{\mathbf{samp}}$. The value of sample number for the situation shown is $\mathbf{f} = 4$.
[Fig.x24] Diagram depicting the time history of a pulse as a series of "snapshots" separated in time by the sampling period $T_{\mathbf{samp}}$. The value of sample number for the situation shown is $\mathbf{f} = 2.5$.